Generation, Optimization and Amplification of Ultrashort Infrared Pulses

by

Hao Huang

A dissertation submitted in partial fulfillment
of the requirements for the degree of
Doctor of Philosophy
(Applied Physics)
in the University of Michigan
2023

Doctoral Committee:

Professor Igor Jovanovic, Co-Chair
Professor Karl Krushelnick, Co-Chair
Dr. Milos Burger
Professor Almantas Galvanauskas
Professor Herbert Winful

Hao Huang
haohg@umich.edu
ORCID iD: 0000-0003-3045-329X

Per aspera ad astra.

Dedicated to my family.

Acknowledgments

I would like to thank all the people who have altruistically guided, supported, and accompanied me during my academic journey at the University of Michigan. A majority of the work included in this dissertation could not be completed amid the COVID-19 pandemic without our perseverance.

First I would like to thank Professor Krushelnick and Professor Jovanovic. I have been fortunate to be working with such resourceful and devoted advisors who are always willing to engage closely and work with their students. You have offered me opportunities to conduct research in the Gérard Mourou Center for Ultrafast Optical Science (CUOS) and inspired me with your deep passion for research.

I would also like to thank my dissertation committee members and people who also played important roles in this dissertation. I thank Professor Galvanauskas for your advice on our collaboration project and Professor Winful for all the profound derivations in your nonlinear optics lecture. I would like to thank Dr. Milos Burger for guiding me through the most difficult phases of my doctoral journey. I appreciate John Nees's help during my onboarding. I thank him for constantly bringing in his unique perspectives and inspiring me and everyone around with his creativity. Thank you Dr. Andrew McKelvey for our fruitful discussions and for working closely with me as a seasoned researcher. Thank you Dr. Bixue Hou for your expertise in Labview and synchronization. Thank you all for your kind support of my dissertation. The skills I have learned and the experience I gained from working with you are invaluable.

I would like to thank Dr. Yifan Cui for his contributions and discussions during our collaboration project. It would be impossible to get those critical results without your efforts. I remember the excitement when we first observed the long-wave infrared light. I thank my colleagues in Prof. Galvanauskas's team, Dr. Tong Zhou, Dr. Yao Xu, Dr. Hanzhang Pei, Dr. Siyun Chen, Dr. Weizhi Du, Mingshu Chen, Yu Bai, Yanwen Jing, Alexander Rainville, Dr. Matthew Whittlesey, Lauren Cooper, Chris Pasquale,

and Tayari Coleman for accompanying me through the years here. I learned a lot from the interactions with all of you.

I have been fortunate to have the opportunity to work in two of the largest laser facilities in CUOS, namely the Lambda Cubed Laser and Zettawatt-Equivalent Ultrashort Pulse Laser System (ZEUS). I would like to thank my Lambda Cubed Laser lab mates Dr. Jinpu Lin, Nick Peskosky, Jon Murphy, Dr. Lauren Finney, Dr. Patrick Skrodzki, and Dr. Xuan Xiao as well as ZEUS staff members Dr. Anatoly Maksimchuk, Lauren Weinberg, Franko Bayer, Amy Brooks, and Gaylene Opal-Deitering for their assistance and support.

I thank my cohort in the Department of Chemistry, Department of Physics, and Applied Physics program for their resourcefulness. They are Dr. Jingru Xie, Dr. Shang Zhang, Dr. Zhi Zheng, Dr. Yangwenxiao Zeng, Dr. Jia Li, Dr. Liuxing Shen, Dr. Anqi Chen, Dr. Kexin Zhang, Dr. Jiaqi Hu, Dr. Lise Wei, and Dr. Sunan Cui. I thank Professor Cagliyan Kurdak and Cynthia D'Agostino McNabb in the Applied Physics program and Professor Zhan Chen in the Department of Chemistry for their advice and support. I also thank my fellow e-board members at the Optics Society at the University of Michigan for serving our optics community.

Finally, the deepest thanks go to my family. I thank my parents for their unconditional love and support regardless of the decisions I made and the places I went to. This dissertation is dedicated to you.

Table of Contents

List of Figures

List of Tables

List of Acronyms

AC Autocorrelation.

ADC Analog-to-digital Converter.

AGS $AgGaS_2$.

AGSe $AgGaSe_2$.

AOPDF Acousto-optic Programmable Dispersive Filter.

CEP Carrier-envelope Phase.

CP-DFG Chirped-pulse Difference-frequency Generation.

CPA Chirped-pulse Amplification.

CW Continuous-wave.

DAC Digital-to-analog Converter.

DC-OPA Double-chirped Optical Parametric Amplification.

DFG Difference-frequency Generation.

DOF Depth of Focus.

FPGA Field-programmable Gate Array.

FROG Frequency-resolved Optical Gating.

FWHM Full Width at Half Maximum.

FWM Four-wave Mixing.

GA Genetic Algorithm.

GDD Group Delay Dispersion.

GVM Group Velocity Mismatch.

HHG High-harmonic Generation.

HWP Half-waveplate.

KTA $KTiOAsO_4$.

LIDT Laser-induced Damage Threshold.

LPA Laser-plasma Accelerator.

LWFA Laser Wakefield Acceleration.

LWIR Long-wave Infrared.

mid-IR Mid-infrared.

NIR Near-infrared.

OPA Optical Parametric Amplification.

OPCPA Optical Parametric Chirped-pulse Amplification.

OPG Optical Parametric Generation.

OPO Optical Parametric Oscillation.

PBS Polarizing Beamsplitter.

PCF Photonic-crystal Fiber.

PSD Power Spectral Density.

SC Supercontinuum.

SFG Sum-frequency Generation.

SHG Second-harmonic Generation.

SPM Self-phase Modulation.

SSFS Soliton Self-frequency Shift.

SVEA Slowly Varying Envelope Approximation.

TFP Thin-film Polarizer.

TPA Two-photon Absorption.

XFROG Cross-correlation Frequency-resolved Optical Gating.

ZDW Zero-dispersion Wavelength.

ZEUS Zetawatt-Equivalent Ultrashort Pulse Laser System.

ZGP $ZnGeP_2$.

Abstract

The development of few-cycle, ultra-intense laser sources in the long-wave infrared (LWIR, 8–12 µm) is of keen interest in many research fields, including molecular spectroscopy in the "fingerprint" region, laser-induced filamentation, remote sensing, and strong-field physics such as laser particle acceleration and high-harmonic generation. LWIR sources have gained their foothold due to their high transmittance in the atmosphere and their advantages granted by wavelength-scaling rules. The current absence of LWIR laser sources capable of generating ∼100-fs pulses with multi-terawatt peak power is due to the lack of broadband laser gain medium in the LWIR. The state-of-the-art CO_2 lasers can produce multi-terawatt peak power, however, in a relatively long picosecond duration. Our vision for delivering such performance is through optical parametric chirped-pulse amplification (OPCPA) of ultra-broadband, carrier-envelope phase (CEP) stabilized LWIR seed. Facilitated by the coherent combining and mid-infrared Er:ZBLAN fiber technologies, the energy scaling capabilities of such architecture can be further extended.

This dissertation focuses on developing few-cycle, ultra-intense LWIR laser sources in three key aspects. First, LWIR seed pulses were generated through difference-frequency generation (DFG) in birefringent nonlinear crystals. For the first time, milliwatt-level LWIR seed pulses were produced by mixing 2.9-µm Er:ZBLAN fiber amplifier/compressor outputs with their frequency-shifted replicas. Higher pulse energy (110 nJ) and ultra-

broadband spectral bandwidth (supporting two-cycle pulses) were achieved at a lower repetition rate driven by two-color Ti:sapphire laser output and assisted by genetic algorithm optimization. A single-shot infrared spectroscopy study on ammonia was performed with the LWIR seed source.

Second, parametric amplification of LWIR seed pulses was realized through non-collinear optical parametric amplification (NOPA) in a 5-mm thick GaSe crystal, pumped by nanosecond 2.7-µm pulses. As a consequence of crystal properties related to laser-induced damage threshold and the beam-pointing fluctuation, the attained parametric gain was limited.

Lastly, an active beam-pointing control system was developed to address the beam-pointing fluctuations confronted in a laser system. Using a proportional feedback loop and piezo-actuated mirror, the short-term beam-pointing fluctuations induced by ambient vibration were significantly reduced by up to an order of magnitude in a proof-of-principle study. Long-term fluctuations due to temperature drift were also eliminated.

To summarize, two broadband LWIR seed sources driven by an Er:ZBLAN fiber laser and a solid-state Ti:sapphire laser were developed, accompanied by the implementation of numerical models and optimization algorithms. Experimental and analytical efforts were presented on characterizing ultrashort LWIR pulses. Amplification of LWIR pulses was accomplished in an OPCPA apparatus with limited parametric gain. The diminished efficacy of the system was attributed to deteriorated nonlinear crystal and beam pointing. An active control system was constructed to potentially tackle the latter by compensating for the beam-pointing fluctuations using a proportional feedback-controlled piezo-actuated mirror. This dissertation research paves new paths for generating and characterizing few-cycle, CEP-stabilized ultra-intense LWIR pulses favorable by a broad spectrum of applications.

Chapter 1

Introduction

1.1 Background

Since the first demonstration of a working laser by Maiman in 1960 [1], researchers' pursuit of ultrafast and ultra-intense lasers has never ceased. The *Science* magazine highlighted "What is the most powerful laser researchers can build?" as one of the unsolved scientific puzzles that have been driving the fundamental research [2]. The development of ultrafast and ultra-intense lasers opens an unprecedented path to extreme conditions in the laboratory, such as ultrafast time scales, ultra-intense electromagnetic fields, and ultra-high energy densities, which are of vital interest for ultrafast molecular dynamics [3], laboratory astrophysics [4], [5], laser-driven nuclear physics [6], and laser-plasma accelerators [7], [8]. Figure 1.1(a) highlights the development trends for ultrafast and ultra-intense lasers with respect to their peak power with milestone techniques and PW-class laser facilities marked.

The invention of Q-switching [10] and mode-locking [11]–[15] techniques greatly enhanced the laser peak power to ∼GW level. To produce even higher peak power in laser

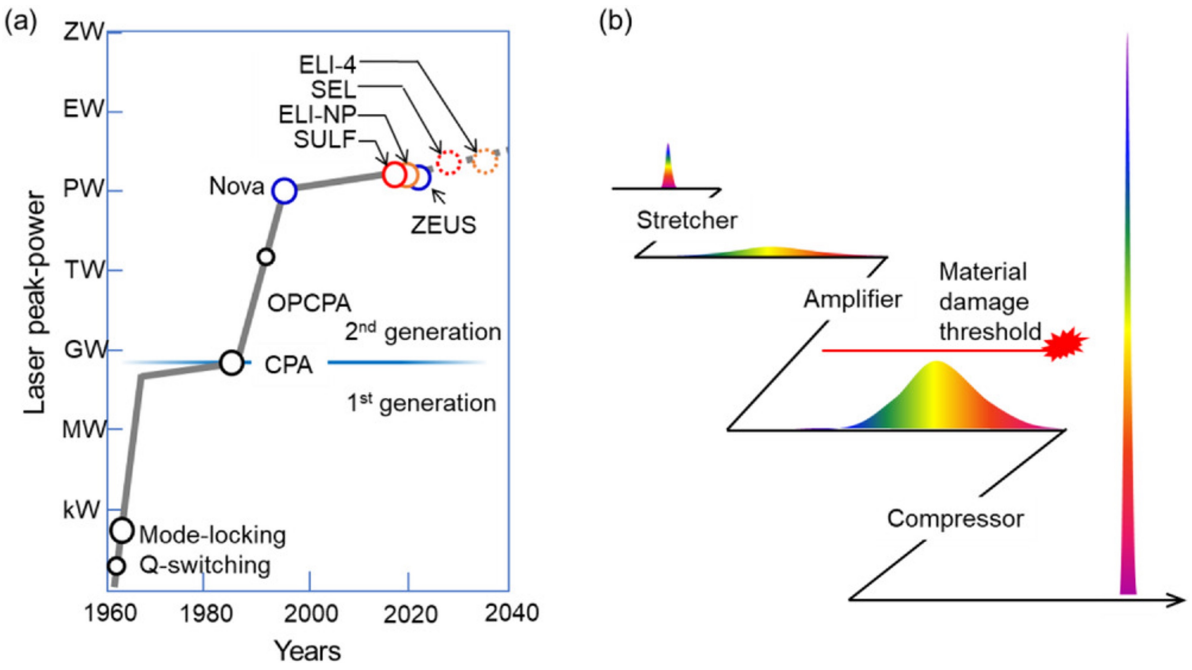

Figure 1.1: (a) The development trends in laser peak power marked with milestone technologies and PW-class laser facilities. (b) Schematic of Chirped-pulse Amplification (CPA) technique. Reprinted from [9].

amplifiers, it is necessary to avoid the accumulation of nonlinear phase and material damage. CPA has been a breakthrough technology that increases the pulse peak power by $\sim 10^5\times$ with pulse stretching and re-compressing (Figure 1.1(b)) [16]. In a solid-state, free-space CPA, further 10^1–$10^2\times$ energy increase can be achieved through transverse crystal size scaling.

The large available dimensions of neodymium-doped glass (meter-sized) empowered the first PW-class facility Nova Petawatt [17]. Multi-kJ pulses can be generated with $\sim$1 ps pulse duration due to its limited gain bandwidth ($\sim$20 nm Full Width at Half Maximum (FWHM)) [17]–[23]. The progress of Ti:sapphire technology starting from the 1980s provides the high-power laser community an unparalleled gain medium with broadest gain bandwidth ($\sim$200 nm FWHM) along with other desirable characteristics

Table 1.1: Comparison of the minimum spectral bandwidth required for two-cycle transform-limited pulses generation at four different central wavelengths involved in this dissertation. λ_0: central wavelength. $\Delta\lambda_{min}$: minimum spectral bandwidth required assuming a Gaussian pulse shape.

λ_0 (µm)	Pulse duration (fs)	$\Delta\lambda_{min}$ (nm)	$\Delta\lambda_{min}/\lambda_0$
0.8	5.3	180	0.22
1.06	7.07	230	0.22
2.8	18.7	620	0.22
10.6	70.7	2300	0.22

such as high damage threshold (∼8–10 J/cm^2), large saturation fluence (∼1 J/cm^2) and high thermal conductivity (∼46 W/mK) [24]. Although the maximum pulse energy attainable from Ti:sapphire amplifiers is around a few hundred Joules (1/10 of that of the neodymium-doped glass lasers), the much shorter compressed pulse duration (tens of femtoseconds) promotes the Ti:sapphire to be the workhorse in the state-of-the-art multi-PW facilities such as Zetawatt-Equivalent Ultrashort Pulse Laser System (ZEUS) [25], Shanghai Superintense Ultrashort Laser Facility (SULF) [26], and Extreme Light Infrastructure – Nuclear Physics (ELI-NP) [27].

The relative emission bandwidth ($\Delta\lambda/\lambda_0$) of Ti:sapphire crystal (∼0.3) supports <5 fs, few-cycle transform-limited pulse generation. Nevertheless, PW-class Ti:sapphire lasers usually produce tens of femtoseconds pulses as a consequence of gain narrowing and shifting [28]. Further scaling up the peak power is hindered by parasitic lasing and available crystal size (∼200 mm [29]).

Optical Parametric Chirped-pulse Amplification (OPCPA), a branch of Optical Parametric Amplification (OPA), was proposed in the 1990s [30] and opened new horizons for 100-PW-class [31]–[33] and even EW-class [34] lasers. Compared to the CPA technique, it has several advantages, such as a broader and smoother gain bandwidth, reduced

thermal load in the gain medium, and a lower stretching and compression factor required if a high-damage-threshold nonlinear medium can be employed. The parametric process leads to a suppressed gain narrowing and shifting, thus a broader and smoother gain profile, supporting few-cycle pulse generation. Table 1.1 elucidates the minimum spectral bandwidth $\Delta\lambda_{\min}$ required for two-cycle pulse production with respect to four different central wavelengths λ_0 discussed or investigated in this dissertation. The minimum relative emission bandwidth ($\Delta\lambda_{\min}/\lambda_0$) are identical for all λ_0, however, the $\Delta\lambda_{\min}$ scales with λ_0. The most extensively used laser gain mediums at those wavelengths are Ti:sapphire, Nd:YAG, Er:ZBLAN, and CO_2, respectively. Among them, Ti:sapphire is the only one that satisfies the minimum relative emission bandwidth requirement specified in Table 1.1. In fact, few-cycle pulse generation directly from a Ti:sapphire oscillator has been demonstrated [35], [36]. The author believes that OPCPA provides a promising route towards few-cycle, ultra-intense pulses generation for wavelengths spanning Near-infrared (NIR), Mid-infrared (mid-IR), and Long-wave Infrared (LWIR) by circumventing the bandwidth limitation of laser gain medium.

As discussed above, ultrashort pulses as short as a few cycles can be produced. For such a short pulse, Carrier-envelope Phase (CEP) starts to play an increasingly important role. A stabilized CEP with attosecond accuracy is crucial for few-cycle, high-field laser applications such as High-harmonic Generation (HHG) and attosecond spectroscopy [37], [38]. The effect of CEP can be seen in the time-domain expression for the electric field of an optical train with noise:

$$E(t) = [E_0 + \Delta E_0(t)] \sum_{m=-\infty}^{+\infty} a(t - mT_R + \Delta T_R(t)) exp\{j[2\pi\nu_c t + m\Phi_{CE} + \Delta\theta(t)]\}, \tag{1.1}$$

where E_0 is the amplitude of the pulse, $\Delta E_0(t)$ is the amplitude noise, $a(t)$ is the pulse envelope function (for example, Gaussian), T_R is the pulse repetition period, $\Delta T_R(t)$ is the pulse timing jitter, ν_c is the carrier frequency, Φ_{CE} is the CEP, and $\Delta\theta(t)$ represents the phase fluctuations of the field.

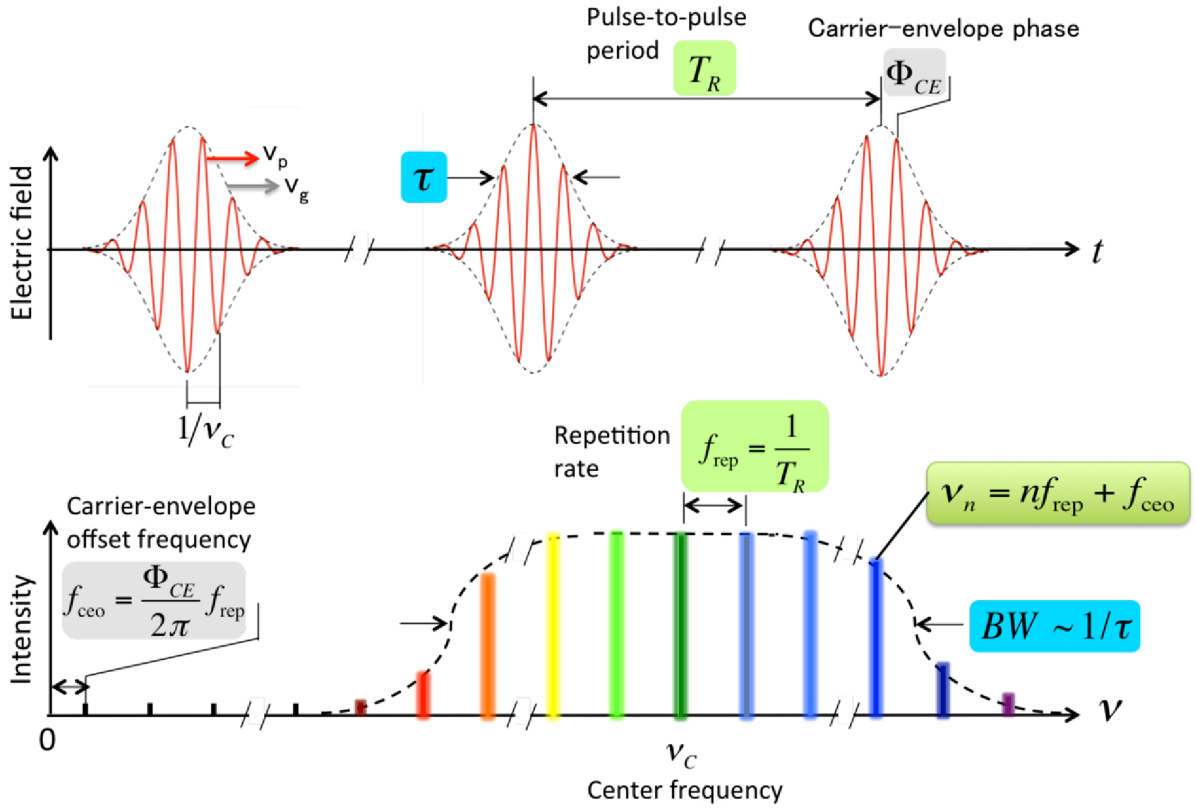

Figure 1.2: Time-frequency correspondence of the few-cycle pulsed output from a mode-locked laser. Reprinted with permission from [39] © The Optical Society.

This expression is further illustrated in the time and frequency domain in Figure 1.2, connecting the CEP in the time domain with the carrier-envelope offset frequency (f_{CEO}) in the frequency domain. The output of a mode-locked laser consists of millions of equally spaced, phase-locked longitudinal modes with spacing $f_{ref} = 1/T_R$. The offset of the entire comb from zero frequency is carrier-envelop-offset frequency f_{CEO},

where $f_{CEO} = mod(\Phi_{CE}, 2\pi) f_{rep}/(2\pi)$. The optical frequency of each comb line (ν_n) can then be expressed as $\nu_n = f_{CEO} + n \cdot f_{rep}$. The measurement of CEP can be accomplished with an f-2f interferometer [40]–[42]. An octave-spanning spectrum covering ν_n–ν_{2n} is necessary to perform a heterodyne detection between $\nu_{2n} = 2n \cdot f_{rep} + f_{CEO}$ and frequency-doubled ν_n ($2\nu_n = 2n \cdot f_{rep} + 2f_{CEO}$). To actively control the CEP, sophisticated feedback controllers have been implemented assisted with fast actuators [43]–[46]. In contrast, passive CEP cancellation through optical parametric processes such as Difference-frequency Generation (DFG) and OPA provides a simple and effective method to stabilize CEP [47]–[49]. An example will be given in Chapter 3.

1.2 Motivation

Accompanied by the development of few-cycle, ultra-intense Ti:sapphire lasers, the study of self-channeling (filamentation) of intense lasers in the atmosphere has been significantly advanced. The extension of its propagation distance from tens of meters [50], [51] to multiple kilometers [52] offers unique opportunities for standoff detection, remote sensing, and long-range transmission of high-power electromagnetic radiation [53]. Through a dynamic equilibrium among self-focusing, diffraction, and plasma defocusing, an intense laser beam can propagate over extended distances much longer than the typical diffraction length while remaining a confined transverse size without the help of any external guiding mechanism.

The intensity of such a laser beam is limited by the multiphoton absorption and thus can be reduced by operation at longer wavelengths. Self-focusing overcomes diffraction and initiates the collapse only if the laser peak power exceeds the critical power $P_{cr} \propto \lambda^2$ [54]. The transverse dimension of the filament and self-channeling distance are both

proportional to the driver's wavelength, λ. As a result of these scaling laws, few-cycle, ultra-intense LWIR sources are favorable for driving self-channeling research.

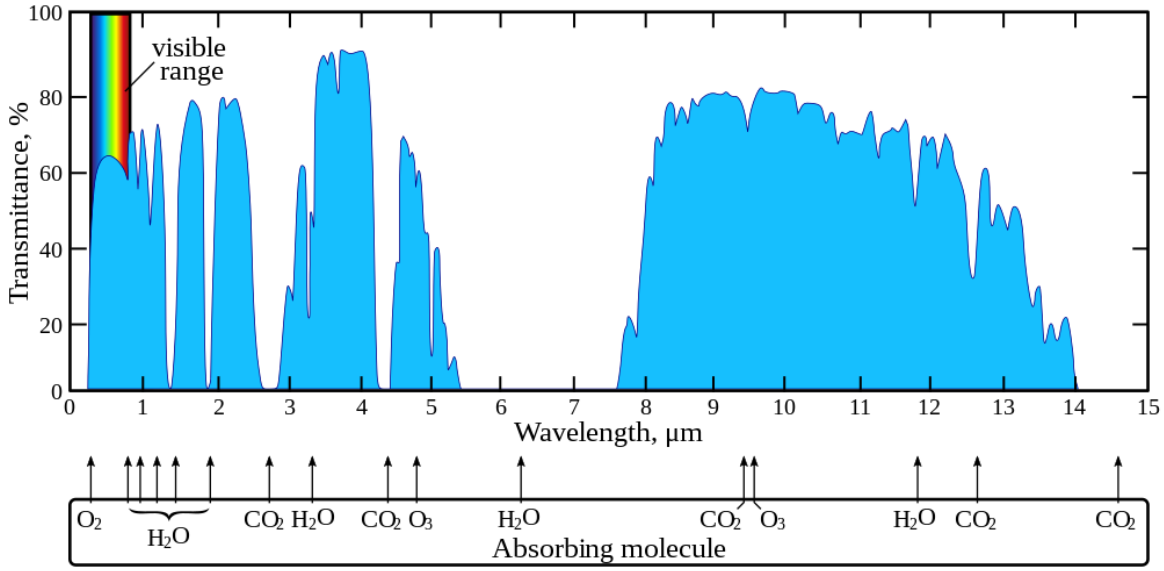

Figure 1.3: Atmospheric transmission window. Reprinted from [55].

Compared to NIR (1–2.5 μm) and mid-IR (3–5 μm), the LWIR (8–12 μm) atmospheric transmission window experiences a lower loss induced by absorption and scattering and has shown an enhanced propagation through fog and clouds with weaker perturbation from turbulence [56], [57]. Figure 1.3 shows the transmission of atmospheric gases. Due to the lack of few-cycle, ultra-intense LWIR sources, most of the atmospheric laser-induced filamentation experiments have been demonstrated with NIR and mid-IR sources [50]–[52], [58]–[61]. Recently, a centimeter-diameter "megafilament" over 20 Rayleigh lengths in the air has been demonstrated, supported by the development of the state-of-the-art LWIR TW-class CO_2 laser [62]. The LWIR (8–12 μm) atmospheric transmission window also incorporates characteristic absorption bands of several molecules of great interest, such as glucose, O_3, CF_4, and NH_3. A single-shot spectroscopic study of NH_3 gas will be presented in Appendix A.

In strong-field laser applications such as Laser-plasma Accelerator (LPA) and HHG, the ponderomotive force affects plasma density distribution and drives particle acceleration. The ponderomotive energy, U_p describes the cycle-averaged quiver energy of a free electron driven by an electromagnetic field and scales with driver laser's intensity (I) and wavelength (λ) squared [63]. Compared with the cutting-edge PW laser facilities operating at ∼1 µm wavelength, few-cycle, ultra-intense LWIR driver provides additional two orders of magnitude scaling of U_p at the same intensity, since $U_p \propto I\lambda^2$. Correspondingly, to maintain high U_p, the wavelength is a more effective control when the boost of laser intensity is limited by ionization saturation.

To date, the main technologies for LWIR pulse production can be categorized by the method they use: stimulated emission of radiation from population inversion and nonlinear frequency conversion. The former includes lead-salt semiconductor lasers, quantum cascade lasers, free-electron lasers, and CO_2 lasers. Lead-salt lasers require cryogenic cooling and have low output power (∼0.1 mW) and narrow bandwidth [64]. Quantum cascade lasers have limited peak power and wavelength tunability. Sub-picosecond pulses could be generated from a quantum cascade laser despite a complex architecture involving spectral filtering, spectral broadening, and external pulse compression [65]. Free-electron lasers can cover an extremely broad wavelength region from X-ray to THz, with >10 kW average power outputs in the LWIR [66], [67]. Their large footprint and high building and operating cost, however, hinder their extensive applications. CO_2 lasers are presently the only sources that can produce high peak-power, short pulses in the LWIR; therefore, they deserve a special mention. By direct amplification [68] or using CPA [69], TW-class LWIR pulses have been produced from CO_2 lasers. However, the amplification bandwidth of CO_2 limits the LWIR pulses to picosecond duration, on the order of tens of optical cycles. A CO_2 system also encounters other considerable

constraints such as low repetition rate (several Hz) and large footprint. To circumvent these constraints, several approaches have been developed, including the use of high-pressure mixed-isotope amplifiers [69], optical pumping by Fe:ZnSe lasers [70], [71] and nonlinear pulse compression [72], [73].

On the other hand, nonlinear frequency conversion methods have evolved into promising candidates for few-cycle, ultra-intense LWIR pulse production, albeit they confront challenges in identifying suitable nonlinear materials. The development of non-silica, soft glasses such as telluride [74] and chalcogenide [75] enables ultra-broadband LWIR pulses generation via Supercontinuum (SC) generation [76]. The output power of a SC source is limited in the case where a waveguide is implemented. What's more, the complex nonlinear nature of SC poses considerable challenges to pulse compression and therefore is not feasible for few-cycle pulse production. Parametric frequency down-conversion techniques such as Optical Parametric Generation (OPG), Optical Parametric Oscillation (OPO), DFG, OPA, and OPCPA have been remarkably successful in extending the wavelength towards LWIR while maintaining the capabilities of producing CEP stabilized, few-cycle, ultra-intense pulses due to their broad bandwidth and wavelength agility [30], [77]–[79]. The main objective of this dissertation is to explore the potential of such architecture where broadband LWIR seed pulses were first produced (Chapter 2 and 3), then bandwidth-optimized (Chapter 3) and further amplified and characterized (Appendix A).

1.3 Technical Basis for Nonlinear Wave Propagation and Parametric Frequency Down-conversion

This section lays the foundation for the concepts such as DFG, OPA, and OPCPA being experimentally investigated in Chapters 2 and 3 and Appendix A.

Starting from Maxwell's equations, the nonlinear wave propagation equation and coupled-mode equations will be derived in this section:

$$\begin{aligned} \vec{\nabla} \times \vec{E} &= -\frac{\partial \vec{B}}{\partial t}, \\ \vec{\nabla} \times \vec{H} &= \vec{J} + \frac{\partial \vec{D}}{\partial t}, \\ \vec{\nabla} \cdot \vec{D} &= \rho_f, \\ \vec{\nabla} \cdot \vec{B} &= 0, \end{aligned} \tag{1.2}$$

where $\vec{E}$ is electric field vector, $\vec{H}$ is magnetic field vector, $\vec{D}$ and $\vec{B}$ are corresponding electric and magnetic flux densities, $\vec{J}$ is current density vector, and ρ_f is the charge density. The wave equation for the electric field propagating in a nonlinear medium can then be derived from

$$\vec{\nabla} \times \vec{\nabla} \times \vec{E} = -\frac{1}{c^2}\frac{\partial^2 \vec{E}}{\partial t^2} - \mu_0 \frac{\partial^2 \vec{P}(\vec{r},t)}{\partial t^2}, \tag{1.3}$$

where $\vec{P}$ is the polarization induced by the electric field in the material.

The electric field and the induced electric polarization can be expressed as the sum

of different frequency components:

$$\begin{aligned}\vec{E}(\vec{r},t) &= \sum_n \frac{1}{2}\vec{E}^{\omega_n} e^{-i\omega_n t} + c.c. \\ \vec{P}(\vec{r},t) &= \sum_n \frac{1}{2}\vec{P}^{\omega_n} e^{-i\omega_n t} + c.c.\end{aligned} \tag{1.4}$$

The double curl operator can be simplified using the identity

$$\vec{\nabla} \times \vec{\nabla} \times \vec{E} = \vec{\nabla}(\vec{\nabla} \cdot \vec{E}) - \vec{\nabla}^2 \vec{E} = -\vec{\nabla}^2 \vec{E}, \tag{1.5}$$

since $\vec{\nabla} \cdot \vec{E} = 0$ for plane waves in a charge-free, homogeneous media.

Inserting the Equation (1.4) and Equation (1.5) in Equation (1.3) and considering only a single frequency, the wave equation becomes

$$\vec{\nabla}^2 \vec{E}^{\omega_n} = -\frac{\omega_n^2}{c^2}\vec{E}^{\omega_n} - \mu_0 \omega_n^2 \vec{P}^{\omega_n}. \tag{1.6}$$

The induced polarization consists of linear and nonlinear components such that

$$\vec{P}^{\omega_n} = \vec{P}_L^{\omega_n} + \vec{P}_{NL}^{\omega_n}, \tag{1.7}$$

where

$$\vec{P}_L^{\omega_n} = \varepsilon_0 \overset{\leftrightarrow}{\chi}^{(1)}(\omega_n)\vec{E}^{\omega_n}, \tag{1.8}$$

and $\overset{\leftrightarrow}{\chi}^{(1)}(\omega_n)$ is the first order susceptibility. The wave equation can be written in a

form where the nonlinear polarization plays the role of a driving source term:

$$\vec{\nabla}^2\vec{E}^{\omega_n} = -\frac{\omega_n^2}{c^2}[1 + \overleftrightarrow{\chi}^{(1)}(\omega_n)]\vec{E}^{\omega_n} - \mu_0\omega_n^2\vec{P}_{NL}^{\omega_n}. \tag{1.9}$$

The linear dispersion of a crystal can also be characterized by principal refractive indices defined as

$$n_i^2(\omega_n) = 1 + \overleftrightarrow{\chi}^{(1)}(\omega_n) = \varepsilon_{ii}(\omega_n)/\varepsilon_0, \tag{1.10}$$

where $\varepsilon_{ii}(\omega_n)$ is the absolute permittivity. The wave equation can therefore be written as

$$\vec{\nabla}^2\vec{E}^{\omega_n} + \frac{\omega_n^2}{c^2}\overleftrightarrow{\varepsilon}\cdot\vec{E}^{\omega_n} = -\mu_0\omega_n^2\vec{P}^{\omega_n,NL}. \tag{1.11}$$

For the nonlinear polarization due to the second order susceptibility, the polarization component at frequency ω_n due to the interaction of two fields at frequencies ω_a and ω_b can be expressed as

$$\vec{P}_{NL}^{\omega_n} = \varepsilon_0\overleftrightarrow{d} : \vec{E}^{\omega_a}\vec{E}^{\omega_b} \tag{1.12}$$

and, in component form, as

$$\vec{P}_{NL,i}^{\omega_n} = \varepsilon_0 d_{ijk}\vec{E}_j^{\omega_a}\vec{E}_k^{\omega_b}, \tag{1.13}$$

where the tabulated constant $d_{ijk} = \chi_{ijk}^{(2)}/2$. If the unit vectors along the polarization directions of the interacting fields as $\hat{e}^{\omega_a}$ and $\hat{e}^{\omega_b}$ are involved, the nonlinear polarization

can be expressed using the concept of effective susceptibility. Let the direction of the nonlinear polarization vector at frequency ω_n be $\hat{e}^{\omega_n}$. The scalar amplitude of the nonlinear polarization vector is then obtained by projection onto $\hat{e}^{\omega_n}$:

$$P^{\omega_n} = \hat{e}^{\omega_n} \cdot \vec{P}_{NL}^{\omega_n} = \varepsilon_0 \hat{e}^{\omega_n} \cdot \overleftrightarrow{d} : \hat{e}^{\omega_a} \hat{e}^{\omega_b} E^{\omega_a} E^{\omega_b}. \tag{1.14}$$

The effective susceptibility is then

$$d_{eff} = \hat{e}^{\omega_n} \cdot \overleftrightarrow{d} : \hat{e}^{\omega_a} \hat{e}^{\omega_b}. \tag{1.15}$$

It is effectively the nonlinear susceptibility tensor component involved in generating the field at ω_n. The effective susceptibility varies by different crystals and also can be maximized by choosing the field polarization and the propagation directions appropriately.

Ordinary and extraordinary waves are the two propagating eigenmodes in an anisotropic crystal. For each eigenmode, the scalar wave equation can be obtained by projecting it into its propagation direction:

$$\nabla^2 E^{\omega_n} + \frac{\omega_n^2 n^2(\omega_n)}{c^2} E^{\omega_n} = -\mu_0 \omega_n^2 P_{NL}^{\omega_n}, \tag{1.16}$$

where $n(\omega_n)$ is the refractive index associated with the particular eigenmode. If we set the propagation direction as the z-axis, the homogeneous wave equation for each eigenmode in the absence of nonlinear polarization can be written as

$$\frac{d^2 E^{\omega_n}}{dz^2} + \frac{\omega_n^2 n^2(\omega_n)}{c^2} E^{\omega_n} = 0, \tag{1.17}$$

for which the solution is the plane wave with constant amplitude:

$$E^{\omega_n} = A^{\omega_n} e^{ik_n z}, \tag{1.18}$$

where the wavenumber $k_n = n(\omega_n)\omega_n/c$. For the inhomogeneous equation

$$\frac{d^2 E^{\omega_n}}{dz^2} + \frac{\omega_n^2 n^2(\omega_n)}{c^2} E^{\omega_n} = -\mu_0 \omega_n^2 P_{NL}^{\omega_n}, \tag{1.19}$$

a similar plane wave solution can be assumed, but with the amplitude being a slowly varying function of distance, which represents the forced wave driven by the nonlinear polarization:

$$E^{\omega_n}(z) = A^{\omega_n}(z) e^{ik_n z}. \tag{1.20}$$

To find the form of the amplitude function $A^{\omega_n}(z)$, one can take the derivatives of the assumed solution:

$$\begin{aligned} \frac{dE^{\omega_n}}{dz} =& (\frac{dA^{\omega_n}(z)}{dz} + ik_n A^{\omega_n}(z)) e^{ik_n z} \\ \frac{d^2 E^{\omega_n}}{dz^2} =& (\frac{d^2 A^{\omega_n}(z)}{dz^2} + 2ik_n \frac{dA^{\omega_n}(z)}{dz} - k_n^2 A^{\omega_n}(z)) e^{ik_n z} \end{aligned} \tag{1.21}$$

Since the amplitude is slowly varying, the following inequality holds:

$$|\frac{d^2 A^{\omega_n}(z)}{dz^2}| \ll |2k_n \frac{dA^{\omega_n}}{dz}| \ll |k_n^2 A^{\omega_n}|. \tag{1.22}$$

The first term in Equation (1.22) is negligible under Slowly Varying Envelope Approx-

imation (SVEA), and the inhomogeneous wave equation becomes

$$2ik_n \frac{dA^n}{dz} = -\mu_0 \omega_n^2 P_{NL}^{\omega_n} e^{-ik_n z}. \tag{1.23}$$

DFG and OPA are mixing processes that involve three photons of different energies propagating through a nonlinear medium. The pump photon ω_1 with higher energy converts to one signal photon ω_2 with a lower frequency and an idler photon $\omega_3 = \omega_1 - \omega_2$, whose energy equals the difference between pump and signal photons. The schematic of the interaction and the energy-level diagram are shown in Figure 1.4. In order to reach the LWIR wavelength region, the energy difference between pump and signal photons must be less than ~0.15 eV.

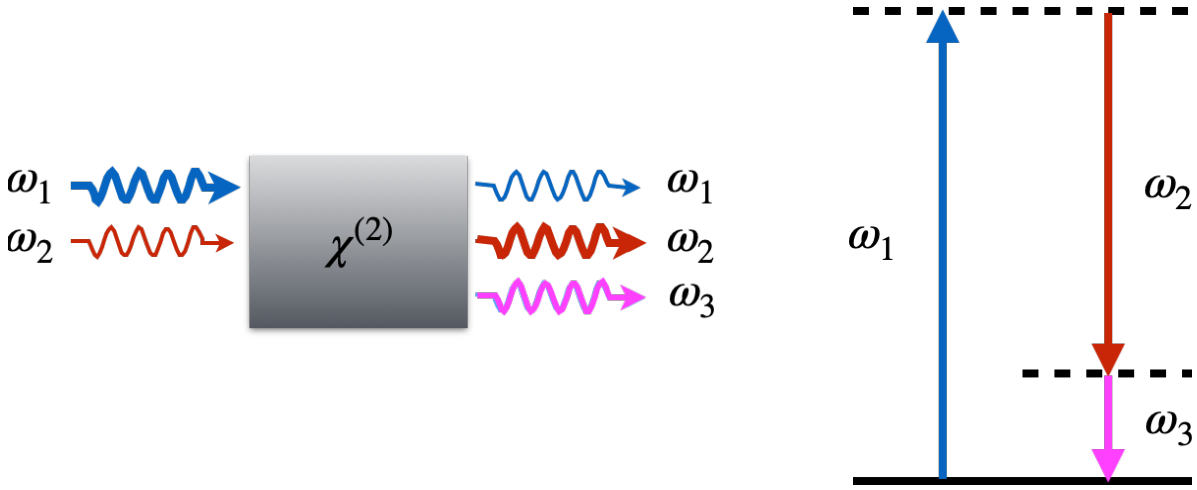

Figure 1.4: Schematics of DFG. Left: three-wave mixing scheme. Right: energy-level diagram.

The nonlinear polarizations for the pump, signal, and idler wave can be expressed as:

$$\begin{aligned} P_i^{\omega_1} =& 2\varepsilon_0 d_{ijk} E_j^{\omega_2} E_k^{\omega_3} \\ P_i^{\omega_2} =& 2\varepsilon_0 d_{ijk} E_j^{\omega_1} E_k^{\omega_3 *} \\ P_i^{\omega_3} =& 2\varepsilon_0 d_{ijk} E_j^{\omega_1} E_k^{\omega_2 *} \end{aligned} \tag{1.24}$$

If the material is lossless and dispersionless, Kleinman's symmetry holds so that the d_{ijk} is independent of frequency. There is also $E^{\omega_n} = A^{\omega_n} e^{ik_n z}$. Then substituting in the SVEA Equation (1.23), the coupled-mode equations can be derived as

$$\begin{aligned} \frac{dA_1}{dz} =& i\eta_1 \omega_1 \varepsilon_0 d A_2 A_3 e^{-i\Delta k z} \\ \frac{dA_2}{dz} =& i\eta_2 \omega_2 \varepsilon_0 d A_1 A_3^* e^{i\Delta k z} \\ \frac{dA_3}{dz} =& i\eta_3 \omega_3 \varepsilon_0 d A_1 A_2^* e^{i\Delta k z}, \end{aligned} \tag{1.25}$$

where $\Delta k = k_1 - k_2 - k_3$.

Under perfect phase matching conditions, $\Delta k = 0$ and $k_1 = k_2 + k_3$. In addition, following the law of conservation of energy $\omega_1 = \omega_2 + \omega_3$, we have:

$$\begin{aligned} \frac{\omega_1 n^{\omega_1}}{c} =& \frac{\omega_2 n^{\omega_2}}{c} + \frac{\omega_3 n^{\omega_3}}{c} \\ n^{\omega_1} =& \frac{\omega_2 n^{\omega_2} + \omega_3 n^{\omega_3}}{\omega_2 + \omega_3}. \end{aligned} \tag{1.26}$$

Assuming an undepleted pump and perfect phase matching, the coupled-wave equations

become

$$\begin{aligned}\frac{dA_1}{dz} =&0\\ \frac{dA_2}{dz} =&i\eta_2\omega_2\varepsilon_0 dA_1 A_3^*\\ \frac{dA_3}{dz} =&i\eta_3\omega_3\varepsilon_0 dA_1 A_2^*.\end{aligned} \tag{1.27}$$

Here A_1 is constant, and therefore the differential equations become

$$\begin{aligned}\frac{dA_2}{dz} =&K_2 A_3^*\\ \frac{dA_3}{dz} =&K_3 A_2^*,\end{aligned} \tag{1.28}$$

where $K_2 = i\eta_2\omega_2\varepsilon_0 dA_1$ and $K_3 = i\eta_3\omega_3\varepsilon_0 dA_1$. We take a derivative of the above coupled-wave equations:

$$\frac{d^2A_2}{dz^2} = K_2\frac{A_3^*}{dz} = K_2K_3^*A_2 = \kappa^2 A_2, \tag{1.29}$$

where $\kappa^2 = K_2K_3^* = \eta_2\omega_2\eta_3\omega_3\varepsilon_0^2 d^2|A_1|^2$. The above equation can be solved and the same for A_3; the resulting solutions are

$$\begin{aligned}A_2(z) =&Ccosh\,(\kappa z) + Dsinh\,(\kappa z)\\ A_3(z) =&\frac{\kappa}{K_2^*}(C^*sinh\,(\kappa z) + D^*cosh\,(\kappa z))\end{aligned} \tag{1.30}$$

Considering the boundary conditions:

$$\begin{aligned}A_2(0) =&constant\\ A_3(0) =&0,\end{aligned} \tag{1.31}$$

the solutions are

$$\begin{aligned} A_2(z) =& A_2(0)\cosh(\kappa z) \\ A_3(z) =& i(\frac{\eta_3\omega_3}{\eta_2\omega_2})^{1/2} e^{i\phi_1} A_2^*(0)\sinh(\kappa z) \end{aligned} \tag{1.32}$$

For a small κz, $\sinh(\kappa z) \sim \kappa z$, and the idler grows linearly. On the other hand, both the sinh and cosh functions can be approximated by $e^{\kappa z}$ if κz is large enough, and therefore both the signal and idler waves in DFG or OPA grow exponentially in these conditions. Since $\kappa \propto |A_1|$, increasing the pump intensity greatly enhances the parametric gain [80].

1.4 Nonlinear Crystal Selection and Design Considerations

Nonlinear crystals are an essential component for parametric down-conversion sources. The crystal's transparency range, nonlinearity, linear and nonlinear absorption, the Laser-induced Damage Threshold (LIDT), phase-matching bandwidth, and other characteristics need to be evaluated to be compatible with the desired few-cycle, ultra-intense LWIR outputs. Oxide nonlinear crystals are not transparent beyond ~5 µm and thus are not suitable for LWIR pulse generation. Figure 1.5 summarizes non-oxide crystals that are transparent in the mid-IR and LWIR region. The horizontal extent of each line segment indicates the transparency range, while the vertical position indicates the nonlinear figure of merit (d_{eff}^2/n^3, where d_{eff} is the effective nonlinearity and n is the refractive index) in $\mathrm{pm}^2/\mathrm{V}^2$. The nonlinear figure of merit is a quantitative measure of the efficiency of the corresponding nonlinear frequency conversion process. $ZnGeP_2$ (ZGP), GaSe, $AgGaS_2$ (AGS), and $AgGaSe_2$ (AGSe) are the most commonly

used birefringent crystals for LWIR pulse production as their transparency range covers the entire 8–12 µm LWIR atmospheric transmission window. The first three crystals will be employed in the experiments discussed in Chapters 2, Appendix A, and Chapter 3, respectively. Quasi-phase-matching materials such as OP-GaAs [81], [82] and OP-GaP [83], [84] have also been developed and employed in LWIR generation recently, due to their attractive properties. However, the intricacy of the growth process and limited transverse dimension (<1 mm) limit their implementation for high-power pulse generation.

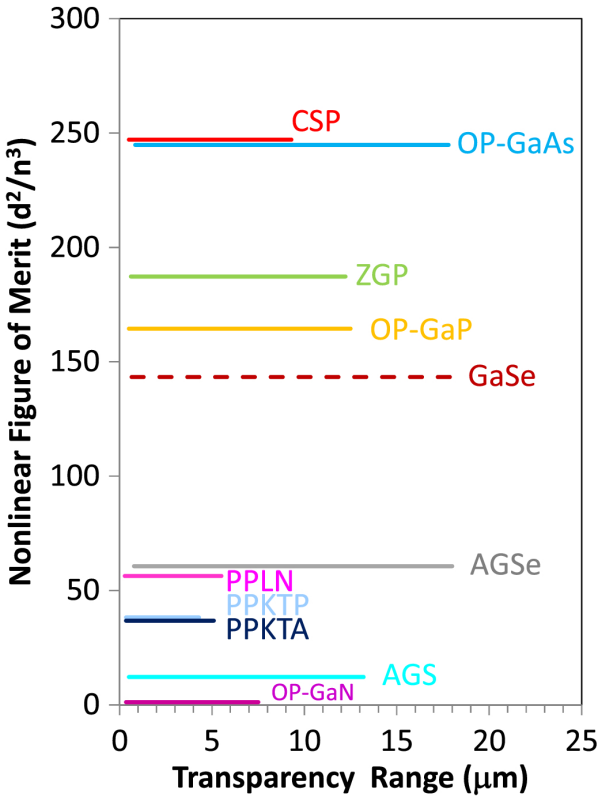

Figure 1.5: Nonlinear figure of merit versus transparency range of various nonlinear crystals. Reprinted with permission from [85] © The Optical Society.

Table 1.2 shows a comparison of the characteristics of four birefringent nonlinear

Table 1.2: Characteristics of four most commonly used birefringent nonlinear crystals. NLCs: nonlinear crystals. ZGP: $ZnGeP_2$. AGS: $AgGaS_2$. AGSe: $AgGaSe_2$.

NLCs	ZGP	GaSe	AGS	AGSe
Transparency Range (μm)	0.74 – 12 [86]	0.62 – 20 [87]	0.47 – 13 [88]	0.71 – 19 [89]
Bandgap (eV) (Wavelength)	2.1 [90] (590 nm)	2.0 [91] (620 nm)	2.76 [92] (449 nm)	1.8 [93] (689 nm)
Linear Absorption Coefficient α (cm^{-1})	1.52 [94] (1.06 μm) 0.16 [95] (2.0 μm) 0.06 [96] (2.79 μm) 0.9 [97] (10.6 μm)	0.45 [98] (1.06 μm) 0.1 [98] (1.9 μm) 0.081 [99] (10.6 μm)	0.01 [100] (0.7–9 μm) 0.01–0.02 [101] (1.06 μm) 0.012–0.024 [92] (2.8 μm) 0.6 [92] (10.6 μm)	0.012-0.2 [92] (1.06 μm) 0.002 [102] (1.3 μm) <0.015 [103] (1.45-1.6 μm) 0.015-0.058 [104] (2.05 μm) 0.008-0.012 [92] (2.8 μm) 0.01-0.018 [92] (10.6 μm)
Two-photon Absorption Coefficient β (cm/W)	2.5×10^{12} [105] (1.3 μm, 130 fs)	6.8×10^{12} [106] (0.9 μm, 200 fs)	1.8×10^{12} [107] (0.8-0.87 μm, 200 fs)	2.5×10^{14} [108] (1.08 μm, 40 ps)
Damage Threshold (GW/cm^2)	0.003 [109] (1.06 μm, 10 ns) >150 [105] (1.3 μm, 130 fs) >100 [105] (1.66 μm, 130 fs) >0.074 [110] (2.05 μm, 10 ns) 35 [111] (2.79 μm, 100 ps) 30 [87] (2.94 μm, 110 ps)	<6.4 [112] (1.03 μm, 200 fs) >1.0 [113] (1.053 μm, 2 ps) 0.03 [114] (1.06 μm, 10 ns) >4 [115] (2.80 μm, 100 ps) 30 [86], [87] (2.94 μm, 110 ps)	>60 [107] (0.8–0.87 μm, 200 fs) 3 [116] (1.06 μm, 20 ps) 0.035 [117] (2 μm, 6 ns)	0.013-0.04 [118] (1.06 μm, 23 ns) >0.02 [119] (1.57 μm, 6 ns) 0.0083 [120] (2.0 μm, 30 ns) 0.025 [121] (2.79 μm, 40 ns)

crystals in the LWIR region. A detailed comparison under specific phase-matching conditions and pump wavelengths will be shown in Chapter 2, Table 2.2 and Table 2.3. The bandgap energy of a direct bandgap material determines the minimum photon energy required for an optical transition; therefore, it is related to the absorption properties of a nonlinear crystal. The intensity-dependent material absorption can be described as

$$\frac{dI}{dz} = -\alpha I - \beta I^2, \tag{1.33}$$

where I is the intensity of the electromagnetic wave, z is the propagation distance, α is the linear absorption coefficient, and β is the intensity-dependent Two-photon Absorption (TPA) coefficient. The nonlinear crystal should be selected such that the absorption at pump, signal, and idler wavelengths are minimized. The TPA can be eliminated (or significantly alleviated) if the bandgap energy exceeds twice the pump photon energy. As a result, if the parametric frequency down-conversion process is driven by a Ti:sapphire laser at 800 nm (Chapter 3), the AGS crystal is the only option due to its transmission range and reduced TPA for the pump.

As derived in Section 1.3, high-intensity pump pulses are preferred in parametric interactions to achieve a higher gain. LIDT of the nonlinear crystal thus constrains the maximum achievable parametric gain. For pulses longer than a few tens of picoseconds, LIDT is generally caused by heat deposition, resulting in material melting and boiling [122]. In this regime, the fluence of the LIDT scales with the square root of the pulse duration ($\tau^{1/2}$). For shorter pulses, the damage mechanism evolves to an ablative regime dominated by collisional and multiphoton ionization and plasma formation [122], [123]. The LIDT fluence in this regime is approximately proportional to the pulse duration, but the exact scaling law is poorly understood. LIDT values have been reported for

various nonlinear crystals, which typically vary significantly due to differences in testing standards, apparatus, laser specifications, and material quality control (Table 1.2). Systematic LIDT studies with well-controlled conditions and, in particular, highly stable, high-beam-quality short pulse [124] and ultrashort pulse lasers are necessary to advance the knowledge of LIDT.

Other design considerations for parametric frequency down-conversion systems arise from the necessity for spatial and temporal overlap between the pump, signal, and idler during the three-wave mixing process. In the spatial domain, the overlap of the three waves is affected by the differences in diffraction and Poynting vector walk-off. The Depth of Focus (DOF) for a Gaussian beam due to diffraction is defined as

$$DOF = \frac{8\lambda}{\pi}(f/\#)^2, \tag{1.34}$$

where λ is the wavelength, $f/\# = F/D$ is the f-number of the focusing optic and equals the ratio of focal length F and the aperture size D. The DOF represents the axial length where the beam transverse radius becomes $\sqrt{2}$ times larger than the beam waist, and it scales with its wavelength. Under the same focusing geometry, the pump beam has the shortest DOF. Therefore, its DOF can be used as a rule of thumb for determining the maximum nonlinear crystal thickness. For example, at 2.9 µm pump wavelength, the DOF for $f/10$ focusing is $\sim$0.75 mm.

To realize critical phase-matching in a birefringent crystal, an extraordinary wave is needed. The direction of energy transport of such a wave deviates from its wave vector, reducing the efficiency of the nonlinear process. The angle ρ between the direction of the energy transport (Poynting vector $\vec{S} = \vec{E} \times \vec{H}$) the direction of the wave vector $\vec{k}$

can be calculated as

$$tan\,(\rho) = -\frac{1}{n_e}\frac{\partial n_e}{\partial \theta}, \tag{1.35}$$

where n_e is the refractive index of the extraordinary wave, θ is the angle between wave vector $\vec{k}$ and the optical axis. Examples of the maximum walk-off angles between three waves can be found in Chapter 2, Table 2.2, and Table 2.3. The nonlinear crystal's thickness should be limited such that the three beams stay mostly overlapped along the entire propagation.

The interaction length of a parametric frequency down-conversion process is also influenced by the temporal walk-off among three waves due to Group Velocity Mismatch (GVM). Each frequency component travels at its phase velocity in the nonlinear medium, while the ultrashort pulse travels at group velocity v_g as a wave packet. The group velocity v_g is defined as

$$v_g = \frac{c}{n\,(\lambda_0) - \lambda_0 \frac{\partial n}{\partial \lambda_0}}, \tag{1.36}$$

where c is the speed of light, n is the refractive index, and λ_0 is the central wavelength.

For ultrafast parametric frequency down-conversion processes, time-dependent coupled-wave equations are necessary to describe such non-stationary pulse propagation. Solving such equations analytically is often nontrivial. Numerical methods such as the split-step Fourier method [125] have been implemented to comprehensively understand the process, and the results will be shown in Chapter 2 and 3.

1.5 Dissertation Overview

This chapter discussed the methods for few-cycle, high-power LWIR pulse generation via optical parametric processes and provided their analytical description. The remainder of this dissertation addresses the scientific and engineering obstacles standing in the path toward developing an ultrashort, high-power LWIR source.

- Chapter 2 presents the first demonstration of high repetition rate, milliwatt-level LWIR source driven by a femtosecond mid-IR all-fluoride fiber laser. The implementation of fluoride fiber-based soliton amplifiers and wavelength shifters operating in mid-IR along with ZGP crystal which has a high damage threshold, offers the potential for much higher LWIR powers and conversion efficiencies.

- Chapter 3 presents a single-stage approach to generate 100-nJ-level LWIR pulses pumped by a solid-state Ti:sapphire laser via DFG in an AGS crystal. The employed nitrocellulose pellicle leads to a non-alignment-critical, passively CEP stabilized configuration. Assisted by the Genetic Algorithm (GA), this chapter further demonstrates a three-fold improvement of the spectral bandwidth, which is of great importance to few-cycle LWIR pulses generation.

- Chapter 4 presents a systematic approach in order to address the laser beam-pointing instability discussed in Appendix A in a well-controlled environment amid the construction of ZEUS. The beam-pointing of a piezo-actuated 16-inch mirror is actively compensated with a simple proportional feedback control, which reduces the instability by up to an order of magnitude in the short term. The long-term beam-pointing jitter induced by temperature drift is completely eliminated.

- Appendix A first presents the application of ultra-broadband LWIR pulses gen-

erated in Chapter 3 in the spectroscopic study. The remainder of this appendix focuses on the characterization of ultrashort LWIR pulses in the temporal and spectral domain and the amplification of ultra-broadband LWIR pulses via OPCPA. It then discusses the limitations of the results due to crystal damage and beam-pointing instability.

- Chapter 5 concludes the dissertation with a discussion of the outcomes of each experiment, and directions for the improvement of future work are explored.

Chapter 2

Generation of High Repetition Rate Long-wave Infrared Pulses Driven by Mid-infrared Fluoride Fiber Laser

2.1 Introduction

High repetition rate femtosecond sources in the mid-IR (2.5–8 µm) and LWIR (8–12 µm) spectral regions are of great interest for applications in several areas of fundamental research and practical applications, including vibrational spectroscopy targeting the absorption lines of gases localized in the "fingerprint" wavelength region (2–20 µm),

This Chapter is based on the previously published article: Y. Cui, **H. Huang**, Y. Bai, W. Du, M. Chen, B. Zhou, I. Jovanovic, and A. Galvanauskas, "Long-wave-infrared pulse production at 11 µm via difference-frequency generation driven by femtosecond mid-infrared all-fluoride fiber laser," *Optics Letters*, vol. 48, no. 7, pp. 1890–1893, 2023. [126]

remote sensing, attosecond pulse generation, and high-field science [127]–[129]. However, there are no laser gain media that can directly generate or amplify femtosecond optical pulses with wavelengths longer than ∼4.4 µm [130], [131]. Therefore, for accessing longer wavelengths in mid-IR and LWIR it is necessary to use nonlinear wavelength conversion (such as DFG [81], [84], [112], [132]–[134], OPO [83], [135], OPG in a waveguide [82], or SC generation [74], [75]), pumped by lasers operating at shorter wavelengths. Table 2.1 summarizes the pump, signal, and idler demonstrated in these works, along with their conversion efficiencies. DFG-based schemes offer advantages of being much simpler than OPO, accommodating much higher energies than OPG in a waveguide, and much more efficient than SC generation.

Compared to other solid-state laser sources, fiber lasers provide the advantages of lower cost, relative compactness, robust maintenance-free operation, and diffraction-limited output beam, which are very important for practical applications. For operation at NIR wavelengths shorter than ∼2.1 µm fused-silica fibers with rare-earth doping of Er, Yb, Nd, Pr, Tm, and Ho are used [136]. For operation in ∼2.1–4 µm mid-IR wavelengths, rare-earth doped fluoride fibers are used instead of silica fibers, due to their broader transmission window reaching ∼4.5–5 µm [136], [137].

For accessing the "fingerprint" spectroscopy region at mid-IR and LWIR wavelengths longer than >4.5 µm, fused-silica-based femtosecond fiber lasers operating in NIR have been demonstrated for driving DFG conversion [81], [84], [112], [132]–[134]. Such mode-locked oscillator-based driver lasers provide high repetition rates of ∼10 MHz to >100 MHz, average powers ranging from ∼10 mW to few watts, and for practical applications seek robust, compact, and power-efficient laser systems. The general scheme for reaching these long wavelengths is to mix λ_p pump at ∼1 µm [112], [132], [133], ∼1.5 µm [84], [134], or ∼2 µm [81] with a slightly longer wavelength λ_s signal, such that

Table 2.1: Summary of LWIR pulses generation driven by ultrafast fiber laser pump and Soliton Self-frequency Shift (SSFS) or Self-phase Modulation (SPM) based signal. NLCs: nonlinear crystals. η: conversion efficiency. FC: frequency comb. CPA: chirped-pulse amplification. MOPA: master oscillator power amplifier. OSC: oscillator.

Pump	Signal	Idler	NLCs	η	Ref.
11.9-nJ, 80-fs @ 1055 nm. Yb-FC @ 151 MHz	0.13-nJ @ 1.28 µm (SSFS)	2-pJ @ 10 µm	0.5-mm GaSe	0.017%	[132]
<8-nJ @ 1092 nm. Yb-CPA-pumped SPM @ 40 MHz	1–1.25-nJ @ 1.24–1.26 µm (SSFS)	3.4-pJ @ 9 µm	2-mm AGS	n/a	[133]
<200-nJ, 165-fs @ 1030 nm. Yb-CPA @ 30 MHz	18.5-nJ, 120-fs @ 1.14 µm (SPM)	63-pJ @ 11.3 µm	2-mm GaSe	n/a	[112]
1.6-nJ, 65-fs @ 1550 nm. Er-MOPA @ 100 MHz	0.08-nJ, 40-fs @ 1.95 µm (SPM)	0.6-pJ @ 11 µm	1-mm GaSe	0.038%	[138]
8.1-nJ, 640-fs @ 1550 nm. Er-CPA @ 37 MHz	n/a @ 1.73–1.84 µm (SSFS)	<41-fJ @ 9.7–14.9 µm	1-mm GaSe, 5-mm AGSe	n/a	[139]
2.2-nJ, 50-fs @ 1550 nm. Er-OSC @ 250 MHz	0.8-nJ, 84-fs @ 1.86 µm (SSFS)	4-pJ @ 10.2 µm	1-mm GaSe	0.18%	[134]
1.6-nJ, 49-fs @ 1560 nm. Er-MOPA @ 40 MHz	1.8-nJ, 80-fs @ 1.88 µm (SPM)	39-pJ, ∼80-fs @ 9.2 µm	2-mm AGS	2.4%	[140]
17.1-nJ, 110-fs @ 1550 nm. Er-MOPA @ 93.4 MHz	6.4-nJ, 60-fs @ 1.9 µm (SPM)	200-pJ @ 10.5 µm	1-mm OP-GaP	1.2%	[141]
3.6-nJ, 76-fs @ 1570 nm. Er-MOPA @ 48 MHz	3.2-nJ @ 1.97 µm (SSFS)	150-pJ @ 7.5 µm	3-mm OP-GaP	4.2%	[142]
1.6-nJ, 65-fs @ 1560 nm. Er-MOPA @ 125 MHz	2.4-nJ @ 1.97 µm (SSFS)	36-pJ @ 8 µm	3-mm OP-GaP	2.3%	[84]
6-nJ, 145-fs @ 1950 nm. Tm-CPA @ 72 MHz	0.4-nJ @ 2.5 µm (SSFS)	18-pJ @ 10.3 µm	2-mm OP-GaAs	0.3%	[81]

the LWIR idler wavelength λ_i is determined by the relationship $1/\lambda_i = 1/\lambda_p - 1/\lambda_s$. The λ_s signal must be synchronous with the λ_p pump, and is therefore usually converted from a part of the ultrashort pump via either Raman-induced SSFS [81], [84], [132]–[134], or using self-phase modulation induced spectral broadening with a subsequent spectral filtering [112]. Using SSFS requires negative dispersion, which is automatically achieved at ∼1.5 µm and ∼2 µm wavelengths, above the Zero-dispersion Wavelength (ZDW) of ∼1.3 µm for fused-silica glass. At ∼1 µm SSFS can be implemented, but only using a ZDW-shifted Photonic-crystal Fiber (PCF) with a small diameter core [133].

The bottleneck of the SSFS-based approaches has been the low energies of the wavelength-shifted λ_s signal pulses. In the majority of experiments [81], [132], [134] only sub-nJ energy SSFS pulses were achieved, with slightly higher energies of ∼1 nJ reported in [133]. (Note that in [84] additional amplification in a Tm-doped fiber amplifier after the SSFS stage was used to increase signal energy to ∼2 nJ). This bottleneck is due to the limitations on the soliton energy, defined by fiber parameters and soliton wavelength. Fundamental-soliton energy is given by $E_p = 2|\beta_2|/(\gamma\tau)$, where $\gamma = 2\pi n_2/(\lambda_s A_{eff})$ is the fiber nonlinear coefficient, β_2 is fiber dispersion, τ is pulse duration, n_2 is the nonlinear refractive index, and A_{eff} is the effective mode area of the fiber [143].

However, it was recently reported that in ZBLAN fibers at ∼2.8 µm or longer wavelengths soliton energies can be significantly increased, primarily due to much lower nonlinear coefficients, resulting from long wavelengths and large single-mode cores [144]. For example, it was demonstrated in [144], [145] that 15-µm single-mode core Er:ZBLAN fiber-based nonlinear soliton-effect amplifier/compressor operating at ∼2.8 µm can produce <100 fs pulses with >40 nJ energies, and 2–4 W of average power, which is at least an order of magnitude energy increase compared to the same adiabatic soliton compression in Er:silica fibers at 1.55 µm. It is worth noting here that these soliton-

effect nonlinear amplifiers/compressors are much simpler and more compact than any CPA-type systems that were used as the NIR drivers for the DFG conversion reported in [81], [84], [112], [132], [133]. Furthermore, using ZBLAN fibers, the SSFS from ∼3 µm to ∼3.6 µm with ZBLAN fiber-based pump laser has yielded red-shifted pulse energies of 37 nJ [146], and the longest reached wavelength has been extended from ∼4.3 µm to ∼4.8 µm [147], [148]. These results, as well as a significantly higher quantum defect for DFG conversion to LWIR from 3–4 µm mid-IR compared to 1–2 µm NIR, indicate that ZBLAN fiber-based mid-IR drivers can have significant advantages compared to silica fiber-based NIR drivers.

To date, the most commonly used birefringent materials for femtosecond fiber laser driven DFG conversion into LWIR are GaSe [112], [132], [134], AGS [133], and AGSe [135]. Pumping DFG at 3–4 µm wavelength has the benefit of being compatible with ZGP, which has at least an order of magnitude higher damage threshold [105] and has one of the highest nonlinear figures of merit compared to these materials. This is particularly relevant for using higher pump and signal energies attainable with ZBLAN fiber-based lasers. Table 2.2 and 2.3 compare the performances of type I and II DFG with these four birefringent nonlinear crystals pumped at different wavelengths of NIR and mid-IR fiber laser drivers. For example, it was pointed in [112] that the low damage threshold in GaSe and AGSe crystals does not permit tight focusing for pump energies in the ∼100 nJ range. Using ZGP completely eliminates this limitation even for the highest obtainable pump and signal energies from ZBLAN fiber laser sources. Quasi-phase-matching materials such as OP-GaP [83], [84] and OP-GaAs [81], [82] have also been developed and employed in LWIR generation recently, due to their attractive properties comparable to ZGP.

In this letter, to the best of our knowledge, the first demonstration of an LWIR ultra-

Table 2.2: Comparison of Type-I DFG performance in different nonlinear crystals pump at different wavelengths. ZGP: $ZnGeP_2$. AGS: $AgGaS_2$. AGSe: $AgGaSe_2$. PM: phase matching. D_{eff}: effective nonlinear coefficient. FOM: figure of merit. GVM: group-velocity mismatch. The data were adapted from Reference [149].

Type I DFG Performance	ZGP	GaSe	AGS	AGSe
Mixing scheme pumped by $\lambda_p = 2.9\ \mu m$:	e+e=o	o+o=e	o+o=e	o+o=e
PM angle (°):	51.2	11.2	40.1	41.5
D_{eff} (pm/V):	79.0	55.0	9.53	23.3
FOM (pm^2/V^2):	205	151	7	31
Crystal acceptance angle (mrad·mm):	77	19.4	54.7	90.5
Temperature range (K·mm):	345.3	14572.4	679.2	1587.8
Idler bandwidth (THz·mm):	4.22	9.99	4.11	18.6
GVM (fs/mm):	240	100	244	53
Spatial walk-off (mrad):	12.38	54.82	22.20	12.26
Mixing scheme pumped by $\lambda_p = 1.95\ \mu m$:	e+e=o	o+o=e	o+o=e	o+o=e
PM angle (°):	52.1	11.1	34.9	44.5
D_{eff} (pm/V):	80.9	56.3	8.80	25.2
FOM (pm^2/V^2):	213	157	5.7	36
Crystal acceptance angle (mrad·mm):	50.9	13.2	38.4	63.1
Temperature range (K·mm):	226.8	2127.9	422.1	1151.1
Idler bandwidth (THz·mm):	26.0	n/a	6.10	13.2
GVM (fs/mm):	70	10	163	73
Spatial walk-off (mrad):	12.3	54.23	21.13	11.78
Mixing scheme pumped by $\lambda_p = 1.55\ \mu m$:	e+e=o	o+o=e	o+o=e	o+o=e
PM angle (°):	57.3	11.6	34.0	50.7
D_{eff} (pm/V):	78.2	57.1	8.75	28.3
FOM (pm^2/V^2):	196	161	6	44
Crystal acceptance angle (mrad·mm):	41.3	10.0	30.9	54.3
Temperature range (K·mm):	157.9	507.9	335.3	1389.4
Idler bandwidth (THz·mm):	4.59	8.43	11.83	4.39
GVM (fs/mm):	220	120	83	227
Spatial walk-off (mrad):	11.87	56.55	20.79	10.83
Mixing scheme pumped by $\lambda_p = 1.03\ \mu m$:		o+o=e	o+o=e	
PM angle (°):		13.8	36.1	
D_{eff} (pm/V):		59.5	9.63	
FOM (pm^2/V^2):		170	7	
Crystal acceptance angle (mrad·mm):	n/a	5.7	20.3	n/a
Temperature range (K·mm):		53.9	282.0	
Idler bandwidth (THz·mm):		1.75	4.92	
GVM (fs/mm):		574	203	
Spatial walk-off (mrad):		65.41	20.81	

Table 2.3: Comparison of Type-II DFG performance in different nonlinear crystals pump at different wavelengths. ZGP: $ZnGeP_2$. AGS: $AgGaS_2$. AGSe: $AgGaSe_2$. PM: phase matching. D_{eff}: effective nonlinear coefficient. FOM: figure of merit. GVM: group-velocity mismatch. The data were adapted from Reference [149].

Type II DFG Performance	ZGP	GaSe		AGS	AGSe
Mixing scheme pumped by $\lambda_p = 2.9\ \mu m$:	o+e=o	e+o=e	o+e=e	e+o=e	e+o=e
PM angle (°):	64.8	13.0	22.8	49.0	50.9
D_{eff} (pm/V):	72.5	52.1	43.8	14.2	33.7
FOM (pm^2/V^2):	174	137	100	15	65
Crystal acceptance angle (mrad·mm):	131	22.8	42.3	75.3	126.1
Temperature range (K·mm):	342.3	n/a	4290.4	511.5	1825.3
Idler bandwidth (THz·mm):	7.07	19.6	4.10	5.75	n/a
GVM (fs/mm):	143	50	274	173	20
Spatial walk-off (mrad):	9.45	63.76	99.44	23.92	12.75
Mixing scheme pumped by $\lambda_p = 1.95\ \mu m$:	o+e=o	e+o=e	o+e=e	e+o=e	e+o=e
PM angle (°):	59.9	12.2	28.1	39.3	51.1
D_{eff} (pm/V):	71.3	53.9	39.4	14.7	34.5
FOM (pm^2/V^2):	166	145	82	16.1	67
Crystal acceptance angle (mrad·mm):	68.4	14.6	37.2	45.2	79.7
Temperature range (K·mm):	226.6	1544.2	454.9	372.5	1454.9
Idler bandwidth (THz·mm):	16.9	19.2	4.35	9.2	7.64
GVM (fs/mm):	60	50	290	110	130
Spatial walk-off (mrad):	10.88	60.08	113.08	23.89	12.73
Mixing scheme pumped by $\lambda_p = 1.55\ \mu m$:	o+e=o	e+o=e	o+e=e	e+o=e	e+o=e
PM angle (°):	64.4	12.5	33.8	37.2	57.6
D_{eff} (pm/V):	76.4	54.6	33.8	14.8	32.5
FOM (pm^2/V^2):	188	148	61	16	59
Crystal acceptance angle (mrad·mm):	55.2	10.8	34.4	34.9	70.0
Temperature range (K·mm):	158.8	426.4	142.4	316.1	2795.3
Idler bandwidth (THz·mm):	3.04	5.84	4.58	31.78	3.36
GVM (fs/mm):	330	170	300	30	297
Spatial walk-off (mrad):	10.20	61.51	122.84	23.52	11.74
Mixing scheme pumped by $\lambda_p = 1.03\ \mu m$:		e+o=e	o+e=e	e+o=e	
PM angle (°):		14.5	57.0	38.3	
D_{eff} (pm/V):		56.1	12.7	15.6	
FOM (pm^2/V^2):		152	9	18	
Crystal acceptance angle (mrad·mm):	n/a	6.0	40.0	22.1	n/a
Temperature range (K·mm):		49.3	18.0	301.5	
Idler bandwidth (THz·mm):		1.55	5.67	3.81	
GVM (fs/mm):		647	340	260	
Spatial walk-off (mrad):		70.10	109.13	23.72	

short pulse generation by the DFG technique using an all-fluoride fiber laser operating in the mid-IR wavelength region was reported. The LWIR pulses have 1.25-mW output power with a spectrum centered at 11 µm and a repetition rate of 48 MHz. The DFG pump pulses are generated from an Er:ZBLAN fiber oscillator and nonlinear amplifier, which was previously reported in Reference [144]. The demonstration of a tunable mid-IR fluoride fiber laser source covering 2.8 to beyond 4 µm was also reported, which implements a compact and practical design that uses SSFS. The shifted soliton pulses at 4 µm have a pulse energy of 6 nJ and 120-fs pulse duration. This research opens new paths for developing intense mid-IR and LWIR ultrashort pulse sources suitable for a wide range of potential applications.

2.2 Experimental Setup and Results

The schematic of the DFG system for LWIR pulse generation using ZBLAN fiber nonlinear soliton amplifier and Raman soliton wavelength shifter is shown in Figure 2.1. An Er:ZBLAN mode-locked fiber oscillator injects ∼2 nJ ultrashort pulses at 2.8 µm with a repetition rate of 48 MHz into a nonlinear Er:ZBLAN amplifier, which increases pulse energies to 50 nJ simultaneously compressing them via soliton-effects to ∼85 fs [144]. The amplifier output is split into two arms: one serves as the 2.9 µm DFG pump beam, and the other is coupled into an 8-m long InF_3 fiber to produce DFG signal beam which is shifted to ∼4 µm. The splitting into two arms is achieved with a Polarizing Beamsplitter (PBS), with a Half-waveplate (HWP) in front of it controlling the splitting ratio. Beams from the two arms are recombined with another PBS, and focused into the ZGP crystal where LWIR pulses centered at 11 µm with an FWHM spectral bandwidth of ∼1.3 µm are generated as the difference-frequency between the pump and

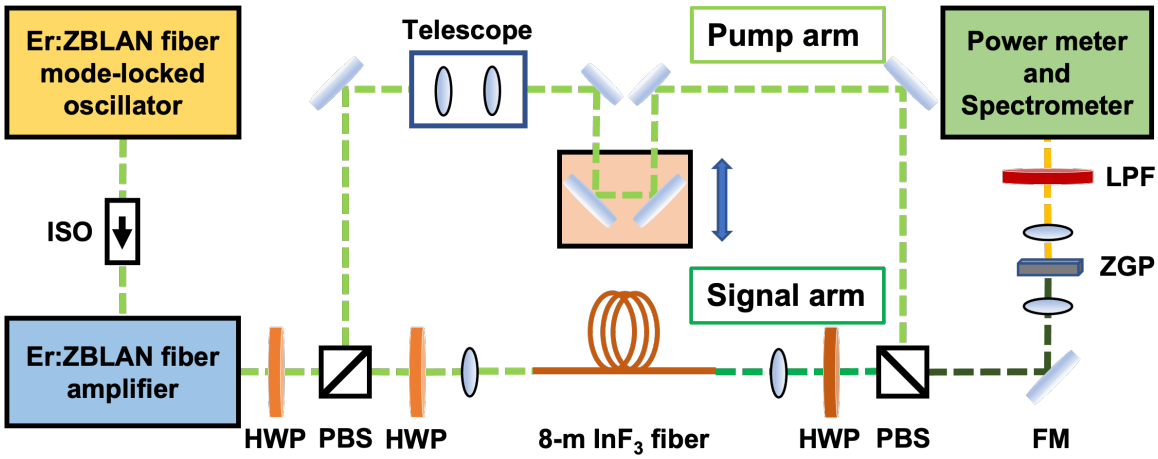

Figure 2.1: The schematic of LWIR pulse generation using DFG. ISO: isolator, HWP: half-wave plate, PBS: polarizing beamsplitter, LPF: long-pass filter, FM: flip mirror. Reprinted with permission from [126] © The Optical Society.

signal beams. The pump arm contains an adjustable free-space delay line for achieving temporal overlap between pump and signal pulses in the DFG crystal.

The spectrum of the pump pulses from the amplifier (measured before the InF_3 fiber) is shown in Figure 2.2(a). The central wavelength of the fundamental soliton, containing most of the energy, is slightly red-shifted to 2.925 µm via SSFS [143], [150]. Amplifier output also contains a weak residual pulse, resulting from the fraction of the amplifier input pulse which did not couple into the main soliton during nonlinear amplification, and thus remains at the ∼2.8 µm central wavelength, separated from the amplified soliton pulse spectrally and temporally [144].

In the signal arm, these pump pulses are injected (with 56% coupling efficiency) into an 8-m long InF_3 fiber with a 7.5-µm diameter core (NA=0.3) and a 125-µm diameter cladding (Le Verre Fluore) for wavelength shifting up to ∼4 µm using SSFS. Both of the InF_3 fiber ends are splice-protected with AlF_3 glass endcaps (AFG 70/125, 0.2 NA, Le Verre Fluore) to prevent fiber end degradation and damage. Each endcap

is angle polished to 8° to avoid optical feedback into the fiber amplifier. Increasing input power into the InF_3 fiber (by adjusting the HWP before the beam-splitting PBS) increases the SSFS towards longer wavelengths. The wavelength-shifted output spectra for several total output average powers are shown in Figure 2.2(b) (measured using an optical spectrum analyzer AQ6377, YOKOGAWA). The maximum SSFS to ∼4 µm was obtained with the 940-mW incident average power (19.5-nJ pulse energy) at the InF_3 fiber input. The corresponding total average output power is 520 mW, with 290-mW measured in the wavelength-shifted portion of the spectrum (corresponding to 6.04-nJ in wavelength-shifted signal pulses). Signal power was measured after a bandpass filter (FB4000-500, Thorlabs), centered at 4 µm with a 500-nm bandwidth. This indicates 30.8% pump-to-signal conversion efficiency at this incident power. The pulse duration of the soliton pulse centered at around 4 µm was measured to be 120 fs using a TPA-based autocorrelator, assuming a $sech^2$ shape, as shown in Figure 2.2(c). A 30-minute measurement of the average power of the main soliton was taken to characterize its stability, and the result indicates the RMS stability of 0.35%.

To understand experimental observations, numerical simulations using the model from Reference [144] were carried out. Simulation results in time and spectral domains, corresponding to the experimental conditions producing the ∼4 µm SSFS signal, are shown in Figure 2.3. The model includes soliton compression in the 3-m long Er:ZBLAN fiber amplifier followed by the SSFS in the 8-m long InF_3 fiber. 1.9-nJ and 230-fs input pulses are amplified and soliton-compressed after 3-m of Er:ZBLAN fiber to ∼40 nJ and ∼90 fs in the main soliton pulse [144]. (In Figure 2.3, the 90 fs output pulse trace appears wider than the 230 fs input trace due to the logarithmic scale of the plotted intensities). Fraction of ∼11.4 nJ of these pump pulses is injected into the 8-m InF_3 fiber. Due to the injected energy exceeding the fundamental-soliton energy, soliton fission occurs

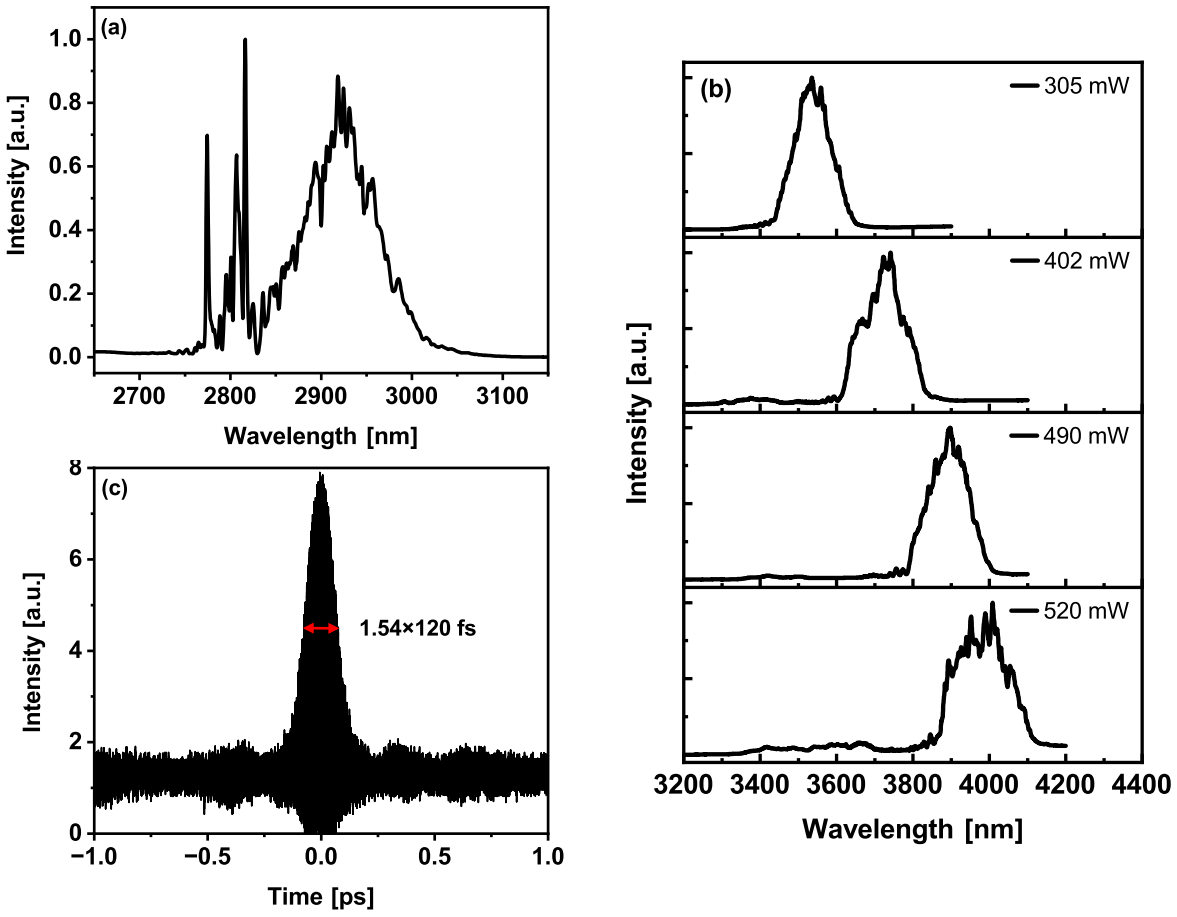

Figure 2.2: Experimental results of SSFS input and outputs. (a) Amplified soliton spectrum measured at the InF_3 fiber input; (b) Tunable SSFS output spectra with increasing output power; (c) Autocorrelation measurement of the shifted soliton pulse at ∼4 µm ($sech^2$ shape). Reprinted with permission from [126] © The Optical Society.

at the beginning of the fiber, splitting the input pulse into several fundamental-soliton pulses [147]. The soliton pulse with the highest energy undergoes the largest SSFS to ∼4 µm, and is used as the DFG signal. Because it is well separated from other pulses both spectrally and temporally, it can be overlapped with the ∼2.9 µm pump pulse without interference with the other pulses. Note that, while the qualitative picture agrees well with experimental observations, there is numerical discrepancy between the simulated 4 µm soliton energy of 3.4 nJ and 85 fs duration, and the measured values of 6.04 nJ and 120 fs, attributable to a limited accuracy of the known ZBLAN fiber Raman-gain parameters.

In the DFG stage, the main pulse output from the nonlinear amplifier (centered at ∼2.9 µm, Figure 2.2(a)) and the signal pulse at ∼4 µm (Figure 2.2(b), bottom panel) were mixed. A type-I ZGP crystal was used in this work for the DFG process $\omega_{idler}(e) + \omega_{signal}(e) = \omega_{pump}(o)$, where idler, signal, and pump have wavelengths of 11, 4.0 and 2.9 µm, respectively. The ZGP crystal (from MolTech GmbH) has a cut angle of θ=50°, ϕ=0° and dimensions of $10 \times 10 \times 0.75$ mm^3. For 0.75-mm thick ZGP crystal, the GVM is 12.5 fs between pump and signal, 155 fs between pump and idler. The simulated pulse duration of idler is 159 fs. The spatial walk-off angle is 12 mrad between pump and signal and between pump and idler. The pump and signal pulses are combined at a PBS and collinearly focused onto the ZGP crystal, with pulse energies of 8.3 nJ and 4.6 nJ, respectively. Independently adjusting the telescope in the pump arm and the collimating lens after InF_3 fiber in the signal arm was performed to ensure identical focal spot sizes for pump and signal on the ZGP crystal. The focal spot size was ∼50 µm, and their near-field and far-field overlaps were verified by a mid-IR beam profiler (WinCamD-IR-BB, Dataray). The temporal overlap of the two arms was set by manually adjusting the delay line. Calculated intensity for the ∼100 fs pulses with

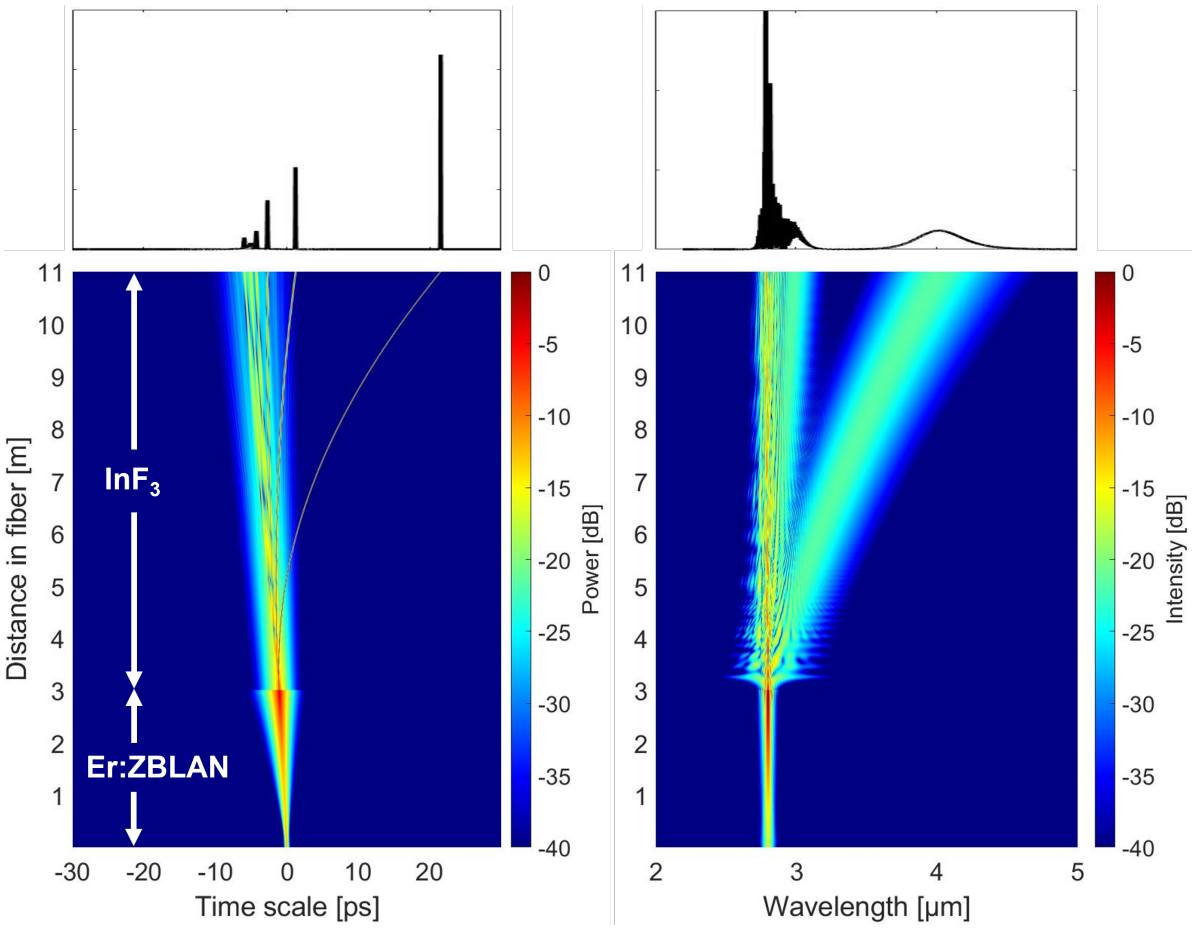

Figure 2.3: Simulation of the pulse propagation in the laser system in the time (left column) and spectral domain (right column). Top row: InF_3 fiber output. Reprinted with permission from [126] © The Optical Society.

the total combined pump and signal energy of ∼14 nJ focused into this 50 µm spot is ∼7 GW/cm^2, which is much smaller than the reported >150 GW/cm^2 damage threshold for 130 fs pulses at 1.3 µm [105].

The LWIR pulse train was first detected by a mercury-cadmium-telluride detector (PVI-4TE-10.6, Vigo) after a 7.3 µm long-pass filter (7.30ILP-25, Andover Corporation). The polar and azimuthal angles of the ZGP crystal were adjusted to maximize the LWIR pulse energy. A maximum average power of 1.25 mW was measured for LWIR pulses centered at 11 µm using a thermopile power meter (Newport), corresponding to 26 pJ of pulse energy. The conversion efficiency with respect to the DFG pump pulse is 0.3%. The LWIR idler spectrum was characterized by a homemade single-shot ZnSe prism-based spectrometer with a pyroelectric line array sensor (Pyreos Ltd.). The spectrometer was calibrated using ammonia absorption features [151] and determined to have a resolution of ∼100 nm in the LWIR region. The output spectrum is shown in Figure 2.4 and is centered at 11 µm, with ∼1.3 µm FWHM spectral bandwidth. The spectrum supports the generation of three-cycle transform-limited LWIR pulses if compressed with flat spectral phase.

To demonstrate the wavelength tunability of our system towards the shorter wavelength portion of the 8–12 µm LWIR atmospheric transmission window, the experiment of mixing the weak satellite pump pulses (centered at ∼2.8 µm, Figure 2.2(a)) with signal pulses at ∼4 µm (Figure 2.2(b), bottom panel) in a ZGP crystal (from Dien Tech) was also conducted. The generated LWIR pulses are centered at 9.7 µm, with ∼1.3 µm FWHM spectral bandwidth and up to 0.4-mW average power (Figure 2.4). Simulations of type-I DFG were performed to further study the wavelength tunability in the 8–12 µm LWIR region, including the two phase-matching conditions in the experiments discussed above. In the DFG process, the pulses propagate through the ZGP crystal and undergo

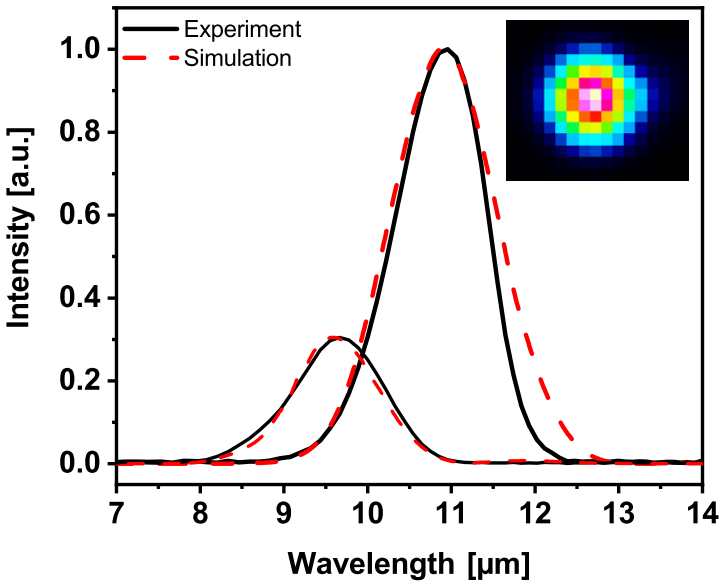

Figure 2.4: Experimental (solid black) and simulated (dashed red) LWIR spectra. Left: DFG pumped with weak ∼2.8 µm satellite pulses; right: DFG pumped with energetic ∼2.9 µm main pulses. Inset: near-field LWIR beam profile. Reprinted with permission from [126] © The Optical Society.

simultaneous linear absorption [86], dispersion, and amplification. These processes were modeled using coupled three-wave mixing equations which were solved with the standard split-step Fourier method [125]. Simulated LWIR spectra (dashed red) are shown in Figure 2.4 and agree well with the results of our experiment (Figure 2.4, solid black). Our simulated results (not shown in this work) demonstrate the LWIR pulse generation covering the entire 8–12 µm region by mixing ∼2.9 µm pump pulses and wavelength-tunable SSFS signal pulses in the ZGP crystal and is only limited by the ZGP linear absorption above ∼12 µm.

The near-field LWIR beam profile was characterized by the same beam profiler mentioned above, and shown in Figure 2.4 inset. The measured near-Gaussian beam profile illustrates the beam-quality advantage of using in-fiber generated pump and signal pulses. The observed LWIR beam profile and its position appeared to be stable.

2.3 Conclusion and Discussions

In summary, to the best of our knowledge, the first milliwatt broadband LWIR source driven by a femtosecond mid-IR fluoride fiber laser was demonstrated. LWIR pulses centered at 11 µm with an average power of 1.25 mW were generated in a ZGP crystal. The generated LWIR spectrum has an FWHM bandwidth of ∼1.3 µm, compatible with three-cycle transform-limited pulses. The LWIR output beam has a near-Gaussian profile.

Fluoride fiber-based soliton amplifiers and wavelength shifters operating in mid-IR offer much higher energies than are achievable in NIR, and thus have the potential of much higher LWIR powers and conversion efficiencies. The conversion efficiency in the reported experiment was limited by the timing instability between the ∼4 µm signal

and the ∼2.9 µm pump pulses due to the long length of the InF_3 fiber. Our analysis indicates that this instability could be sufficiently reduced by (i) increasing energies into the SSFS fiber, and thus shortening the required fiber length, leading to reduced timing instability [152], and (ii) using active feedback for controlling the free-space delay to actively compensate this timing instability [84]. With these improvements, nJ-level LWIR ultrashort pulses with tens of milliwatt average power should be expected.

Chapter 3

Generation of Ultra-broadband Long-wave Infrared Pulses Assisted by Genetic Algorithm Optimization

3.1 Introduction

The generation of bright coherent radiation in the LWIR region is of vital interest for fundamental science and diverse applications, for instance HHG [38], Laser Wakefield Acceleration (LWFA) [8], and mega-filament generation in the atmosphere [62].

This Chapter is based on the previously published articles:

H. Huang, X. Xiao, M. Burger, J. Nees, and I. Jovanovic, "Ultra-broadband long-wave-infrared pulse production using a chirped-pulse difference-frequency generation," *Optics Letters*, vol. 47, no. 13, pp. 3159–3162, 2022. [49]

H. Huang, X. Xiao, J. Nees, and I. Jovanovic, "Broadband long-wave infrared pulse generation using chirped-pulse difference-frequency mixing," in *CLEO: Science and Innovations*, Optica Publishing Group, 2022, STh4E–4. [153]

H. Huang, X. Xiao, J. Nees, and I. Jovanovic, "Genetic algorithm optimization for ultra-broadband long-wave infrared seed pulse generation," in *2021 Conference on Lasers and Electro-Optics (CLEO)*, IEEE, 2021, pp. 1–2. [154]

Terawatt-class LWIR pulses have been produced from CO_2 lasers by direct amplification [68] or using CPA [69]. However, the amplification bandwidth of CO_2 limits the LWIR pulses to picosecond duration, on the order of tens of optical cycles. A CO_2 system also confronts other considerable constraints such as low repetition rate and large footprint. To circumvent these constraints, several approaches have been developed, including the use of high-pressure mixed-isotope amplifiers [69], optical pumping by Fe:ZnSe laser [70], [71] and nonlinear pulse compression [72], [73]. Solid-state OPCPA [30], [77] has been drawing significant attention as an alternative method with the potential to produce high peak and average power LWIR pulses due to its broad bandwidth and wavelength agility.

Although not yet demonstrated at a center wavelength of 10 µm, OPCPA development displays a trend towards few-cycle pulse generation in the LWIR regime. In recent years, OPCPAs operating near 4 µm [155], [156], 5 µm [157]–[159], 7 µm [160], [161], and 9 µm [162] have been demonstrated. This trend highlights the potential for broadband LWIR, CEP-stable, solid-state counterparts to the TW-class CO_2 lasers to be demonstrated in the near future. To seed such OPCPA systems, a broadband seed source at a center wavelength of 10 µm is needed.

DFG in non-oxide nonlinear crystals employing control over input pulse spectral amplitude and phase is a promising candidate technique for production of broadband seed that supports few-cycle pulse generation in the LWIR range. Table 3.1 summarizes the generation of LWIR pulses driven by Ti:sapphire laser using different configurations. Several DFG approaches based on AGS and GaSe have been presented in the past [164], [169], [171], [173]. However, to circumvent TPA in these crystals, most approaches adopted two-stage schemes, in which the output from the Ti:sapphire CPA was first downconverted to the NIR and then followed by DFG. In addition to reduced

Table 3.1: Summary of LWIR pulses generation pumped by Ti:sapphire laser. NLCs: nonlinear crystals. AGS: $AgGaS_2$. AGSe: $AgGaSe_2$. Osc: oscillator. Regen: regenerative amplifier.

NLCs-type, θ_{cut}	L (mm)	λ_0 (μm)	$\Delta\lambda$ (μm)	Scheme	Ref.
AGS, 44°	1	9	n/a	Single-cavity, double-slit Osc	[163]
AGS-I, 40°	2	9.5	1.5	OPG/OPA (LBO/BBO)	[164]
AGS, 47°	5	9.7	n/a	2 synchronized Osc	[165]
AGSe-II, 66°	2	11.2	1	OPO(KTP)	[166]
AGS	20	11	n/a	AOPDF-tuned Osc	[167]
GaSe	1	10	2.5	OPG/OPA (Sapphire/BBO)	[168]
AGS-I, 40.5°	0.3	10	1	OPG (BBO)	[169]
AGS-II	1	9.7	0.32	Double-cavity Osc	[107]
AGS-II	1	9.85	0.28	Double-cavity Osc	[170]
AGS-II	1	11	n/a	Etalon-tuned Regen	[171]
AGS-I, 45°	1	11	2	Spectral filtering	[172]

conversion efficiency and greater complexity, the CEP was also random in schemes that employ optical parametric generation [174]. Broadband LWIR pulses were generated via noncollinear phase-matching [172], but the angular dispersion has to be carefully compensated for seeding OPCPA [175].

In this work, a compact single-stage approach for generating LWIR seed by DFG of two-color chirped Ti:sapphire CPA output with a collinear geometry was demonstrated, which is referred to as Chirped-pulse Difference-frequency Generation (CP-DFG). Compared to conventional DFG, CP-DFG offers several potential advantages such as reduced TPA, higher efficiency, and increased phase-matching bandwidth [176]. Indirect manipulation of the chirp of LWIR pulses can also be realized through tuning the chirp of Ti:sapphire CPA output, which can facilitate the recently developed Double-chirped Optical Parametric Amplification (DC-OPA) scheme [177], [178] in the LWIR region.

The CP-DFG operates by mixing spectral components that originate from the same pulse. Consequently, the shortest wavelength that can be generated is determined by

the frequency separation between the extrema of its spectrum. In many Ti:sapphire CPA systems, the gain-narrowing effect limits the amplified bandwidth to ∼40 nm, which is too narrow for LWIR pulse generation in the 8–12 µm atmospheric transmission region. Therefore, to achieve broader amplified bandwidth, spectral shaping is necessary to overcome gain narrowing. In this work, a nitrocellulose pellicle was placed inside the Ti:sapphire regenerative amplifier to introduce a loss near the peak of the gain profile. The amplified spectrum has two peaks with a separation of ∼60 nm. Unlike the spectral shaping techniques based on adjustable air-spaced etalon [179], a single-pellicle configuration is not alignment-critical and can easily be implemented in Ti:sapphire regenerative amplifiers with minimal introduction of material dispersion.

The chirp and interpulse delay of two-color pulses mixed in the nonlinear crystal also affects the bandwidth of the generated LWIR pulse. To obtain even broader bandwidths, tailoring of the chirp is crucial. However, the number and range of parameters that play a role in the CP-DFG process makes it time-consuming to search for their optimum combination for bandwidth control. Under our simulation conditions, for instance, the parameter space has at least 10^{40} distinct points. As a result, the implementation of an algorithm to traverse the parameter space in an efficient manner is favored. Evolutionary algorithms and, in particular, the GA, represent an efficient optimization strategy. GA is inspired by mechanisms of biological evolution and has been used in many prior studies, such as those involving nonlinear pulse propagation [180] and self-starting mode locking [181].

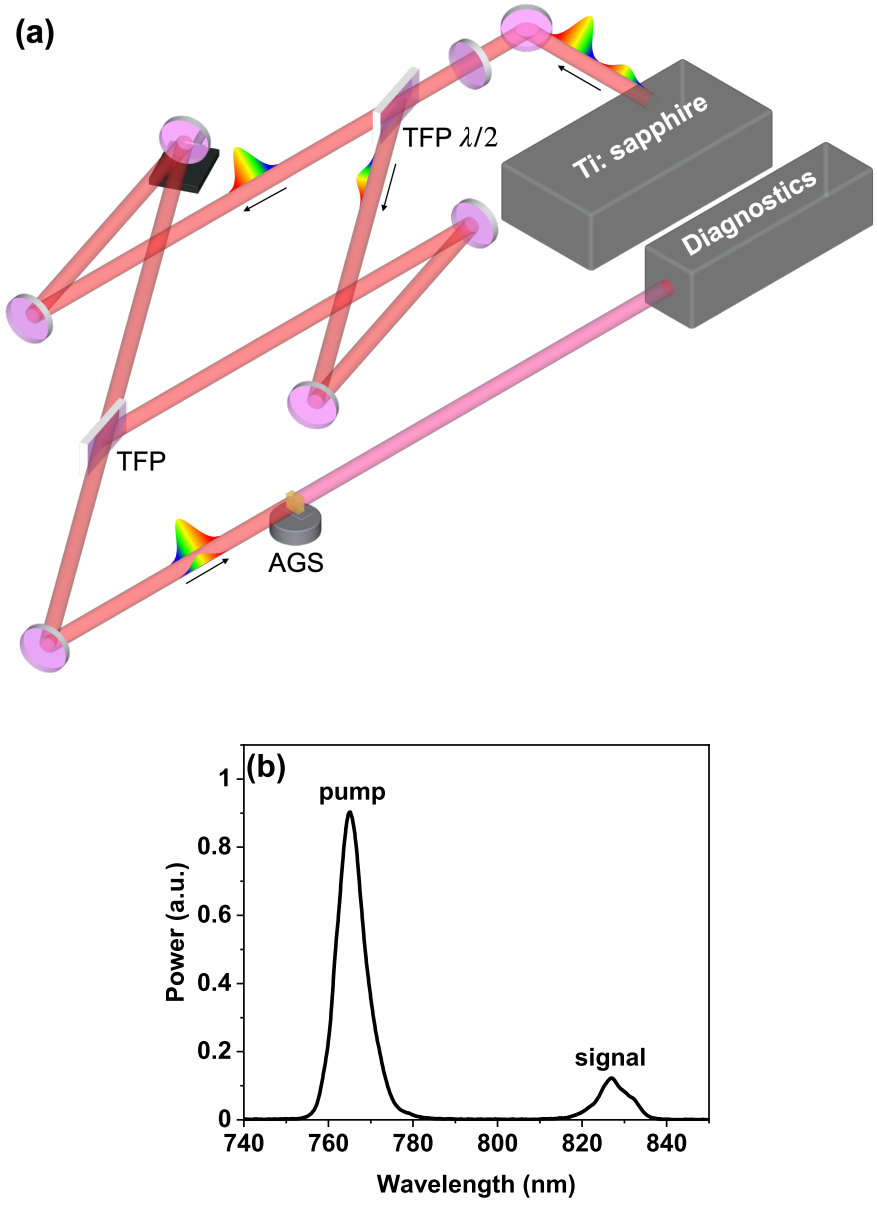

Figure 3.1: (a) Experimental setup for LWIR seed generation via CP-DFG. TFP: thin-film polarizer; λ/2: half-wave plate. (b) Output spectrum of the Ti:sapphire CPA system modified by pellicle inserted into the regenerative amplifier. Reprinted with permission from [49] © The Optical Society.

3.2 Experimental Setup

The laser used in this work is a custom-built Ti:sapphire CPA system that delivers >22-mJ, ∼40-fs pulses at 480 Hz. The nitrocellulose pellicle with a thickness of 2 µm was placed into the regenerative amplifier with ∼45° angle of incidence. The compressed pulses were resized to a 5-mm diameter by a 5× Galilean reflective telescope.

The experimental setup is illustrated in Figure 3.1a. Briefly, the two-color Ti:sapphire output passes through a half-wave plate and is separated by a Thin-film Polarizer (TFP). The ratio of energy in the upper (pump) to lower (signal) arm can be adjusted by rotating the half-wave plate. The translation stage in one arm is used to adjust the delay between pump and signal, which are then combined at another TFP and passed through the AGS crystal to generate idler at their difference frequency. The compact design allows the CP-DFG setup to be accommodated within a 1×1 ft^2 area.

A type-II AGS crystal with a cut angle of θ=45.4°, ϕ=0° and dimensions of $5 \times 5 \times 0.4$ mm^3 was used to strike a balance between the LWIR bandwidth and conversion efficiency. Further increase of spectral bandwidth is realized by the use of chirped-pulse mixing. An Acousto-optic Programmable Dispersive Filter (AOPDF) (Fastlite Dazzler) was applied after the Ti:sapphire oscillator to shape the spectral phase of both the pump and signal pulses for this purpose.

The LWIR idler spectrum was characterized by a homemade single-shot ZnSe prism-based spectrometer with a pyroelectric line array sensor (Pyreos Ltd.). The spectrometer was calibrated using ammonia absorption features [151] and determined to have a resolution of ∼100 nm in the 8–12 µm LWIR region.

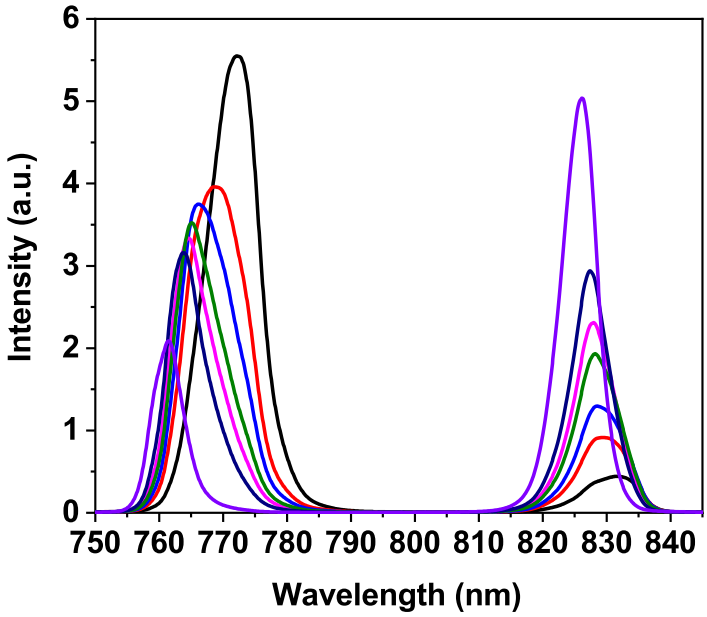

Figure 3.2: Wavelength tunability of the Ti:sapphire CPA system accessible by adjusting the pellicle inserted into the regenerative amplifier.

3.3 Results and Discussion

A typical spectrum of pump and signal pulse centered at 765 nm and 826 nm is shown in Figure 3.1b. The full tunable range accessible by adjusting the azimuthal angle of the pellicle is shown in Figure 3.2. The separations between the central wavelengths of the pump and signal correspond to idler wavelengths of 9.7–10.8 µm. The type-II DFG process used is $\omega_{idler}(e) + \omega_{signal}(o) = \omega_{pump}(e)$, where idler, signal, and pump have wavelengths of 10.4, 0.826 and 0.765 µm, respectively.

To find the optimized thickness of AGS crystal, a simulation of DFG with various crystal thicknesses was performed. In the DFG process, the pulses propagate through AGS crystal and undergo simultaneous linear absorption [169], TPA [107], dispersion, and amplification. These processes were modeled using coupled three-wave mixing equations [182] and solved with the standard split-step Fourier method [125]. Transform-limited pump and signal with the spectrum shown in Figure 3.1b are used in the simulation. The interpulse delay is set to zero. LWIR spectra generated from several crystal thicknesses are shown in Figure 3.3a. The broadest bandwidth is achieved in the shortest crystal at a cost of low conversion efficiency. After ∼0.4 mm, back conversion starts to take effect, which narrows the spectrum. 0.4 mm was chosen to be the optimum crystal length on the basis of the combination of its conversion efficiency and bandwidth. The generated idler spectrum (∼1-µm FWHM) is shown in Figure 3.3b (solid black) and agrees well with the result of simulation (Figure 3.3b, dashed red). The measured pulse energy was ∼100 nJ, giving a conversion efficiency of 0.05%.

To further broaden the LWIR spectrum using GA, nine different parameters were selected as genes, including up to fourth-order spectral phase of pump and signal pulses, the ratio between pump and signal pulse energy, interpulse delay, and crystal orien-

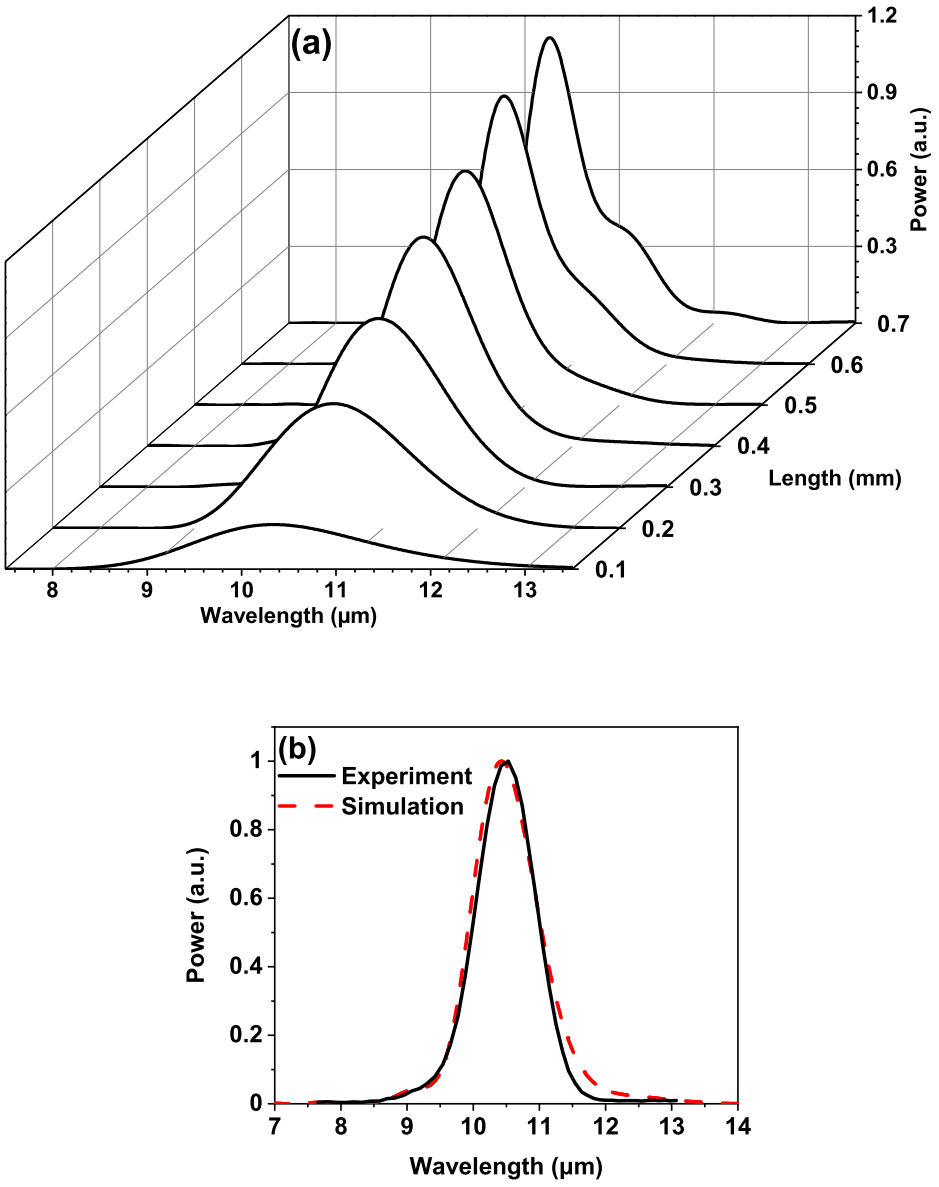

Figure 3.3: (a) Simulated LWIR spectra generated from different thicknesses of AGS crystals. The simulation parameters are provided in the text. (b) Spectra of generated LWIR pulses by mixing transform-limited input pulses: solid black – experiment; dashed red – simulation. Reprinted with permission from [49] © The Optical Society.

tation angle θ. Figure 3.4a shows the evolution of the spectral bandwidth of the five broadest LWIR seed pulses simulated in each generation. The algorithm converges after ∼20 generations. With optimized parameters, the generated LWIR spectrum is shown in Figure 3.4b (solid black). The pulse energy in this case is ∼110 nJ, giving a conversion efficiency of ∼0.07%. By adjusting the interpulse delay and the input chirp, the bandwidth of LWIR pulses was broadened by a factor of three. If compressed with flat spectral phase, such a broad spectrum supports two-cycle (∼73 fs) pulses at a center wavelength of 10.5 µm.

The GA predicted phases are 2630 fs^2, −140 fs^3, and 7020 fs^4 for pump; and 720 fs^2, 33540 fs^3, and 87060 fs^4 for signal. The other optimized parameters are 1.1 for pump-to-signal pulse energy ratio, −90 fs for interpulse delay, and 45.8° for crystal orientation angle θ. Figure 3.5 illustrates the calculated conversion efficiency for the DFG process of mixing different pump and signal wavelengths and normalizing to the two central wavelengths. A pattern with a positive slope was observed, which indicates that mixing the same portion of pump and signal spectra is more efficient. That is to say, mixing the shorter wavelength portion of the pump and signal spectra and the longer wavelength portion of the pump and signal spectra is more efficient than mixing the opposite parts of the spectra. Furthermore, the Group Delay Dispersion (GDD) of pump and signal in 0.4-mm AGS crystal are 415 fs^2 and 333 fs^2, respectively. Therefore, a positive chirp is preferred to broaden the idler spectrum since it also mitigates the GVM. A previous study demonstrated the narrowing of idler bandwidth by equally chirping pump and signal pulses [158]. In contrast, the different chirps predicted by GA would notably broaden the LWIR spectrum. In summary, the larger positive chirp of the pump and smaller positive chirp of the signal accompanied by the optimized interpulse delay compensate for the GVM and improve the conversion efficiency in the DFG process, thus

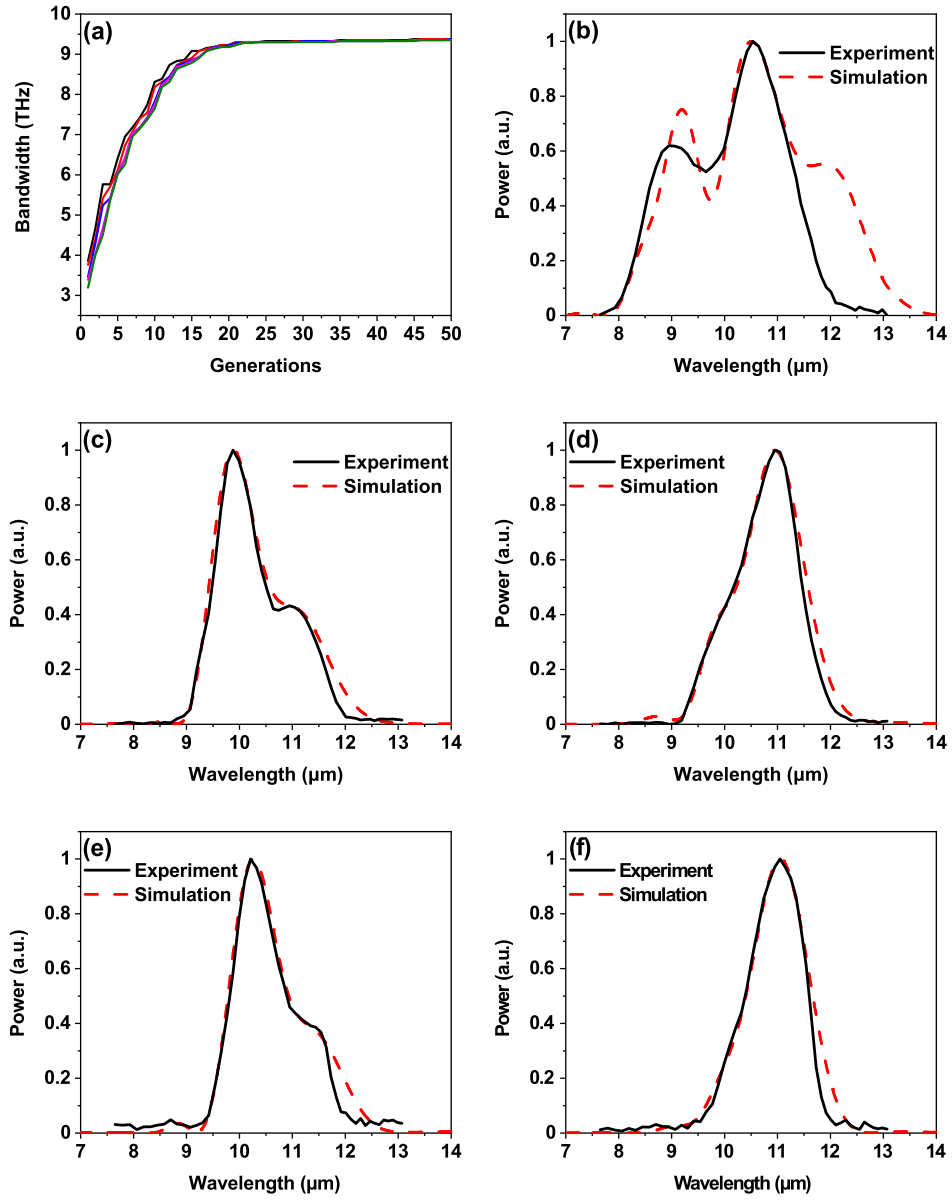

Figure 3.4: (a) Evolution of the spectral bandwidth of the five broadest LWIR seeds. (b) – (d) Experimental (solid black) and simulated (dashed red) results of LWIR seed spectrum generated with the same GA-optimized phase and other parameters listed in the text but different delays between pump and signal. (b) -90 fs. (c) -30 fs. (d) $+50$ fs. (e), (f) Experimental (solid black) and simulated (dashed red) results of LWIR seed spectrum generated with different chirps and zero interpulse delay. (e) Pump: $+2000$ fs^2, signal: 0 fs^2. (f) Pump: 0 fs^2, signal: -2000 fs^2. Reprinted with permission from [49] © The Optical Society.

broadening the LWIR spectrum.

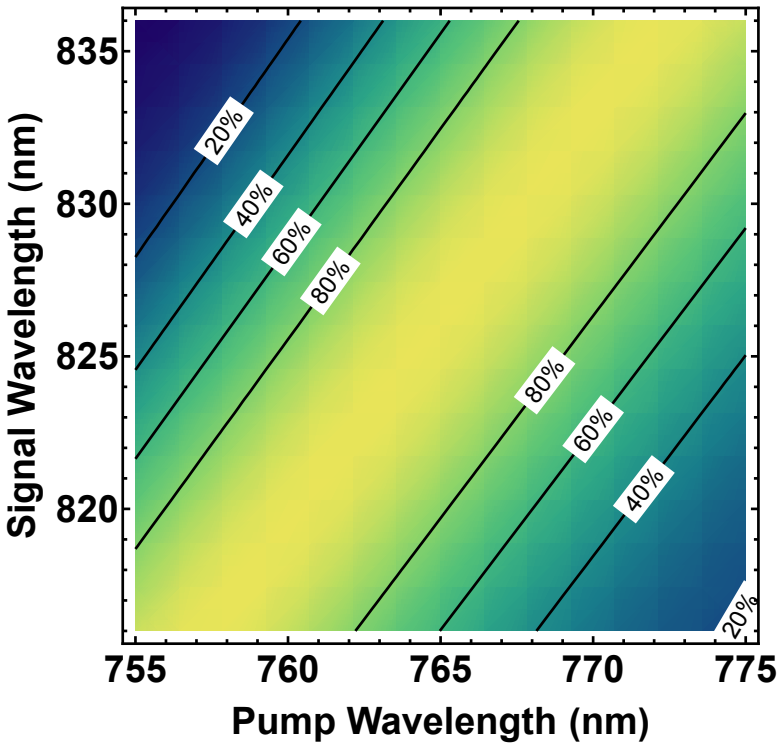

Figure 3.5: Conversion efficiency of the DFG process with respect to the mixing of the two central wavelengths. Adapted with permission from [49] © The Optical Society.

Compared to the experimental result (Figure 3.4b, solid black), the simulated spectrum (Figure 3.4b, dashed red) has a broader bandwidth spanning from 8 to 13.5 µm. To study the reason for the discrepancy and validate our DFG model, four additional experiments with different interpulse delays or chirps were performed. The results are shown in Figure 3.4c – 3.4f. These four experimental results agree better with the simulation with a slight discrepancy in the longer wavelength part of the spectrum. The discrepancy occurs in the region longer than 11.5 µm, which may originate from the absorption of AGS crystal. In our simulation, the transmission data of AGS was adopted from Reference [169] with a cutoff wavelength at ∼13 µm. However, shorter

cutoff wavelength has also been reported [183].

3.4 Conclusion

In conclusion, a simple single-stage scheme for broadband generation of LWIR pulses that could serve as a low-energy seed source for OPCPA was demonstrated. A 2-µm nitrocellulose pellicle was used in the regenerative amplifier of Ti:sapphire CPA system to modify its gain profile. Amplified two-color spectrum centered at 765 nm and 826 nm was spatially and temporally overlapped on a 0.4-mm AGS crystal. LWIR pulses with a ∼1-µm FWHM bandwidth were produced with transform-limited input pulses. By optimizing the chirp and delay of the two-color NIR pulses using GA, LWIR pulses with an FWHM bandwidth of ∼3 µm were generated, supporting the production of two-cycle transform-limited pulses that span the majority of the 8–12 µm atmospheric transmission window. The CEP of broadband LWIR pulses is expected to be passively stabilized due to the shared origin of amplified two-color pulses used in DFG [184].

Future work would be beneficial to employ the GA *in situ* with real-time fitness feedback from diagnostics, for instance, spectral bandwidth measured by a spectrometer. However, in such a scheme, more constraints are needed to avoid potential damage in the Ti:sapphire CPA system that can occur due to inadvertent bandwidth narrowing. In this work, the objective was solely to broaden the LWIR bandwidth for seeding an LWIR OPCPA. In the cases where the conversion efficiency holds a greater importance for the application, the GA may be used to strike a more favorable balance between the LWIR bandwidth and conversion efficiency.

Chapter 4

Optimization of Laser Beam Pointing Stability Using Active Method

4.1 Introduction

As high-power laser systems continue to advance in capabilities, the explorations of the research fields enabled by this technology have extensively expanded [185]–[190]. Tightly-focused high-peak-power laser pulses with intensity exceeding 10^{18} W/cm^2 open new horizons in the relativistic optics regime. For many applications, the preferred extreme intensity greater than 10^{22} W/cm^2 [191], [192] or even 10^{23} W/cm^2 [193] is only obtainable within micrometer-sized focal spot. Therefore, taking full advantage of these lasers' high peak power and high intensity requires precise control of the laser beam pointing. The flagship experiment proposed for the ZEUS aims to collide a wakefield-

This Chapter presents research separate from the previous Chapters.

accelerated electron beam with a focused ultrashort laser pulse [25]. The diameter of the electron beam at the interaction point from this experiment should be less than 100 µm. The position deviation of the focused laser pulses must be within the electron beam diameter such that the interaction between them can be realized. This requires both the wakefield-driver laser and the laser interacting with the electron beam to have minimal pointing instability (a few µrad). The quantum electrodynamics regime can be explored through such experiments producing electron-positron pairs through the collision of high energy electrons and photons [194]. A proof-of-principle active beam-pointing stabilization system in ZEUS is presented. The system will also facilitate LWFA experiments, which were devised nearly four decades ago [7], providing an attractive scheme for compact particle acceleration. The production of relativistic electron beams with a narrow energy spread has been demonstrated by LWFA [187], [188].

The efforts made towards active control of beam-pointing in a high-power laser system can be classified into three categories: experimental results of compensating short (and long) term beam-pointing fluctuations [195]–[200], experimental results of compensating long term only beam-pointing fluctuations [201]–[205], and control algorithms and simulated results [206]–[208]. Table. 4.1 summarizes these results along with the system presented in this work.

High-speed (higher than the repetition rate of the final laser amplifier, if necessary) data collection and processing are essential to compensate for short-term (shot-to-shot) fluctuations. Sub-terawatt lasers operating at kHz repetition rate benefit from the compensation for beam-pointing instability by collecting, processing, and controlling at the laser amplifier's repetition rate [197]. However, higher power laser systems of interest in this work operate at much lower repetition rates ranging from 1 shot per minute (1/60 Hz) to 10 Hz [195], [196]. To circumvent inadequate data collection rates

necessary for control, the beam-pointing stabilization is performed by analyzing the pointing of pulses from the regenerative amplifier or oscillator pulse train before the final amplifier [195], [196]. It has been demonstrated that the pointing of the higher-repetition-rate regenerative amplifier beam has a strong correlation with respect to that of the lower-repetition-rate beam from the final amplifier and is thus suitable for compensating the pointing of the laser [195].

In various applications that do not require high-speed (shot-to-shot) stabilization, compensation for long-term pointing instabilities is of more interest than that for short-term variations. For example, an actively controlled laser pointing system [201] developed at Oak Ridge National Laboratory (ORNL) operates at 10 Hz and provides stabilization after 65-m of transport to convert a H^- beam into protons with 99% efficiency. Using two close-loop piezo-actuated mirrors, the standard deviation of the corresponding beam-pointing was reduced by $\sim 2\times$. Similarly, the Spallation Neutron Source at ORNL relies on active beam-position stabilization to improve ion beam profile diagnostic over a long distance (225 m) through correction of a multi-MW laser operating at 30 Hz [203]. An active stabilization system was implemented to mitigate long-term pointing instability induced by thermal drift in a high-power KrF laser [202]. Thermal drift is also identified as a main source that deteriorates the long-term stability of our system and will be discussed in this work.

Advanced computational methods that employ neural networks or machine learning offer effective solutions to problems encountered in active beam-pointing controls [206]–[208]. By performing time-series analysis and computer simulations on experimentally measured data sets using low-pass filters and neural networks, researchers at the University of Texas explored the maximum possible reductions in pointing instability of the laser, which drives LWFA experiments at 20 Hz. The feedforward algorithm reduces

the standard deviation of beam-pointing from 0.7 µrad to 0.3 µrad [206]. An additional challenge in the modeling and controlling of the piezo-actuated mirrors is hysteresis. To address hysteresis in piezo-actuated mirrors, a feedforward model learning algorithm based on least squares support vector machines has been developed. By compensating for nonlinearities during the controlling of the mirrors, this work offered regulation on four degrees of freedom of the beam and aided the development of an active pointing control system with two piezo-actuated mirrors [208]. A recurrent neural network has been developed to classify different types of disturbances that lead to beam-pointing instability, such as airflow, mechanical vibrations, and elastic deformation, in real-time and compensates for the given disturbance in the most effective manner [207].

In this work, a proof-of-principle study of active controlling a 16-inch mirror assembly by sampling a Continuous-wave (CW) laser diode output at 100 Hz was presented, which effectively resembles the regenerative amplifier operating at the same repetition rate. Actuating such a large optic is critical due to the necessity for independent control of the 12-inch beam-pointing after the final amplifier for the colliding experiment discussed above. A simple Field-programmable Gate Array (FPGA)-based proportional feedback control was implemented and reductions of the standard deviation of beam-pointing were observed in the horizontal and vertical directions by 91% and 78%, respectively. This study lays the groundwork for novel experiments requiring precise laser beam-pointing control. The principles of this study can be easily adopted by other facilities to improve beam-pointing stability. To the best of our knowledge, this work features the largest actively controlled optic used in a high-power laser system. Note that the next largest actively controlled mirror was only 4 inches in diameter [196]. As high-power laser systems continue to advance, this work will be meaningful to researchers interested in the frequency response and active control of large optics used in high-power

laser systems.

Table 4.1: Comparison of relevant parameters for actively controlled high-power laser systems. Corr.: correction. RR: repetition rate. M1: mirror 1. M2: mirror 2. H: horizontal direction. V: vertical direction.

Ref.	Peak Power	Diameter of Beam on Piezo Mirror (mm)	Size of Piezo Mirror (inch)	Corr. RR	Deviation Before Corr. (µrad)	Deviation After Corr. (µrad)
ZEUS (this work)	3 PW @ 1/60 Hz	305	16	100 Hz	0.83 (H) 1.14 (V)	0.075 (H) 0.25 (V)
Lund Laser Center [196]	40 TW @ 10 Hz	M1: n/a M2: 50	M1: 1 M2: 4	80 MHz	3.7	2.6
BELLA [195]	∼70 TW @ 1 Hz	81	n/a	1 kHz	170 (H) 220 (V)	10 (H) 26 (V)
Tokai University [197]	0.2 TW @ 1 kHz	n/a	2	1 kHz	30 µm (H) 42 µm (V)	1.0 µm (H) 1.1 µm (V)
ORNL [201]	2 MW @ 10 Hz	n/a	M1: 2 M2: 2	10 Hz	758 (H) 535 (V)	247 (H) 299 (V)
University of Szeged [202]	100 GW @ 1 Hz	35	n/a	1 Hz	19	14
SGII-UP-Petawatt [198]	500 TW @ n/a	n/a	1	1 kHz	2.8	0.63
ORNL [203]	214 MW @ 30 Hz	∼25.4	2	30 Hz	200	4.2
JAERI-APRC [204]	10 TW @ 10 Hz	50	n/a	2 Hz	70 (H) 20 (V)	10 (H) 10 (V)

4.2 Experimental Setup

The mirrors presented in this work have a diameter of 16 inches and a thickness of 2 inches. They have a broadband high-reflective coating on their front surfaces with a designed incident angle of 22.5°. Up to 120-J, 1-ns amplified pulses would be reflected into the 3-PW compressor by the 16-inch mirrors. A total of two 16-inch mirror as-

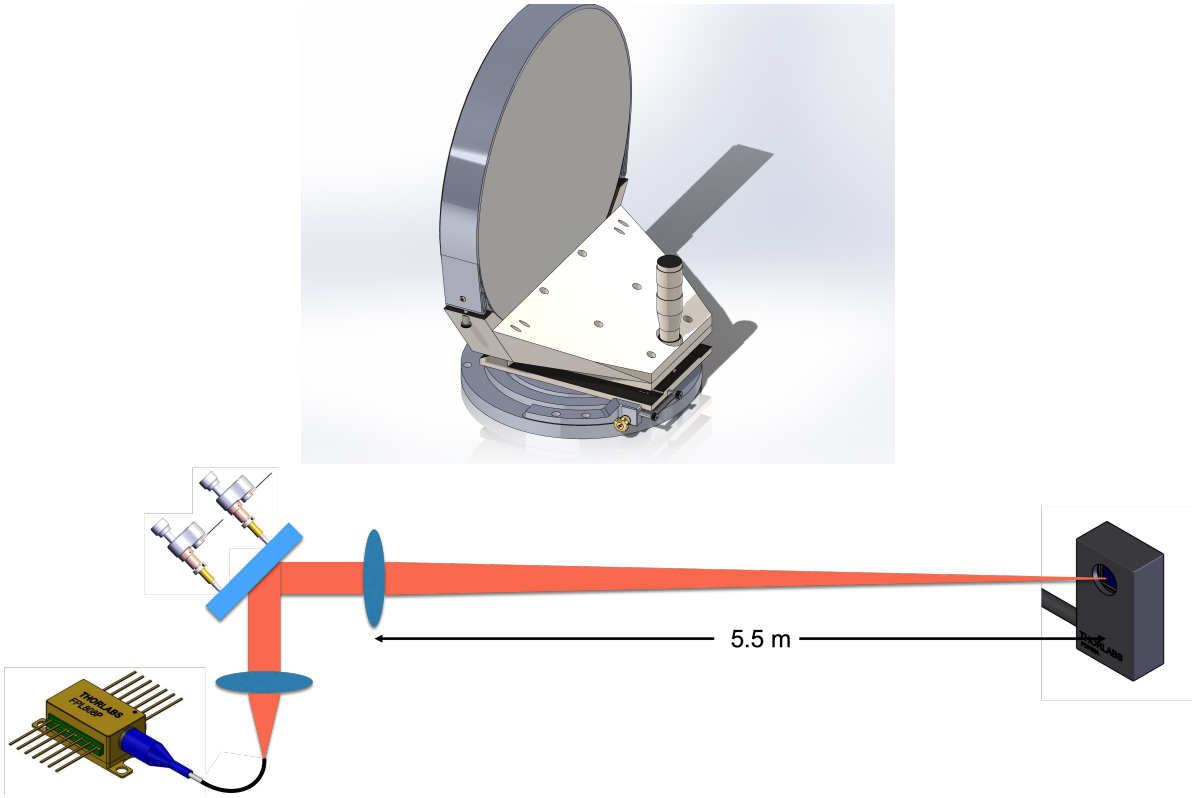

Figure 4.1: Experimental setup. Up: Computer-aided design (CAD) model of the 16-inch mirror assembly. Down: Schematic of the proof-of-principle experiment using a laser diode and position sensing detector.

semblies were constructed in order to redirect the beam by 90°. The original design of the 16-inch assembly was based on an off-the-shelf rotation stage and tilt platform. It also consists of a customized stainless steel V-block, reinforcing block, and strap to rigidly mount the optics, as shown in Figure 4.1. The total assembly weighs ∼50 kg. A replica with piezo-actuators was also constructed to demonstrate active control of beam pointing. Figure 4.1 inset shows an enlarged view of the piezo-actuated 16-inch mirror assembly. The two piezo-actuators were carefully aligned and centered with the micrometers to avoid excessive tensile stresses that lead to their failure. The positions of the piezo-actuators were then fixed with high-temperature epoxy.

To study the effects of the ambient environment on the beam-pointing stability, apparatuses to characterize vibration and temperature were also employed. Two three-dimensional seismic accelerometers simultaneously measured the vibration on the floor and the optical table. The accelerometer has a resolution of 0.05 mg with a frequency range (±5%) covering 0.5 to 3000 Hz. A temperature logger with 0.024°C resolution was placed on the optical table adjacent to the 16-inch mirror assembly to record the temperature every minute.

While waiting for the Ti:sapphire laser beam delivery, a proof-of-principle study of active beam-pointing control using a CW laser diode at 808 nm was performed. By sampling the CW beam only at 100 Hz, the operation of the active control system with the Ti:sapphire regenerative amplifier outputs at 100 Hz can be effectively simulated. The single-mode, polarization-maintained CW fiber output was first collimated to a 3-inch diameter beam. The collimation and beam profile were examined with a wavefront sensor. The collimated 3-inch beam was then incident on the top portion of the 16-inch mirror assembly at 22.5°, and the reflected beam was focused with a lens with a 5.5-m focal length. A two-dimensional, lateral effect position sensing detector was placed at

focus to measure the position of the beam's centroid. The detector has a bandwidth of 15 kHz and is capable of resolving 0.75-µm displacement. The laser diode, focusing lens, and position sensing detector was rigidly mounted on the chain of optical tables hosting the ZEUS laser system. The beam-pointing instability induced by these three elements is negligible compared to that induced by the 16-inch mirror.

A simple proportional feedback loop was realized in the onboard FPGA of a real-time embedded controller (CompactRio, National Instruments), which acquires the position sensing detector outputs as the feedback loop's inputs and produces the corrected voltage to drive the piezo-actuator. The voltage outputs generated from the position sensing detector were digitized by a 24-bit Delta-Sigma Analog-to-digital Converter (ADC), and the corrected voltages calculated by the FPGA were transmitted to a 16-bit string Digital-to-analog Converter (DAC). The piezo controller amplifies the corrected voltages 15 times and then directly applies the amplified voltage to the piezo-actuators.

4.3 Results and Discussion

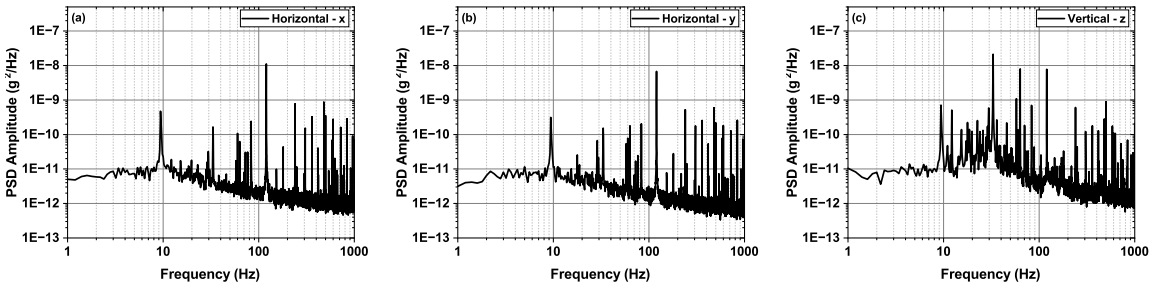

Figure 4.2: Vibration baseline measured on the floor near 3-PW compressor in the ZEUS facility. PSD: power spectral density. (a) Horizontal direction perpendicular to main laser chain. (b) Horizontal direction parallel to main laser chain. (c) Vertical direction.

The ambient vibration on the floor and optical table with the beam-pointing stability

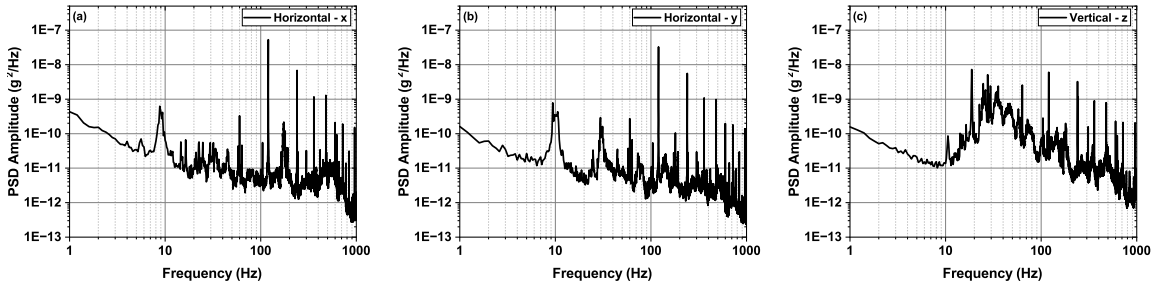

Figure 4.3: Vibration baseline measured on the optical table of the main laser chain in the ZEUS facility. PSD: power spectral density. (a) Horizontal direction perpendicular to main laser chain. (b) Horizontal direction parallel to main laser chain. (c) Vertical direction.

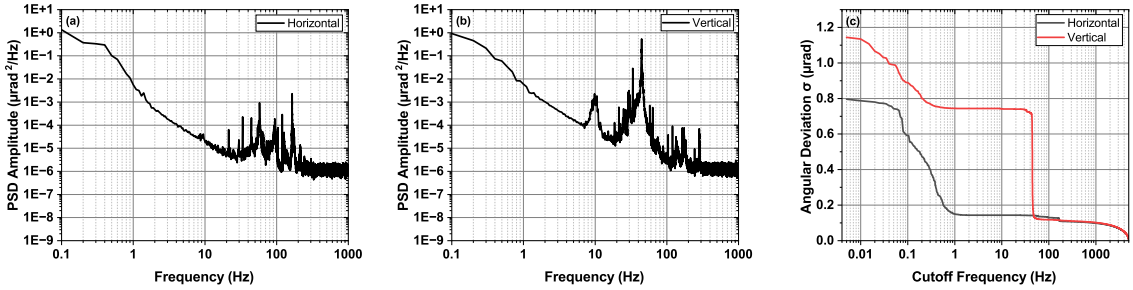

Figure 4.4: Short-term characterization of the original 16-inch mirror assembly. PSD: power spectral density. (a) Power spectral density of horizontal angular deviation. (b) Power spectral density of vertical angular deviation. (c) Comparison of the standard deviation of horizontal (black) and vertical (red) angular fluctuations, with only frequencies higher than the cutoff frequency contributing to the standard deviation.

measurement were simultaneously characterized using three-dimension accelerometers. The Power Spectral Density (PSD) of the measured time series is shown in Figure 4.2 and 4.3. The PSD $S(f)$ of a discrete time-series x_n is defined as:

$$S(f) = \frac{\Delta t}{N} \left| \sum_{n=0}^{N-1} x_n \exp\left(-\mathrm{i}2\pi f n \Delta t\right) \right|^2 , \tag{4.1}$$

where Δt is the sampling interval, N is the total number of samples. The baseline of the ambient vibration on the floor is determined to be 1×10^{-12} g^2/Hz, which is around two orders of magnitude larger than that reported in the ELI-Beamlines [209]. The maximum value also exceeds the 1×10^{-10} g^2/Hz limit specified by National Ignition Facility (NIF) [210]. The standard deviations of the ambient vibration on the floor in the x, y, and z directions are 0.241 mg, 0.165 mg, and 0.210 mg, respectively. Whereas the values are increased to 0.277 mg, 0.183 mg, and 0.302 mg on the optical table. As shown in Figure 4.3, in the horizontal directions x (perpendicular to the main laser chain) and y (parallel to the main laser chain), frequencies below 2 Hz, at 9 Hz and 60 Hz dominants the PSD below 100 Hz. Attention was aimed at frequency components lower than 100 Hz due to the $1/f^2$ scaling law for displacement regarding the frequency. Other laser facilities have also identified a cutoff frequency lower than 100 Hz (See, for example, Reference [195], [198]). The 30 Hz component in the y-direction also contributes significantly. In the z-direction (vertical to the table surface), a broader frequencies range between 14 and 83 Hz has a significant contribution in addition to the frequencies below 2 Hz. The above-mentioned considerable ambient vibration demonstrates the necessity for a system to actively compensate for the beam-pointing instability induced by ambient vibration.

The use of a CW laser in this proof-of-principle study provides us with a more com-

prehensive picture of beam-pointing instability induced by the 16-inch mirror in the frequency domain. In Figure 4.4(a) and (b), the PSD of the angular deviation sampled at 10 kHz were shown in the horizontal and vertical direction, respectively. Frequencies below 1 Hz dominate both the horizontal and vertical angular deviation. In addition, 33.5 Hz and 44.5 Hz components contribute significantly to the vertical angular deviation. The ∼10 Hz vibrational components on the optical table transferred to the angular deviation in both directions were also observed. However, their effects are negligible compared to the frequency components mentioned above. Figure 4.4(c) clearly illustrates the significance of each frequency component regarding their contribution to the overall standard deviation of angular deviation. The standard deviations of angular deviation at different cutoff frequencies are calculated by:

$$\sigma(f_{cutoff}) = \sqrt{\sum_{f_{cutoff}}^{f_{Nyquist}} 2S(f)\Delta f} \ , \tag{4.2}$$

where σ is the standard deviation, f_{cutoff} is the cutoff frequency, $f_{Nyquist}$ is the Nyquist frequency, $S(f)$ is the PSD as defined in Equ. 4.1, and $\Delta f = 1/\left(N\Delta t\right)$ is the frequency interval.

The cutoff frequencies of the original 16-inch mirror are determined to be 1 Hz and 50 Hz for the horizontal and vertical directions, respectively. The frequency components below the cutoff frequencies contribute to 81% of the total horizontal deviation of 0.796 µrad and 89% of the total vertical deviation of 1.14 µrad.

Figure 4.5 shows the step response of the piezo-actuated 16-inch mirror characterized by a 2.5-GHz oscilloscope. The square wave generated by a function generator was amplified by the piezo controller with a 20-µs rising edge and then drove the piezo-actuators.

The piezo-actuated 16-inch mirror reached a steady state in the horizontal direction within ∼150 ms. In the vertical direction, the mirror resonates for ∼700 ms with a ∼23 ms period, corresponding to the major peak at 44.5 Hz shown in Figure 4.4(b). The 44.5 Hz resonance frequency limits the maximum frequency of beam-pointing instability that could be compensated.

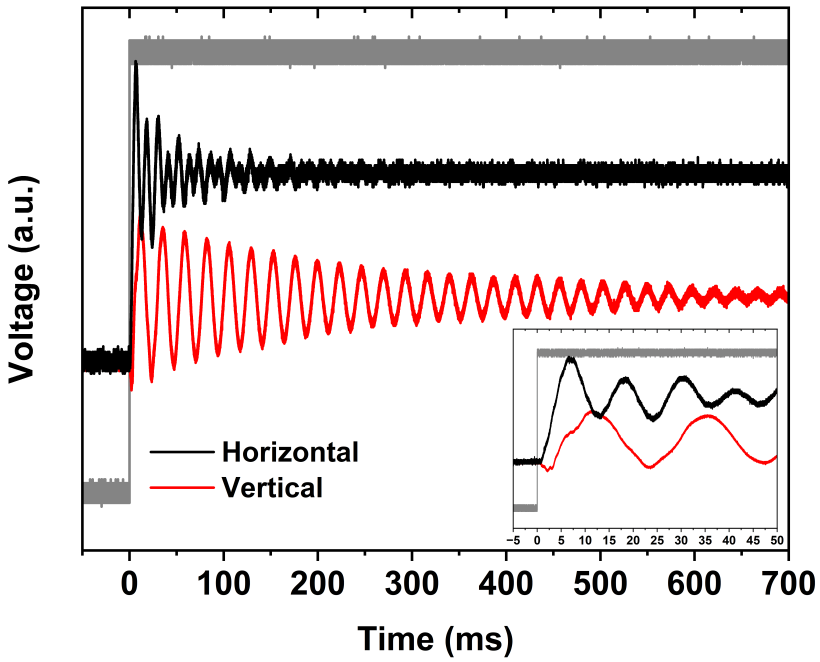

Figure 4.5: Step Response of the piezo-actuated 16-inch mirror in the horizontal (black) and vertical (red) direction. Inset: enlarged view of the first 50 ms.

The results of active beam-pointing control with proportional feedback control are shown in Figure 4.6. In Figure 4.6(a), the driving voltages were kept constant when no control was implemented. The proportional feedback control was realized at 100 Hz by sampling the position sensing detector and driving the piezo-actuators at such frequency, which is the repetition rate of the regenerative amplifier of ZEUS. When active control was implemented, the n-th sampled beam-pointing deviation was corrected by the (n-

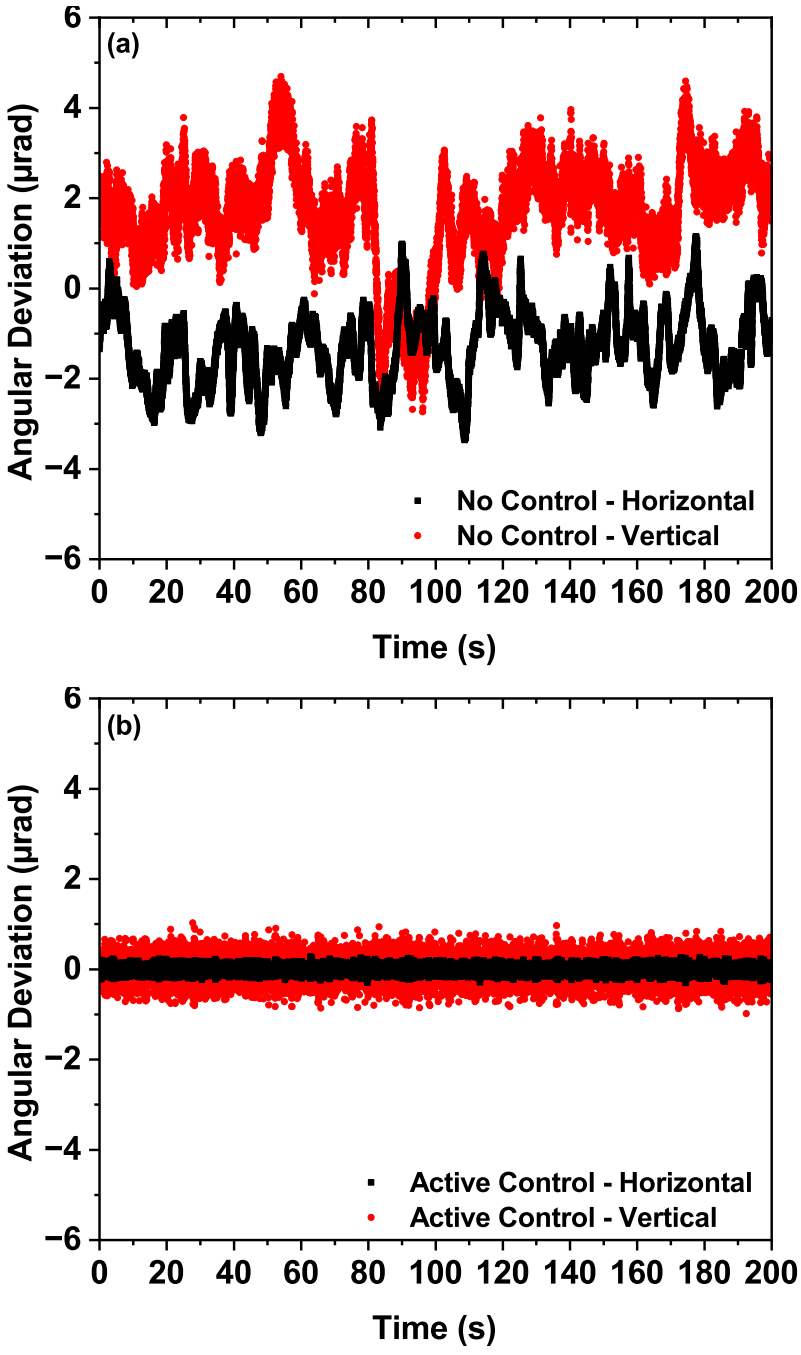

Figure 4.6: Short-term time series of the beam-pointing in the horizontal (black) and vertical (red) direction. (a) Piezo-actuated 16-inch mirror without active control. (b) Piezo-actuated 16-inch mirror with active control.

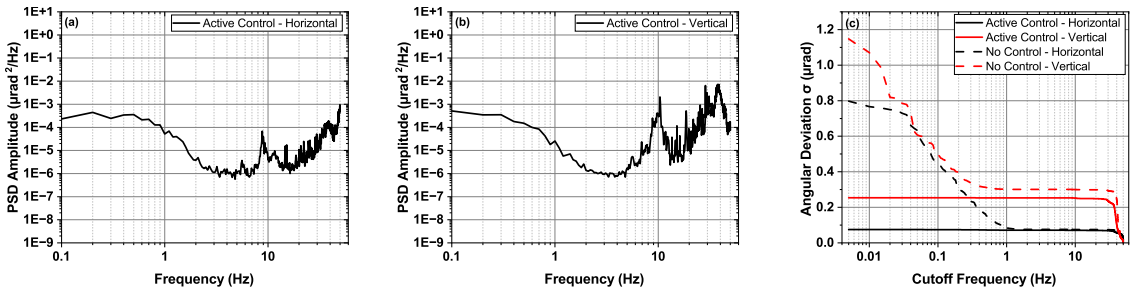

Figure 4.7: Short-term characterization of the piezo-actuated 16-inch mirror assembly. PSD: power spectral density. (a) Power spectral density of horizontal angular deviation. (b) Power spectral density of vertical angular deviation. (c) Comparison of the standard deviation of horizontal (black) and vertical (red) angular fluctuations, with only frequencies higher than the cutoff frequency contributing to the standard deviation.

1)-th sample 10 ms earlier. The feedback loop then acquired the deviation of the n-th sample to generate corrected voltage for the (n+1)-th sample. Benefiting from the FPGA architecture, the loop time was determined to be less than 50 µs without any FPGA optimizations, much less than the sampling interval of 10 ms. The loop time consists of 8.5 µs ADC input delay, 5.3 µs DAC update time, and 20 µs controller delay during voltage amplification. The standard deviations of the horizontal and vertical angular deviations are 0.798 µrad and 1.15 µrad when piezo-actuators are driven at a constant voltage (no active control), consistent with the performance of the original 16-inch mirror. This indicates that incorporating the two piezo-actuators does not deteriorate the mechanical properties of the original 16-mirror assembly design, and the electrical noise of the ADC, DAC, and piezo controller is negligible. With proportional feedback control, a 91% reduction to 0.0747 µrad in the horizontal direction and a 78% reduction to 0.254 µrad in the vertical direction were demonstrated, as shown in Figure 4.6(b).

To further study the efficacy of the proportional feedback control, the PSD and cutoff

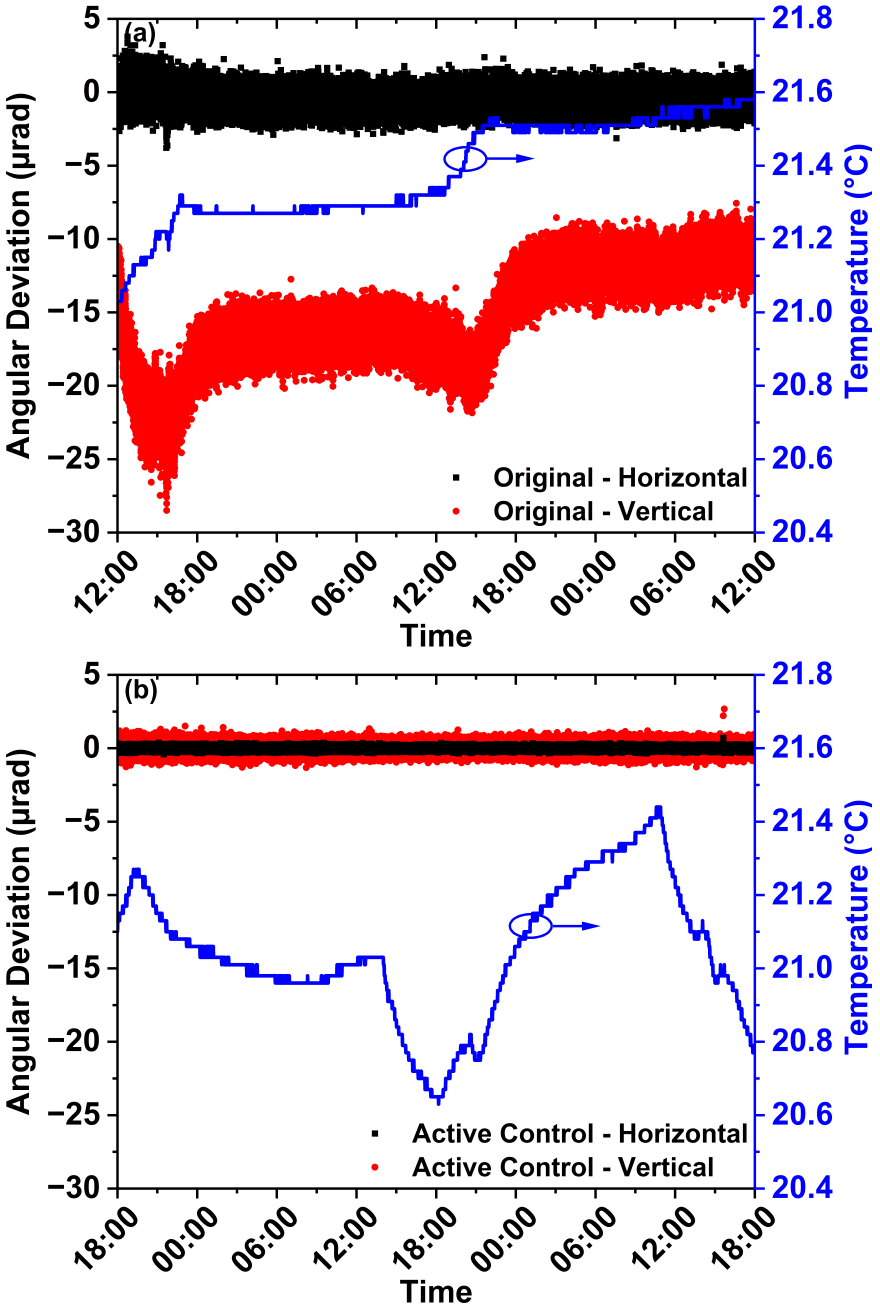

Figure 4.8: Long-term (48 hours) stability characterization of two 16-inch mirror assemblies in the horizontal (black) and vertical (red) direction. The temperature fluctuation is plotted as the blue curve. (a) Original 16-inch mirror design. (b) Actively controlled piezo-actuated 16-inch mirror assembly.

frequency of the time series (Figure 4.6(b)) of the actively controlled 16-mirror were investigated. The results are shown in Figure 4.7. With the proportional feedback control, Figure 4.7(a) illustrates three orders of magnitude depression across all frequencies in the horizontal direction. Figure 4.7(b) illustrates three orders of magnitude depression for lower frequencies and two orders of magnitude depression near its resonance frequency in the vertical direction. Figure 4.7(c) further demonstrates the efficacy of the active control method by comparing the cutoff frequency-dependent angular deviation with and without proportional feedback control. In the vertical direction, compensating all the frequency components up to the mirror's resonance frequency at 44.5 Hz was realized. All the frequency components lower than the Nyquist frequency were compensated in the horizontal direction. It is believed that the small residual in the horizontal direction was due to the convolution of the vertical direction since the laser incident the mirror at 22.5°.

Managing long-term beam-pointing jitter induced by ambient environmental change is also required for high-power laser systems since the beam-pointing jitter can significantly deteriorate the experimental results after the initial alignment. As a result, the beam-pointing jitter of the original 16-inch mirror over 48 hours (Figure 4.8(a)) was first studied. The beam-pointing was sampled at 100 Hz; nonetheless, only one point per second was shown for clarity in Figure 4.8. A considerable deviation in the vertical direction up to 23 µrad and a 7.6 µrad change in the horizontal direction with only 0.6°C temperature variation was observed. It is believed that such deviation is due to the differences between the thermal expansion coefficient of the different stainless steel components, which is the material of both our customized and off-the-shelf components. The original 16-inch mirror assembly experienced relaxation and re-equilibrium during the temperature increment. The long-term beam-pointing jitter was completely elim-

inated with the same proportional feedback control operating at 100 Hz, as shown in Figure 4.8(b). With a larger temperature variation of 0.8°C and more random fluctuation, the standard deviation of the horizontal and vertical beam-pointing jitter is reduced to 0.085 µrad and 0.29 µrad, respectively. The long-term stabilization results further demonstrate the robustness of our control method.

4.4 Conclusion and Outlook

In conclusion, to the best of our knowledge, an actively controlled mirror with a diameter of 16 inches used in a high-power laser system was first demonstrated in a proof-of-principle study. Actively controlling the beam-pointing with large optics is of vital importance for a wide range of experiments facilitated with a high-power laser system such as ZEUS. With two piezo-actuators and a simple FPGA-based proportional feedback control, the short-term beam-pointing instability was reduced by up to an order of magnitude. The long-term drift due to temperature variation was also eliminated. Given the considerable baseline of ambient vibration in the ZEUS reported, our approach manifests its effectiveness, although limited by the resonance frequency of the construction.

Future work would be beneficial to fine-tune the resonance frequency of the 16-inch mirror assembly to a frequency higher than the Nyquist frequency of the active control system, assisted by finite element analysis. With such a design modification, our proportional feedback control could potentially compensate for beam-pointing instabilities up to the Nyquist frequency, which is 50 Hz in the scheme described in this work. Data-driven Recurrent Neural Network models such as Long Short-Term Memory and Grated Recurrent Unit could also be employed to improve the efficacy of the feedback

control [207]. However, a substantial amount of data from the actual laser shots must be collected to train the model.

Chapter 5

Summary and Future Work

5.1 Summary

To summarize, this dissertation has accomplished the theoretical and experimental study of few-cycle, CEP-stabilized, ultra-intense LWIR pulses generation in the following three aspects:

1. LWIR seed pulses were generated through DFG in the ZGP and AGS crystals. For the first time, milliwatt-level LWIR seed pulses were produced by mixing 2.9-μm Er:ZBLAN fiber amplifier/compressor outputs with their frequency-shifted replicas in a ZGP crystal. LWIR pulses centered at 11 μm with an average power of 1.25 mW were generated and have a near-Gaussian profile. The generated LWIR spectrum has an FWHM bandwidth of ∼1.3 μm, compatible with three-cycle transform-limited pulses. Wavelength tunability was demonstrated by adjusting the input power of the InF_3 fiber, thus changing the wavelength of the SSFS output and that of the idler in DFG. Higher pulse energy (110 nJ) and ultra-broadband spectral bandwidth (supporting two-cycle pulses production) were achieved at a

lower repetition rate in an AGS crystal driven by two-color Ti:sapphire laser output and assisted by GA optimization. A single-shot infrared spectroscopy study on ammonia was performed with the LWIR seed source operating at 480 Hz.

2. Parametric amplification of LWIR seed pulses was realized through noncollinear OPA in a 5-mm thick GaSe crystal, pumped by nanosecond 2.7-μm pulses at 10 Hz. As a consequence of crystal properties related to LIDT and the beam-pointing fluctuation, the attained parametric gain was limited to $\sim 2\times$. An autocorrelator based on TPA in an InSb crystal was constructed to enable the characterization of ultrashort pulse duration. A discussion of spectral phase retrieval via the Cross-correlation Frequency-resolved Optical Gating (XFROG) technique was presented.

3. For the first time, an actively pointing-controlled mirror with a diameter of 16 inches used in a high-power laser system was demonstrated in a proof-of-principle study. Using a proportional feedback loop and piezo-actuated mirror, the short-term beam-pointing fluctuation induced by ambient vibration was significantly reduced by 91% to 0.075 μrad in the horizontal direction and by 78% to 0.25 μrad in the vertical direction. Long-term fluctuation due to temperature drift was also eliminated.

5.2 Future Work

1. Conversion efficiency in the Er:ZBLAN fiber laser-driven LWIR seed source was limited by the timing instability between the ∼4 μm signal and the ∼2.9 μm pump pulses due to the long length of the InF_3 fiber. Our analysis indicates that this instability could be sufficiently reduced by (i) increasing energies into the SSFS

fiber, and thus shortening the required fiber length, leading to reduced timing instability [152], and (ii) using active feedback such as the modified version of active beam-pointing control system developed in Chapter 4 for controlling the free-space delay to actively compensate this timing instability [84]. With these improvements, nJ-level LWIR ultrashort pulses with tens of milliwatt average power is expected.

2. The GA-assisted spectral bandwidth optimization would be more efficient and effective by employing the GA *in situ* with real-time fitness feedback from diagnostics, for instance, spectral bandwidth measured by a spectrometer. However, in such a scheme, more constraints are needed to avoid potential damage in the Ti:sapphire CPA system that can occur due to inadvertent bandwidth narrowing.

3. A second mercury-cadmium-telluride detector could be added to the Autocorrelation (AC) setup for single-shot calibration in order to correct for input pulse energy fluctuation. On the other hand, a significant amount of effort is necessary to improve the shot-to-shot energy fluctuation of the pump laser.

4. The limited parametric gain achieved in the LWIR OPCPA induced by the properties of the GaSe crystal could be alleviated with multi-stage pumping and amplification [78] and pumping with shorter (picosecond [78] or sub-picosecond [211], [212]) pulses generated from Er:ZBLAN fiber amplifier and nonlinear compressor, in addition to the advances in crystal manufacturing. The active beam-pointing control system depicted in Chapter 4 could be easily modified and implemented in the LWIR OPCPA such that the spatial jitter between pump, LWIR seed and the GaSe crystal could be minimized.

5. The resonance frequency of the 16-inch mirror assembly could be fine-tuned to

a frequency higher than the Nyquist frequency of the active control system, assisted by finite element analysis. With such design modification, our proportional feedback control could potentially compensate for the beam-pointing instability up to the Nyquist frequency, which is 50 Hz in the scheme described in this work. Data-driven Recurrent Neural Network models such as Long Short-Term Memory and Grated Recurrent Unit could also be employed to improve the efficacy of the feedback control [207]. However, a substantial amount of data from the actual laser shots must be collected to train the model.

Appendix A

Application, Characterization, and Parametric Amplification of Long-wave Infrared Pulses

A.1 Molecular Spectroscopy with Long-wave Infrared and Mid-infrared Pulses

Molecular spectroscopy has been a workhorse in the analytical chemistry field to identify or quantify a species, which depends on the interactions between molecules and electro-

This Appendix is partially based on the previously published articles:

X. Xiao, J. Nees, **H. Huang**, and I. Jovanovic, "Nanosecond 2.73-µm parametric source for pumping LWIR OPCPA," in *CLEO: QELS_Fundamental Science*, Optical Society of America, 2021, JTu3A–109. [213]

I. Jovanovic, X. Xiao, and **H. Huang**, "Production of high-power ultrashort pulses in the long-wave infrared range," in *2020 IEEE Photonics Conference (IPC)*, IEEE, 2020, pp. 1–2. [214]

X. Xiao, J. Nees, **H. Huang**, A. Galvanauskas, and I. Jovanovic, "Optical parametric amplification at 10.6 µm in GaSe pumped by a 2.75-µm parametric source," in *CLEO: Applications and Technology*, Optical Society of America, 2020, JTu2F–19. [215]

magnetic radiation. LWIR and mid-IR sources are of particular interest in such a field since they can access the molecular "fingerprint" region. Most spectroscopic systems can be categorized into two types: scanning system and broadband system, employing a wavelength-tunable narrow-band source and a broadband source, respectively.

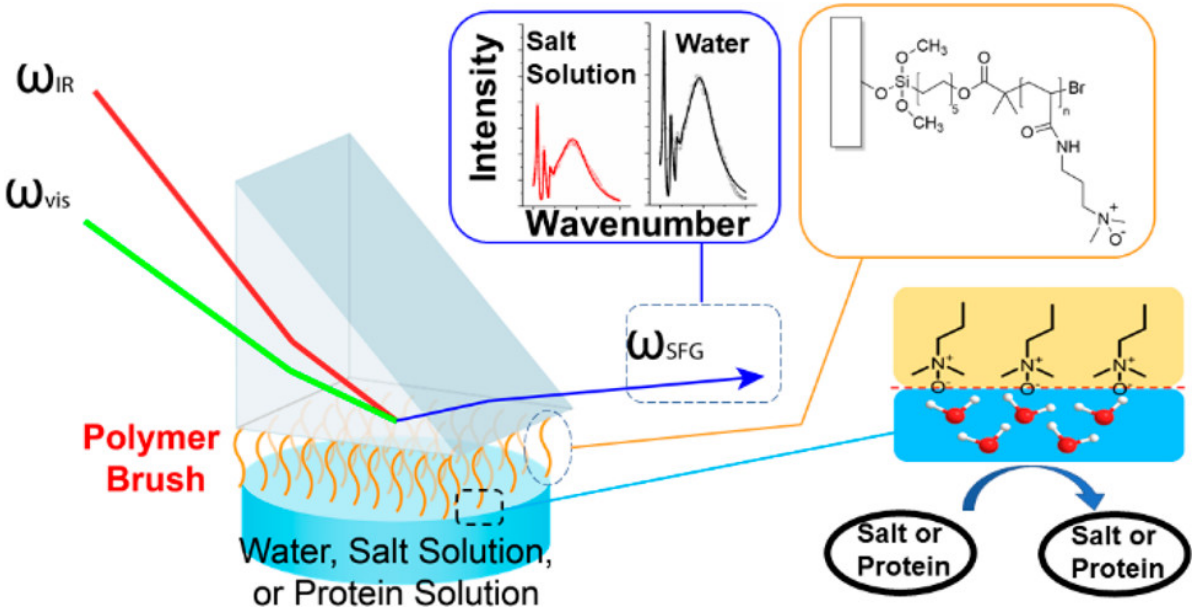

Figure A.1: Schematic and spectra of sum-frequency generation vibrational spectroscopy. Reprinted with permission from [216]. Copyright 2021 American Chemical Society.

A commercial wavelength-tunable narrow-band infrared source (EKSPLA) was employed for Sum-frequency Generation (SFG) vibrational spectroscopy studies. SFG vibrational spectroscopy is a surface-sensitive nonlinear spectroscopy technique, which has been developed into a powerful tool to study surfaces of functional materials such as antifouling polymer coatings [216]–[219] and graphene [220]. In the SFG spectroscopic system, an Nd:YAG laser-pumped OPG/OPA generates ~20 ps pump and signal beam at 50 Hz for DFG in a nonlinear crystal. The wavelength of the narrow band (~5 cm^{-1}) LWIR or mid-IR idler can be tuned by adjusting the OPG/OPA output wavelength

and phase-matching angle of DFG simultaneously. A visible beam at 532 nm is also generated via Second-harmonic Generation (SHG) of the 1064 nm pump, which up-converts the infrared signal into the visible region such that it can be easily detected by a monochromator and Si-based detector. The sampling rate of such a system is significantly limited due to the wavelength-tuning mechanism. A typical scan from 2800 to 3600 cm^{-1} (2.8–3.6 µm) that comprises C-H and O-H bands requires a few minutes to complete.

The schematic and spectra of SFG vibrational spectroscopy are shown in Figure A.1. In order to generate SFG spectrum, a pump laser at 532 nm and a wavelength-tunable narrow band infrared probe were used as input beams and overlapped spatially and temporally at the polymer surface or polymer/aqueous solution interface. SFG signal can only be generated from a surface or interface due to the selection rule of the SFG technique under the electric dipole approximation. The selection rule determines that only the regions where inversion symmetry is broken, i.e., at the surface or interface, can contribute SFG signals. The SFG signal can be enhanced at specific input infrared frequencies, which are associated with vibrational transitions of the sample molecules on the surface/at the interface. As a result, characterization of the molecular structure at the surface or interface *in situ* and in real-time with SFG spectroscopy can be realized.

A broadband spectroscopic system is preferred for practical applications, especially when a time-resolved measurement is desired. In such a spectroscopic system, a broadband infrared source outputs a spectrum that covers the entire region of interest. As a result, the scanning mechanism is eliminated, and the sampling rate is determined by the minimum between the repetition rate of the source and the sampling rate of the spectrometer. A sampling rate in the order of 1 kHz could be realized with a diode-pumped solid-state laser source and spectrometer based on pyroelectric arrays.

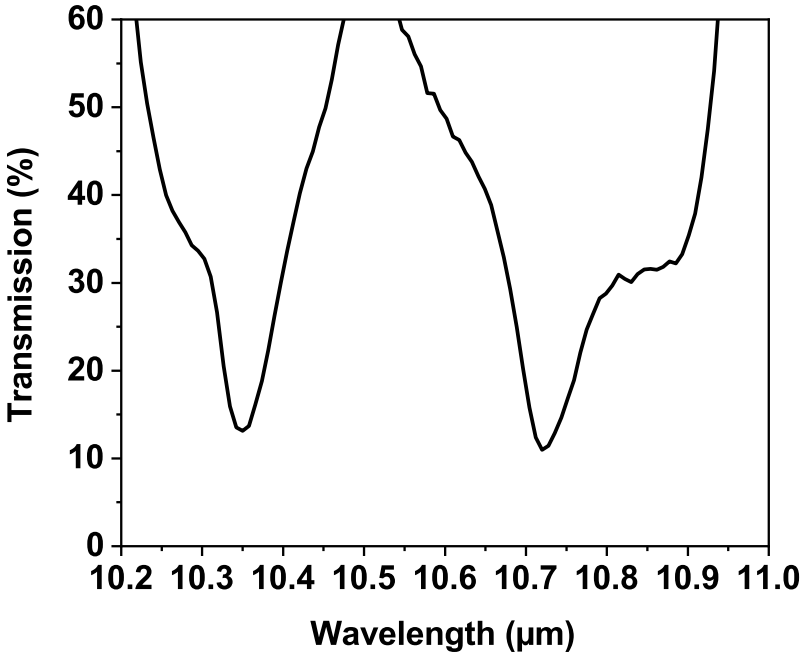

Figure A.2: Measured transmittance spectrum of ammonia.

Infrared spectroscopy theories, instrumentation, data collection, and data analysis has been extensively studied [221]; therefore, they will not be discussed in detail in this dissertation. In this experiment, the LWIR seed pulses described in Chapter 3 passed through a 12.7-cm cell containing ammonia gas at atmospheric pressure with polyethylene film-sealed ends. The spectrum of the transmitted LWIR seed pulse was measured with a homemade spectrometer described in Reference [222]. The ammonia gas was produced by evaporation of a 50% ammonium hydroxide solution. A control experiment utilizing the same apparatus but filled with air at atmospheric pressure was also performed. The spectrum was then subtracted from the ammonia transmittance spectrum to correct for air and polyethylene absorption. The background-subtracted ammonia transmittance spectrum was shown in Figure A.2, with two major features near 10.3 and 10.7 µm, qualitatively in good agreement with the results shown in Reference [151]. The observed shoulders in Figure A.2 are likely due to the excessive amount of water vapor in the sample.

A.2 Characterization of Ultrashort Long-wave Infrared Pulses

A.2.1 Autocorrelation

The characterization of ultrashort pulses has been a continued challenge for the ultrafast optics community since the pulse duration is much shorter than any electronics can respond. Intensity AC [69], [168], [223] and XFROG [224], [225], developed in the NIR region, have been successfully employed in LWIR. Extremely thin AGSe [69] and GaSe [223] crystals have been implemented to realize SHG AC. The AC function of the

intensity envelope of the test pulse measured by a square-law photodetector in a SHG configuration can be written as,

$$S(\tau) \propto \int |E_2(t,\tau)|^2 \, \mathrm{d}t \propto \int I(t) \, I(t-\tau) \, \mathrm{d}t \tag{A.1}$$

Achieving an even broader bandwidth with phase-matching nonlinear crystals becomes unpractical. A nearly wavelength-independent AC based on TPA in an InSb crystal was constructed since the TPA coefficient is nearly constant ($\approx$ 3 cm/MW) within the LWIR region [226]. Figure A.3 shows the experimental setup for TPA AC. A small portion of the input beam reflected by a ZnSe wedge serves as the probe arm and enters a delay line. The delay line consists of two mirrors and a translation stage where the movement of the two mirrors has a 0.5-µm increment. The majority of the input beam transmits through the wedged beamsplitter and serves as the pump beam for TPA. The probe and pump overlap within the InSb crystal and undergo self TPA and induced TPA. The remainder of the pump beam was blocked by the iris placed behind the TPA crystal such that the mercury-cadmium-telluride detector only measures the weak probe beam. The measured pulse energy of the probe beam is reduced due to the induced TPA when overlapping with the pump beam spatially and temporally.

The intensity-dependent absorption of the pump and probe beam can be expressed as,

$$\begin{aligned}
\frac{\partial I_{pump}(r,z;t)}{\partial z} &= -\alpha I_{pump}(r,z;t) - \beta I_{pump}^2(r,z;t) - \beta I_{pump}(r,z;t) \, I_{probe}(r,z;t+\delta t) \\
\frac{\partial I_{probe}(r,z;t)}{\partial z} &= -\alpha I_{probe}(r,z;t) - \beta I_{probe}^2(r,z;t) - \beta I_{pump}(r,z;t-\delta t) \, I_{probe}(r,z;t)
\end{aligned} \tag{A.2}$$

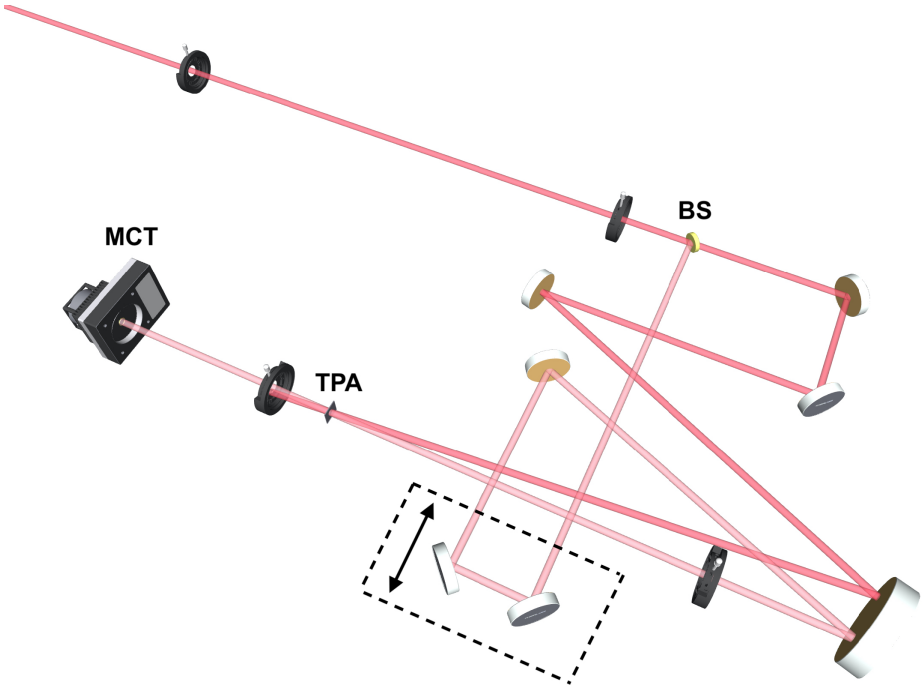

Figure A.3: Experimental setup for InSb-based TPA AC. BS: beamsplitter. MCT: mercury-cadmium-telluride detector. TPA: two-photon absorption crystal. Adapted from [222].

where I is the intensity of the beam, z is the propagation distance, α is the linear absorption coefficient, β is the TPA coefficient.

The solution of I_{probe} after propagating through distance L is:

$$I_{probe}(r,L;t) = \frac{(1-R)^2 I_{pump}(r,0;t-\delta t)\, I_{probe}(r,0;t)\exp(-\alpha L)}{1+f(t-\delta t)\exp\left(-r^2/w_{pump}^2\right)} \cdot \frac{1}{I_{pump}(r,0;t-\delta t) + I_{probe}(r,0;t)\ln\left[1+f(t-\delta t)\exp\left(-r^2/w_{pump}^2\right)\right]} \tag{A.3}$$

where

$$f(t-\delta t) = (1-R)\,\beta I_{pump}(r,0;t-\delta t)\cdot[1-\exp(-\alpha L)]\cdot\exp\left[-(t-\delta t)^2/\tau^2\right]/\alpha \tag{A.4}$$

The solution of I_{probe} can be further simplified as,

$$I_{probe}(r,L;t) \approx \frac{(1-R)^2 I_{probe}(r,0;t)\exp(-\alpha L)}{1+f(t-\delta t)\exp\left(-r^2/w_{pump}^2\right)} \tag{A.5}$$

The transmission of the probe beam after the TPA crystal can be written as,

$$T_{probe}(\delta t) \approx (1-R)^2\exp(-\alpha L)\cdot\sum_{k=0}^{\infty}\frac{(-1)^k p^k}{(k+1)^{3/2}}\exp\left[-\frac{k}{k+1}\left(\frac{\delta t}{\tau}\right)^2\right] \tag{A.6}$$

where $p = (1-R)\,\beta I_{pump}(r,0;t-\delta t)\cdot[1-\exp(-\alpha L)]/\alpha$.

When TPA depletion is small and therefore $p \ll 1$, the transmission of the probe can be written as,

$$T_{probe}(\delta t) \approx (1-R)^2\exp(-\alpha L)\left[1-\frac{p}{2\sqrt{2}}\exp\left(-\frac{\delta t^2}{2\tau^2}\right)\right] \tag{A.7}$$

As illustrated in the Equation above, the transmission of the probe beam as a function of the temporal delay between the pump and probe follows the same expression as the SHG AC of a Gaussian pulse. As a result, measuring the time-dependent intensity of the probe beam and deconvolving the AC trace with a deconvolution factor of 0.707 provide us the characterization of ultrashort LWIR pulse's duration.

A 0.5-mm thick InSb crystal was employed in the experiment (Figure A.3), which requires $\sim$0.4 MW/cm^2 pump intensity for a 5% induced TPA, much less than the available pump intensity. The experimental results of characterizing the 110-nJ ultrashort LWIR seed pulses described in Chapter 3 were hindered, likely due to the large shot-to-shot energy fluctuation (up to 10%) of the Ti:sapphire pump pulses, which in theory could be mitigated with statistical average. Extensive efforts are needed to stabilize the Ti:sapphire pump laser in order to realize a valid AC using the TPA-based apparatus. Additionally, A second mercury-cadmium-telluride detector could be added to the AC setup for single-shot calibration.

A proof-of-concept study of induced TPA was conducted with the same apparatus using CO_2 laser. The results verify the design of TPA-based AC qualitatively, thus will not be presented in detail in this dissertation.

A.2.2 Frequency-resolved Optical Gating

Intensity AC has nontrivial ambiguities. One may wonder if we could acquire more information about the optical pulses by combing their spectrum and AC measurements. In fact, the pulse's intensity AC is nothing but the inverse Fourier transform of the squared magnitude of its intensity's Fourier transform, which contains no phase information. Retrieving phase from either of these measurements can be categorized as a

one-dimensional phase retrieval problem, which is mathematically impossible. Instead, a two-dimensional measurement is needed to retrieve the phase information.

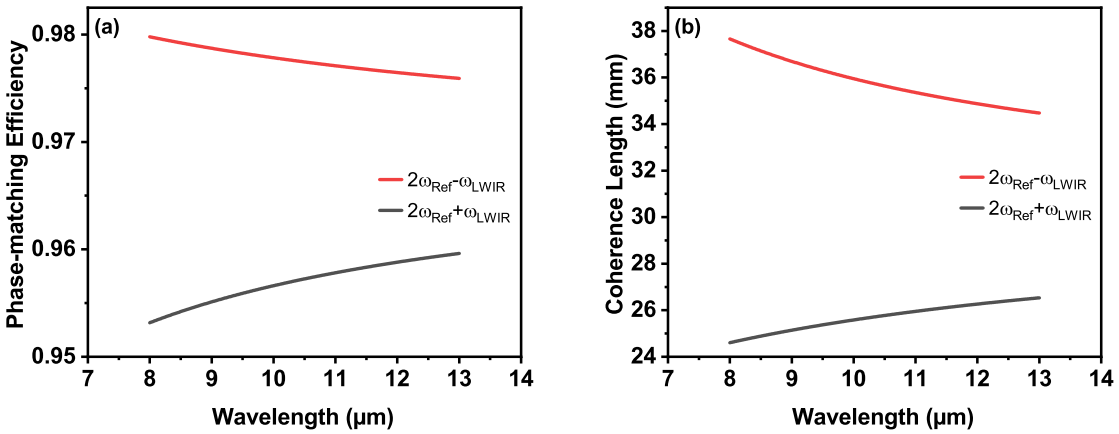

Figure A.4: Analytical study of characterizing the pulse duration and spectral phase of ultrashort LWIR pulses using Four-wave Mixing (FWM) XFROG in the atmosphere. (a) Phase-matching efficiency of FWM processes between 830-nm pump and broadband LWIR pulses in air. (b) Coherence length ($\pi/|\Delta k|$) of the FWM process.

The Frequency-resolved Optical Gating (FROG) technique, operating in the time-frequency domain, has been the workhorse in the field of ultrashort pulse characterization [227]. It utilizes a two-dimensional array of data, $I_{FROG}(\omega, \tau)$, acquired from a spectrally resolved nonlinear-optical gating process, and then retrieves the temporal intensity and phase of arbitrary pulses via various algorithms [228]–[230].

The measured two-dimensional "FROG trace" can be expressed as,

$$I_{FROG}(\omega, \tau) \propto \left| \int_{-\infty}^{\infty} E_{sig}(t, \tau) \exp(-\mathrm{i}\omega t)\, \mathrm{d}t \right|^2 \tag{A.8}$$

where E_{sig} is the generated FROG signal in a spectrally resolved nonlinear-optical gating process, where one ultrashort pulse gates another in the temporal or frequency domain.

In self-referenced versions of FROG, such as SHG FROG, $E_{sig}(t,\tau)$ is a function of the test pulse $E(t)$ and a variably delayed replica of it, $E(t-\tau)$. In XFROG scheme, another known gate pulse is used as a reference, and $E_{sig}(t,\tau)$ becomes a function of the reference pulse and the test pulse.

SHG FROG is less favored in the LWIR as a consequence of the limitation of nonlinear crystals for broadband phase-matching and the limitation of the detectors in the ∼5 µm mid-IR for fast and efficient measurement. To circumvent these limitations, XFROG based on FWM process is studied in this Section. Figure A.4 shows the analytical calculation of the FWM process in the atmosphere that generates the XFROG signal. The refractive-index models of the atmosphere were adopted from Reference [231] and [232] for visible and NIR and LWIR regions, respectively. The signal pulse at 830 nm in the DFG process described in Chapter 3 serves as the reference beam. The FWM photon (ω_{FWM}) can be generated via two different mixing processes: $\omega_{FWM} = 2\omega_{Ref} - \omega_{LWIR}$ (Figure A.4, red) or $\omega_{FWM} = 2\omega_{Ref} + \omega_{LWIR}$ (Figure A.4, black). The intensity of the generated FWM beam in such two processes can be expressed as $I_{FWM} \propto I_{Ref}^2 \cdot I_{LWIR}$, therefore a weak LWIR pulse can be efficiently detected via high-power pumping. Compared to $\omega_{FWM} = 2\omega_{Ref} + \omega_{LWIR}$ (Figure A.4, black) process, $\omega_{FWM} = 2\omega_{Ref} - \omega_{LWIR}$ (Figure A.4, red) offers a higher phase-matching efficiency (>97.5%) over the entire LWIR region. The calculated coherence length ($\pi/|\Delta k|$) of the later FWM process (Figure A.4, red) is greater than 34 mm in the LWIR, much longer than the 6-mm confocal parameter of the LWIR beam if loosely focused to ∼100 µm beam waist.

In summary, the broadband FWM process can be achieved through focusing synchronized 830-nm reference beam and LWIR beam in the atmosphere. The XFROG signal can be upconverted into the visible region such that fast and efficient detection is available using complementary metal–oxide–semiconductor (CMOS) sensor. The method

enables single-shot measurement and retrieval of ultrashort LWIR pulse duration and spectral phase, provided that a high-throughput phase-retrieval algorithm can be implemented.

A.3 Optical Parametric Chirped Pulse Amplification of Long-wave Infrared Pulses

A.3.1 Experimental Setup

The pump source of the OPCPA is based on the previously published article: X. Xiao, J. Nees, and I. Jovanovic, "High-energy nanosecond parametric source at 2.7 µm," *Applied Optics*, vol. 60, no. 13, pp. 3585–3590, 2021. [233]. The author realigned, characterized, and improved the performance of the nanosecond, mid-IR pump source in terms of its pulse energy and beam profile. The stretcher and compressor were designed, constructed, and discussed in detail in Reference [222]. The author realigned and improved the efficiency and output beam profile of the stretcher.

The schematic of the OPCPA system is shown in Figure A.5. The front-end of the system is based on DFG pumped by a custom-built Ti:sapphire CPA system capable of delivering up to 22 mJ, ∼40 fs pulses at 480 Hz. The ultra-broadband LWIR seed source is generated through DFG of two-color chirped output from the regenerative amplifier of the Ti:sapphire CPA system in a 0.4-mm thick, AR-coated AGS crystal in a collinear geometry. The LWIR seed is then extracted from the residual pump and signal using a long-pass filter. Since the pump and signal of the DFG originate from the same pulse in the Ti:sapphire oscillator, the LWIR seed architecture presents passive CEP stability. Up to 110-nJ LWIR pulse can be obtained to seed the OPCPA.

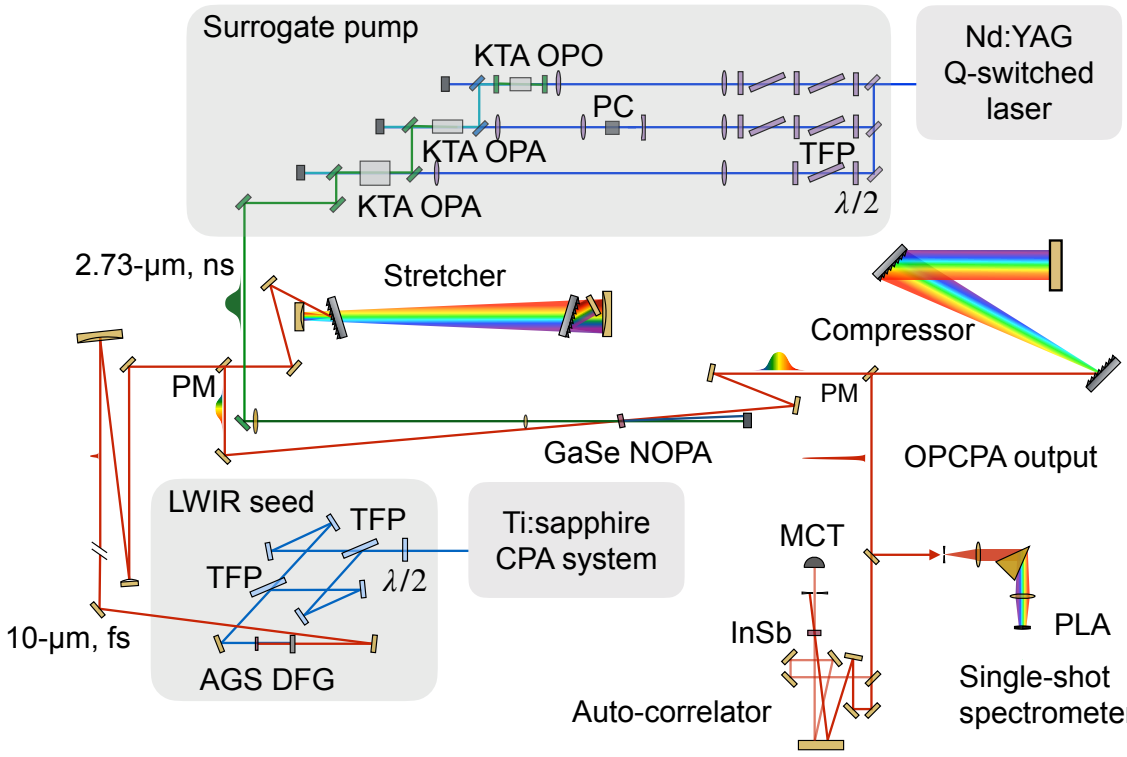

Figure A.5: Schematic of the GaSe OPCPA architecture. λ/2: half-wave plate; PLA: pyroelectric linear array; PC: Pockels cell; PM: pick-off mirror; TFP: thin-film polarizer [222].

A $KTiOAsO_4$ (KTA)-based OPO/OPA system was developed to provide nanosecond mid-IR pumping for the LWIR OPCPA. The mid-IR pump is driven by an injection-seeded, Q-switched Nd:YAG laser (Spectra-Physics, Quanta-ray PRO-250-10H), which delivers 10-ns, 1.064-µm pulses with an energy of up to 1.4 J at a repetition rate of 10 Hz. The KTA crystals used in the mid-IR pump are XZ-cut ($\theta \approx 59°$) for type-II (eo-o) phase matching and AR-coated with ~500-MW/cm^2 damage threshold. The 2.7-µm signal is extracted after the pre-amplification OPA stage following a singly-resonant OPO. Electro-optic pulse slicing is enabled in this OPA stage via a high-speed Pockels cell (Leysop UPC068/2) with two KD_2PO_4 (DKDP) crystals operating at half-wave voltage. The pre-amplified mid-IR pump at 2.7 µm can operate at a reduced pulse duration of 1.2 ns.

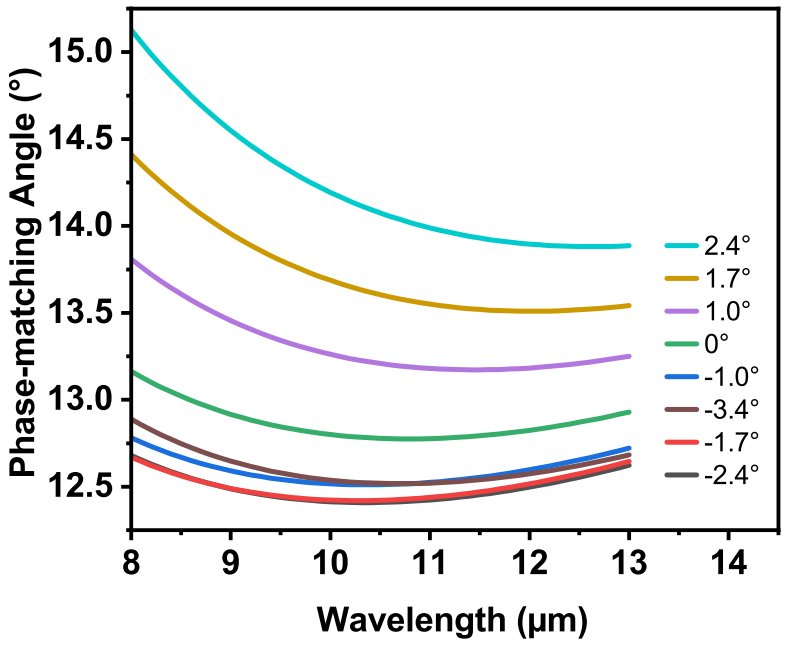

Figure A.6: Calculated phase-matching angles with respect to LWIR seed wavelengths at different internal noncollinear angles.

By reducing the pulse duration of the OPCPA pump, the LIDT intensity of the nonlinear crystal in the OPCPA amplifier can be scaled up, and the pulse duration of the pump can better match the pulse duration of the stretched seed in the nanosecond regime. Higher pump intensity reduces the required nonlinear medium's length for producing the same gain and, as a result, increases the parametric gain bandwidth in the OPCPA. Additionally, the parametric fluorescence is absent outside the temporal overlapping range of the pump and the seed pulses; therefore, better temporal contrast can be obtained. A power OPA boosts the energy of the generated 2.7-µm signal up to 10.5 mJ in a large-aperture (10 mm×10 mm), 25-mm long KTA crystal. The size of the 2.7-µm beam from the power OPA stage is 5.8 mm×4.9 mm, which preserves a uniform beam profile and a good beam quality with a M^2 value near 2.4. Due to the deployment of pulse slicing, a relatively large RMS energy fluctuation of 16.1% over 1800 pulses becomes a trade-off for a low timing jitter of 69 ps of the 2.7-µm pulses [233]. The 10-Hz Nd:YAG laser pump is synchronized with the 480-Hz Ti:sapphire regenerative amplifier such that only one out of 48 LWIR seed pulses is amplified in the GaSe noncollinear OPA.

To reach sufficient pump intensity on the GaSe, the 2.7-µm pump beam is resized by two CaF_2 relay lenses to ∼0.9 mm diameter. A reflective Galilean telescope resizes the LWIR seed beam to match the pump beam size before the stretcher. The stretcher and compressor in the Martinez-Treacy configuration employ 2-inch, 100-lines/mm, plane-ruled diffraction gratings (Thorlabs, GR2550-10106) to stretch the LWIR seed to ∼1 ns and recompress it after parametric amplification. A noncollinear OPA geometry with a GaSe crystal (z-cut, 5×5×5 mm^3, Eksma Optics) is implemented to amplify the LWIR seed pulses under Type-II (eo-e) phase matching condition. The noncollinear configuration is selected to avoid customized dichroic optics meeting the high-damage-threshold

requirements that are applied to combine and separate the pump and seed beams. The noncollinear geometry offers a supplementary degree of freedom in the phase-matching process and a potentially broader gain bandwidth. Figure A.6 illustrates the wavelength-dependent phase-matching angle for LWIR seed at different internal noncollinear angles. Broader phase-matching bandwidth can be achieved with flatter curves given a negative nonlinear angle. Based on the calculation, a combination of an internal noncollinear angle of -1.7° and a phase-matching angle of 12.4° would give an optimum OPCPA performance with high conversion efficiency and broad gain bandwidth [222]. By adopting the phase-matching configuration at a small phase-matching angle (the very left portion in Figure A.7), the incident angle of the pump and seed at the uncoated z-cut GaSe can be minimized, thus reducing the Fresnel reflection and enhancing the conversion efficiency.

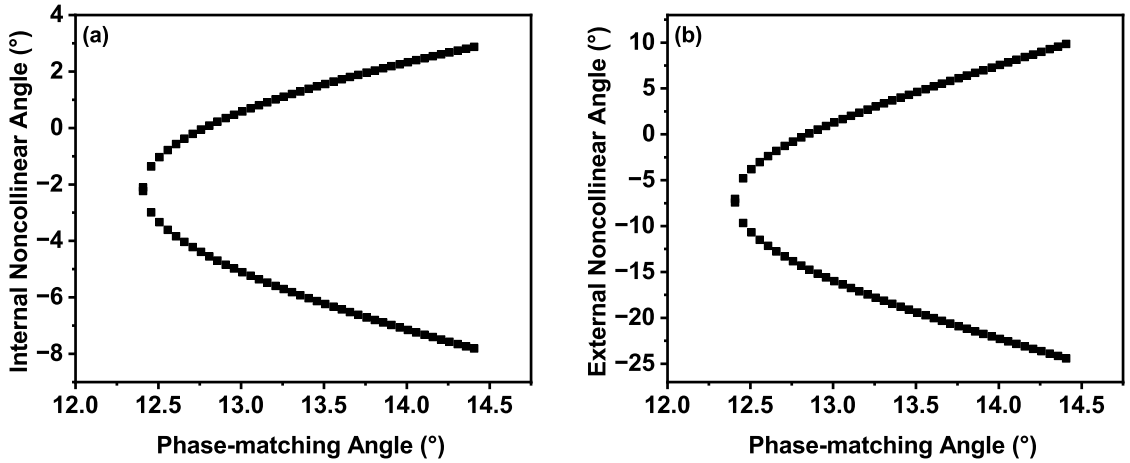

Figure A.7: Calculated phase-matching angles for LWIR seed pulse's central wavelength at different internal (a) and external (b) noncollinear angles.

A.3.2 Results and Discussion

The parametric gain of GaSe noncollinear OPA measured with a mercury-cadmium-telluride detector is shown in Figure A.8. The amplified LWIR seed has ∼two times more energy than the input, although order-of-magnitude less than that devised in the simulation with 1 GW/cm^2 pump intensity [222].

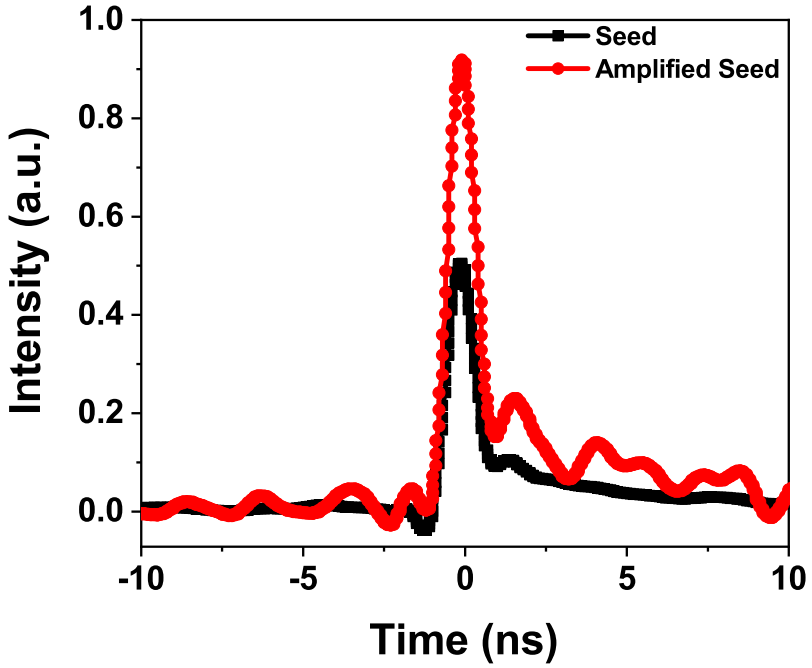

Figure A.8: Measured parametric gain in the GaSe noncollinear OPA.

The limited parametric amplification results can be attributed to two reasons: the GaSe crystal sample that was presumably damaged during the experiment and the pointing instability of the LWIR beam seeding OPCPA. As discussed in Chapter 1, the reported LIDT of nonlinear crystals often varies considerably. The GaSe crystal gains its foothold in the LWIR regime due to its broad transmission (<1–20 µm) and high nonlinearity. However, its reported LIDT in the literature ranges from <0.1 GW/cm^2

to >1 GW/cm^2, if scaled with the square root of the pulse duration [91], [100], [113], [114], [234]–[236]. The layered structure of GaSe with weak, van der Waals-typed interlayer bonding raises difficulties during the crystal growing and processing, making large, high optical quality (linear absorption coefficient $\alpha \leq$0.1–0.2 cm^{-1}) nearly unobtainable. Furthermore, accessing to other crystallographic directions besides z-cut and fine polishing and coating of GaSe are hampered because of its perfect cleavage and low hardness (close to 0 on the Mohs' scale) [237], leading to its inconsistent LIDT.

Figure A.9: Microscopic images of the GaSe crystal damaged in the OPCPA experiment. (a) Front surface (incident surface). (b) Back surface. (c) Bulk of the crystal by illuminating from the back.

Figure A.9 shows the microscopic images of the damaged GaSe crystal employed in the OPCPA experiment with conditions detailed in Section. A.3.1. The stretched LWIR seed beam and 2.7-µm pump beam incident on the front surface, creating millimeter and sub-millimeter-sized surface damage. Following surface damage of GaSe, the transmission of the two beams decreased substantially, and the crystal was translated perpendicularly to the beam path to resume the experiment. The back surface of the GaSe crystal shown in Figure A.9(b) appears to be undamaged. Nevertheless, more damage is revealed by observing the transmitted light through the bulk of the crystal. As shown in Figure A.9(c), radial and circular patterned shadows were observed in addition to the spots corresponding to the surface damage, indicating the shattering inside the crystal

due to the weak interlayer bonding of the GaSe crystal. The limitation induced by the properties of the GaSe crystal could be alleviated with multi-stage pumping techniques [78] and pumping with shorter (picosecond [78] or sub-picosecond [211], [212]) pulses. The latter method could also mitigate or eliminate the efforts needed to stretch the sub-picosecond LWIR seed pulses.

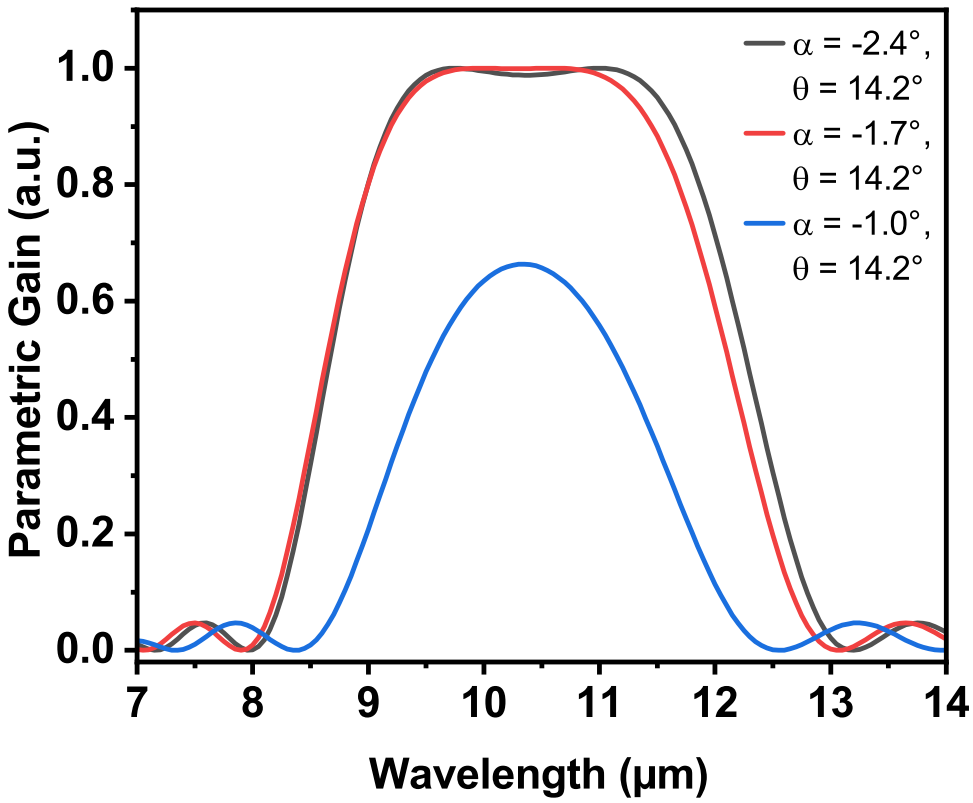

Figure A.10: Calculated parametric gain in the GaSe noncollinear OPA at different noncollinear angles but same phase-matching angle.

The beam-pointing instability leads to significant gain fluctuation, thus limiting the achieved gain in the experiments. Due to the arrangement of the lab, the LWIR seed pulses need to propagate for 8-m in the air before stretching. The maximum pointing

fluctuation of the residual Ti:sapphire pump in the LWIR seed generation stage induced by vibration and air turbulence is ∼0.5 mrad. The expected beam-pointing instability of the LWIR seed pulse is worse than that of the residual pump as a result of the collinear geometry used in the DFG. The beam-pointing instability weakens the parametric gain for almost all seed pulses by reducing the spatial overlap between the pump and LWIR seed pulses and diminishing the phase-matching bandwidth and efficiency at deviated noncollinear angles.

Figure A.10 shows the calculated parametric gain for three different internal noncollinear angles: -2.4°, -1.7°, and -1.0°. The calculated phase-matching angle for α= -1.7° is 14.2° and is applied for all three cases, which resemble the experimental conditions where the beam-pointing of the LWIR seed pulses fluctuates with respect to the pump pulses and GaSe crystal. When the internal noncollinear angle increases by only 0.7°, the parametric gain and bandwidth are reduced significantly (Figure A.10, blue). Whereas decreasing the internal noncollinear angle only slightly alters the parametric gain (Fig, A.10, black). The fluctuation of the beam-pointing of the LWIR seed beam leads to extreme difficulties in aligning the GaSe noncollinear OPA and thus affects its efficacy. Under our experimental conditions, an active beam-pointing control system is necessary to circumvent this obstacle and will be discussed in Chapter 4.

Bibliography

[1] H. M. Theodore, "Stimulated optical radiation in ruby," *Nature*, vol. 187, pp. 493–94, 1960.

[2] D. Kennedy and C. Norman, "What don't we know?" *Science*, vol. 309, no. 5731, pp. 75–75, 2005.

[3] A. H. Zewail, "Femtochemistry: Atomic-scale dynamics of the chemical bond," *The Journal of Physical Chemistry A*, vol. 104, no. 24, pp. 5660–5694, 2000.

[4] B. A. Remington, R. P. Drake, and D. D. Ryutov, "Experimental astrophysics with high power lasers and Z pinches," *Reviews of Modern Physics*, vol. 78, no. 3, p. 755, 2006.

[5] S. Bulanov, T. Z. Esirkepov, D. Habs, F. Pegoraro, and T. Tajima, "Relativistic laser-matter interaction and relativistic laboratory astrophysics," *The European Physical Journal D*, vol. 55, pp. 483–507, 2009.

[6] D. Habs, T. Tajima, J. Schreiber, C. Barty, M. Fujiwara, and P. Thirolf, "Vision of nuclear physics with photo-nuclear reactions by laser-driven beams," *The European Physical Journal D*, vol. 55, no. 2, p. 279, 2009.

[7] T. Tajima and J. M. Dawson, "Laser electron accelerator," *Physical Review Letters*, vol. 43, no. 4, p. 267, 1979.

[8] W. Lu, M. Tzoufras, C. Joshi, F. Tsung, W. Mori, J. Vieira, R. Fonseca, and L. Silva, "Generating multi-GeV electron bunches using single stage laser wakefield acceleration in a 3D nonlinear regime," *Physical Review Special Topics-Accelerators and Beams*, vol. 10, no. 6, p. 061 301, 2007.

[9] Z. Li, Y. Leng, and R. Li, "Further development of the short-pulse petawatt laser: Trends, technologies, and bottlenecks," *Laser & Photonics Reviews*, p. 2 100 705, 2022.

[10] F. J. McClung and R. W. Hellwarth, "Giant optical pulsations from ruby," *Applied Optics*, vol. 1, no. 101, pp. 103–105, 1962.

[11] L. Hargrove and M. Pollack, "Locking of He–Ne laser modes induced by synchronous intracavity modulation," *Applied Physics Letters*, vol. 5, no. 1, pp. 4–5, 1964.

[12] M. DiDomenico Jr, "Small-signal analysis of internal (coupling-type) modulation of lasers," *Journal of Applied Physics*, vol. 35, no. 10, pp. 2870–2876, 1964.

[13] A. Yariv, "Internal modulation in multimode laser oscillators," *Journal of Applied Physics*, vol. 36, no. 2, pp. 388–391, 1965.

[14] H. W. Mocker and R. J. Collins, "Mode competition and self-locking effects in a Q-switched ruby laser," *Applied Physics Letters*, vol. 7, no. 10, pp. 270–273, 1965.

[15] A. DeMaria, D. Stetser, and H. Heynau, "Self mode-locking of lasers with saturable absorbers," *Applied Physics Letters*, vol. 8, no. 7, pp. 174–176, 1966.

[16] D. Strickland and G. Mourou, "Compression of amplified chirped optical pulses," *Optics Communications*, vol. 55, no. 6, pp. 447–449, 1985.

[17] M. Perry, D. Pennington, B. Stuart, G. Tietbohl, J. Britten, C. Brown, S. Herman, B. Golick, M. Kartz, J. Miller, *et al.*, "Petawatt laser pulses," *Optics Letters*, vol. 24, no. 3, pp. 160–162, 1999.

[18] C. Barty, M. Key, J. Britten, R. Beach, G. Beer, C. Brown, S. Bryan, J. Caird, T. Carlson, J. Crane, *et al.*, "An overview of LLNL high-energy short-pulse technology for advanced radiography of laser fusion experiments," *Nuclear Fusion*, vol. 44, no. 12, S266, 2004.

[19] C. Danson, P. Brummitt, R. Clarke, J. Collier, B. Fell, A. Frackiewicz, S. Hancock, S. Hawkes, C. Hernandez-Gomez, P. Holligan, *et al.*, "Vulcan petawatt—an ultra-high-intensity interaction facility," *Nuclear Fusion*, vol. 44, no. 12, S239, 2004.

[20] K. Mima, H. Azechi, Y. Johzaki, Y. Kitagawa, R. Kodama, Y. Kozaki, N. Miyanaga, K. Nagai, H. Nagatomo, M. Nakai, *et al.*, "Present status of fast ignition research and prospects of FIREX project," *Fusion Science and Technology*, vol. 47, no. 3, pp. 662–666, 2005.

[21] L. Waxer, D. Maywar, J. Kelly, T. Kessler, B. Kruschwitz, S. Loucks, R. McCrory, D. Meyerhofer, S. Morse, C. Stoeckl, *et al.*, "High-energy petawatt capability for the OMEGA laser," *Optics and Photonics News*, vol. 16, no. 7, pp. 30–36, 2005.

[22] J. Zuegel, S. Borneis, C. Barty, B. Legarrec, C. Danson, N. Miyanaga, P. Rambo, C. Leblanc, T. Kessler, A. Schmid, *et al.*, "Laser challenges for fast ignition," *Fusion Science and Technology*, vol. 49, no. 3, pp. 453–482, 2006.

[23] S. Fujioka, Y. Arikawa, S. Kojima, T. Johzaki, H. Nagatomo, H. Sawada, S. H. Lee, T. Shiroto, N. Ohnishi, A. Morace, *et al.*, "Fast ignition realization experiment with high-contrast kilo-joule peta-watt LFEX laser and strong external magnetic field," *Physics of Plasmas*, vol. 23, no. 5, p. 056 308, 2016.

[24] P. F. Moulton, "Spectroscopic and laser characteristics of Ti:Al_2O_3," *J. Opt. Soc. Am. B*, vol. 3, pp. 125–133, 1986.

[25] J. Nees, A. Maksimchuk, G. Kalinchenko, B. Hou, Y. Ma, P. Campbell, A. McKelvey, L. Willingale, I. Jovanovic, C. Kuranz, *et al.*, "ZEUS: A National Science Foundation mid-scale facility for laser-driven science in the QED regime," in *2020 Conference on Lasers and Electro-Optics (CLEO)*, IEEE, 2020, pp. 1–2.

[26] W. Li, Z. Gan, L. Yu, C. Wang, Y. Liu, Z. Guo, L. Xu, M. Xu, Y. Hang, Y. Xu, *et al.*, "339 J high-energy Ti:sapphire chirped-pulse amplifier for 10 PW laser facility," *Optics Letters*, vol. 43, no. 22, pp. 5681–5684, 2018.

[27] F. Lureau, G. Matras, O. Chalus, C. Derycke, T. Morbieu, C. Radier, O. Casagrande, S. Laux, S. Ricaud, G. Rey, *et al.*, "High-energy hybrid femtosecond laser system demonstrating 2 × 10 PW capability," *High Power Laser Science and Engineering*, vol. 8, e43, 2020.

[28] C. Le Blanc, P. Curley, and F. Salin, "Gain-narrowing and gain-shifting of ultrashort pulses in Ti:sapphire amplifiers," *Optics Communications*, vol. 131, no. 4-6, pp. 391–398, 1996.

[29] H. Cao, Z. Gan, X. Liang, L. Yu, W. Li, Z. Guo, P. Huang, J. Wang, M. Xu, and Y. Hang, "Optical property measurements of 235 mm large-scale Ti:sapphire crystal," *Chinese Optics Letters*, vol. 16, no. 7, p. 071 401, 2018.

[30] A. Dubietis, G. Jonušauskas, and A. Piskarskas, "Powerful femtosecond pulse generation by chirped and stretched pulse parametric amplification in BBO crystal," *Optics Communications*, vol. 88, no. 4-6, pp. 437–440, 1992.

[31] J. Bromage, S.-W. Bahk, I. Begishev, C. Dorrer, M. Guardalben, B. Hoffman, J. Oliver, R. Roides, E. Schiesser, M. Shoup Iii, *et al.*, "Technology development for

ultraintense all-OPCPA systems," *High Power Laser Science and Engineering*, vol. 7, e4, 2019.

[32] D. Xu, B. Shen, J. Xu, and Z. Liang, "XFEL beamline design for vacuum birefringence experiment," *Nuclear Instruments and Methods in Physics Research Section A: Accelerators, Spectrometers, Detectors and Associated Equipment*, vol. 982, p. 164 553, 2020.

[33] X. Wang, X. Liu, X. Lu, J. Chen, Y. Long, W. Li, H. Chen, X. Chen, P. Bai, Y. Li, *et al.*, "13.4 fs, 0.1 Hz OPCPA front end for the 100 PW-class laser facility," *Ultrafast Science*, 2022.

[34] Z. Li, Y. Kato, and J. Kawanaka, "Simulating an ultra-broadband concept for Exawatt-class lasers," *Scientific Reports*, vol. 11, no. 1, p. 151, 2021.

[35] U. Morgner, F. X. Kärtner, S.-H. Cho, Y. Chen, H. A. Haus, J. G. Fujimoto, E. P. Ippen, V. Scheuer, G. Angelow, and T. Tschudi, "Sub-two-cycle pulses from a Kerr-lens mode-locked Ti:sapphire laser," *Optics Letters*, vol. 24, no. 6, pp. 411–413, 1999.

[36] D. H. Sutter, G. Steinmeyer, L. Gallmann, N. Matuschek, F. Morier-Genoud, U. Keller, V. Scheuer, G. Angelow, and T. Tschudi, "Semiconductor saturable-absorber mirror-assisted Kerr-lens mode-locked Ti:sapphire laser producing pulses in the two-cycle regime," *Optics Letters*, vol. 24, no. 9, pp. 631–633, 1999.

[37] T. Brabec and F. Krausz, "Intense few-cycle laser fields: Frontiers of nonlinear optics," *Reviews of Modern Physics*, vol. 72, no. 2, p. 545, 2000.

[38] F. Krausz and M. Ivanov, "Attosecond physics," *Reviews of Modern Physics*, vol. 81, no. 1, p. 163, 2009.

[39] J. Kim and Y. Song, "Ultralow-noise mode-locked fiber lasers and frequency combs: Principles, status, and applications," *Advances in Optics and Photonics*, vol. 8, no. 3, pp. 465–540, 2016.

[40] T. Udem, J. Reichert, R. Holzwarth, and T. Hänsch, "Accurate measurement of large optical frequency differences with a mode-locked laser," *Optics Letters*, vol. 24, no. 13, pp. 881–883, 1999.

[41] H. R. Telle, G. Steinmeyer, A. E. Dunlop, J. Stenger, D. H. Sutter, and U. Keller, "Carrier-envelope offset phase control: A novel concept for absolute optical frequency measurement and ultrashort pulse generation," *Applied Physics B*, vol. 69, pp. 327–332, 1999.

[42] D. J. Jones, S. A. Diddams, J. K. Ranka, A. Stentz, R. S. Windeler, J. L. Hall, and S. T. Cundiff, "Carrier-envelope phase control of femtosecond mode-locked lasers and direct optical frequency synthesis," *Science*, vol. 288, no. 5466, pp. 635–639, 2000.

[43] C.-C. Lee, C. Mohr, J. Bethge, S. Suzuki, M. Fermann, I. Hartl, and T. Schibli, "Frequency comb stabilization with bandwidth beyond the limit of gain lifetime by an intracavity graphene electro-optic modulator," *Optics Letters*, vol. 37, no. 15, pp. 3084–3086, 2012.

[44] L. C. Sinclair, J.-D. Deschênes, L. Sonderhouse, W. C. Swann, I. H. Khader, E. Baumann, N. R. Newbury, and I. Coddington, "Invited article: A compact optically coherent fiber frequency comb," *Review of Scientific Instruments*, vol. 86, no. 8, p. 081 301, 2015.

[45] N. Kuse, C.-C. Lee, J. Jiang, C. Mohr, T. Schibli, and M. Fermann, "Ultra-low noise all polarization-maintaining Er fiber-based optical frequency combs facili-

tated with a graphene modulator," *Optics Express*, vol. 23, no. 19, pp. 24 342–24 350, 2015.

[46] N. Kuse, J. Jiang, C.-C. Lee, T. Schibli, and M. Fermann, "All polarization-maintaining Er fiber-based optical frequency combs with nonlinear amplifying loop mirror," *Optics Express*, vol. 24, no. 3, pp. 3095–3102, 2016.

[47] A. Baltuška, T. Fuji, and T. Kobayashi, "Controlling the carrier-envelope phase of ultrashort light pulses with optical parametric amplifiers," *Physical Review Letters*, vol. 88, no. 13, p. 133 901, 2002.

[48] G. Krauss, D. Fehrenbacher, D. Brida, C. Riek, A. Sell, R. Huber, and A. Leitenstorfer, "All-passive phase locking of a compact Er: fiber laser system," *Optics Letters*, vol. 36, no. 4, pp. 540–542, 2011.

[49] H. Huang, X. Xiao, M. Burger, J. Nees, and I. Jovanovic, "Ultra-broadband long-wave-infrared pulse production using a chirped-pulse difference-frequency generation," *Optics Letters*, vol. 47, no. 13, pp. 3159–3162, 2022.

[50] A. Braun, G. Korn, X. Liu, D. Du, J. Squier, and G. Mourou, "Self-channeling of high-peak-power femtosecond laser pulses in air," *Optics Letters*, vol. 20, no. 1, pp. 73–75, 1995.

[51] E. Nibbering, P. Curley, G. Grillon, B. Prade, M. A. Franco, F. Salin, and A. Mysyrowicz, "Conical emission from self-guided femtosecond pulses in air," *Optics Letters*, vol. 21, no. 1, pp. 62–64, 1996.

[52] M. Rodriguez, R. Bourayou, G. Méjean, J. Kasparian, J. Yu, E. Salmon, A. Scholz, B. Stecklum, J. Eislöffel, U. Laux, *et al.*, "Kilometer-range nonlinear propagation of femtosecond laser pulses," *Physical Review E*, vol. 69, no. 3, p. 036 607, 2004.

[53] J. Kasparian, M. Rodríguez, G. Méjean, J. Yu, E. Salmon, H. Wille, R. Bourayou, S. Frey, Y.-B. André, A. Mysyrowicz, *et al.*, "White-light filaments for atmospheric analysis," *Science*, vol. 301, no. 5629, pp. 61–64, 2003.

[54] J. H. Marburger, "Self-focusing: Theory," *Progress in Quantum Electronics*, vol. 4, pp. 35–110, 1975.

[55] Wikipedia contributors, *Infrared window — Wikipedia, the free encyclopedia*, https://en.m.wikipedia.org/wiki/File:Atmosfaerisk_spredning-en.svg.

[56] J. N. Howard and J. S. Garing, "The transmission of the atmosphere in the infrared—a review," *Infrared Physics*, vol. 2, no. 3, pp. 155–173, 1962.

[57] P. Panagiotopoulos, P. Rosenow, K. Schuh, M. Kolesik, E. Wright, S. Koch, and J. Moloney, "Simulation of LWIR TW ultrashort pulses over kilometer ranges in the atmosphere," in *Ultrafast Bandgap Photonics III*, SPIE, vol. 10638, 2018, pp. 151–163.

[58] S. V. Chekalin and V. P. Kandidov, "From self-focusing light beams to femtosecond laser pulse filamentation," *Physics-Uspekhi*, vol. 56, no. 2, p. 123, 2013.

[59] A. Mitrofanov, A. Voronin, D. Sidorov-Biryukov, A. Pugžlys, E. Stepanov, G. Andriukaitis, T. Flöry, S. Ališauskas, A. Fedotov, A. Baltuška, *et al.*, "Mid-infrared laser filaments in the atmosphere," *Scientific Reports*, vol. 5, no. 1, p. 8368, 2015.

[60] A. V. Mitrofanov, D. A. Sidorov-Biryukov, A. A. Voronin, A. Pugžlys, G. Andriukaitis, E. A. Stepanov, S. Ališauskas, T. Flöry, A. B. Fedotov, V. Y. Panchenko, *et al.*, "Subterawatt femtosecond pulses in the mid-infrared range: New spatiotemporal dynamics of high-power electromagnetic fields," *Physics-Uspekhi*, vol. 58, no. 1, p. 89, 2015.

[61] A. Zheltikov, "Laser-induced filaments in the mid-infrared," *Journal of Physics B: Atomic, Molecular and Optical Physics*, vol. 50, no. 9, p. 092 001, 2017.

[62] S. Tochitsky, E. Welch, M. Polyanskiy, I. Pogorelsky, P. Panagiotopoulos, M. Kolesik, E. M. Wright, S. W. Koch, J. V. Moloney, J. Pigeon, and C. Joshi, "Megafilament in air formed by self-guided terawatt long-wavelength infrared laser," *Nature Photonics*, vol. 13, no. 1, pp. 41–46, 2019.

[63] L. Keldysh *et al.*, "Ionization in the field of a strong electromagnetic wave," *Sov. Phys. JETP*, vol. 20, no. 5, pp. 1307–1314, 1965.

[64] M. Tacke, "Lead-salt lasers," *Philosophical Transactions of the Royal Society of London. Series A: Mathematical, Physical and Engineering Sciences*, vol. 359, no. 1780, pp. 547–566, 2001.

[65] P. Täschler, M. Bertrand, B. Schneider, M. Singleton, P. Jouy, F. Kapsalidis, M. Beck, and J. Faist, "Femtosecond pulses from a mid-infrared quantum cascade laser," *Nature Photonics*, vol. 15, no. 12, pp. 919–924, 2021.

[66] P. G. O'Shea and H. P. Freund, "Free-electron lasers: Status and applications," *Science*, vol. 292, no. 5523, pp. 1853–1858, 2001.

[67] W. Barletta, J. Bisognano, J. Corlett, P. Emma, Z. Huang, K.-J. Kim, R. Lindberg, J. Murphy, G. Neil, D. Nguyen, *et al.*, "Free electron lasers: Present status and future challenges," *Nuclear Instruments and Methods in Physics Research Section A: Accelerators, Spectrometers, Detectors and Associated Equipment*, vol. 618, no. 1-3, pp. 69–96, 2010.

[68] D. Haberberger, S. Tochitsky, and C. Joshi, "Fifteen terawatt picosecond CO_2 laser system," *Optics Express*, vol. 18, no. 17, pp. 17 865–17 875, 2010.

[69] M. N. Polyanskiy, I. V. Pogorelsky, M. Babzien, and M. A. Palmer, "Demonstration of a 2 ps, 5 TW peak power, long-wave infrared laser based on chirped-pulse amplification with mixed-isotope CO_2 amplifiers," *OSA Continuum*, vol. 3, no. 3, pp. 459–472, 2020.

[70] D. Tovey, S. Y. Tochitsky, J. Pigeon, G. Louwrens, M. Polyanskiy, I. Ben-Zvi, and C. Joshi, "Multi-atmosphere picosecond CO_2 amplifier optically pumped at 4.3 µm," *Applied Optics*, vol. 58, no. 21, pp. 5756–5763, 2019.

[71] D. Tovey, J. Pigeon, S. Tochitsky, G. Louwrens, I. Ben-Zvi, D. Martyshkin, V. Fedorov, K. Karki, S. Mirov, and C. Joshi, "Lasing in 15 atm CO_2 cell optically pumped by a Fe: ZnSe laser," *Optics Express*, vol. 29, no. 20, pp. 31 455–31 464, 2021.

[72] J. Pigeon, S. Tochitsky, and C. Joshi, "Nonlinear optical compression of high-power 10-µm CO_2 laser pulses in gases and semiconductors," in *AIP Conference Proceedings*, AIP Publishing LLC, vol. 1812, 2017, p. 110 003.

[73] P. Panagiotopoulos, M. G. Hastings, M. Kolesik, S. Tochitsky, and J. V. Moloney, "Multi-terawatt femtosecond 10 µm laser pulses by self-compression in a CO_2 cell," *OSA Continuum*, vol. 3, no. 11, pp. 3040–3047, 2020.

[74] Z. Zhao, B. Wu, X. Wang, Z. Pan, Z. Liu, P. Zhang, X. Shen, Q. Nie, S. Dai, and R. Wang, "Mid-infrared supercontinuum covering 2.0–16 µm in a low-loss telluride single-mode fiber," *Laser & Photonics Reviews*, vol. 11, no. 2, p. 1 700 005, 2017.

[75] C. R. Petersen, U. Møller, I. Kubat, B. Zhou, S. Dupont, J. Ramsay, T. Benson, S. Sujecki, N. Abdel-Moneim, Z. Tang, *et al.*, "Mid-infrared supercontinuum covering the 1.4–13.3 µm molecular fingerprint region using ultra-high NA chalcogenide step-index fibre," *Nature Photonics*, vol. 8, no. 11, pp. 830–834, 2014.

[76] T. Sylvestre, E. Genier, A. N. Ghosh, P. Bowen, G. Genty, J. Troles, A. Mussot, A. C. Peacock, M. Klimczak, A. M. Heidt, *et al.*, "Recent advances in supercontinuum generation in specialty optical fibers," *J. Opt. Soc. Am. B*, vol. 38, no. 12, F90–F103, 2021.

[77] I. Jovanovic, B. J. Comaskey, C. A. Ebbers, R. A. Bonner, D. M. Pennington, and E. C. Morse, "Optical parametric chirped-pulse amplifier as an alternative to Ti:sapphire regenerative amplifiers," *Applied Optics*, vol. 41, no. 15, pp. 2923–2929, 2002.

[78] P. Fuertjes, M. Bock, L. von Grafenstein, D. Ueberschaer, U. Griebner, and T. Elsaesser, "Few-cycle 65-µJ pulses at 11.4 µm for ultrafast nonlinear longwave-infrared spectroscopy," *Optica*, vol. 9, no. 11, pp. 1303–1306, 2022.

[79] Z. Heiner, V. Petrov, V. L. Panyutin, V. V. Badikov, K. Kato, K. Miyata, and M. Mero, "Efficient generation of few-cycle pulses beyond 10 µm from an optical parametric amplifier pumped by a 1-µm laser system," *Scientific Reports*, vol. 12, no. 1, p. 5082, 2022.

[80] Q. Cao, F. X. Kärtner, and G. Chang, "Towards high power longwave mid-IR frequency combs: power scalability of high repetition-rate difference-frequency generation," *Optics Express*, vol. 28, no. 2, pp. 1369–1384, 2020.

[81] C. Phillips, J. Jiang, C. Mohr, A. Lin, C. Langrock, M. Snure, D. Bliss, M. Zhu, I. Hartl, J. Harris, *et al.*, "Widely tunable midinfrared difference frequency generation in orientation-patterned GaAs pumped with a femtosecond Tm-fiber system," *Optics Letters*, vol. 37, no. 14, pp. 2928–2930, 2012.

[82] R. Becheker, M. Bailly, S. Idlahcen, T. Godin, B. Gerard, H. Delahaye, G. Granger, S. Fèvrier, A. Grisard, E. Lallier, *et al.*, "Optical parametric gener-

ation in OP-GaAs waveguides pumped by a femtosecond fluoride fiber laser," *Optics Letters*, vol. 47, no. 4, pp. 886–889, 2022.

[83] L. Maidment, P. G. Schunemann, and D. T. Reid, "Molecular fingerprint-region spectroscopy from 5 to 12 µm using an orientation-patterned gallium phosphide optical parametric oscillator," *Optics Letters*, vol. 41, no. 18, pp. 4261–4264, 2016.

[84] K. Krzempek, D. Tomaszewska, A. Głuszek, T. Martynkien, P. Mergo, J. Sotor, A. Foltynowicz, and G. Soboń, "Stabilized all-fiber source for generation of tunable broadband f_{CEO}-free mid-IR frequency comb in the 7–9 µm range," *Optics Express*, vol. 27, no. 26, pp. 37 435–37 445, 2019.

[85] P. G. Schunemann, K. T. Zawilski, L. A. Pomeranz, D. J. Creeden, and P. A. Budni, "Advances in nonlinear optical crystals for mid-infrared coherent sources," *J. Opt. Soc. Am. B*, vol. 33, no. 11, pp. D36–D43, 2016.

[86] K. L. Vodopyanov, "Parametric generation of tunable infrared radiation in $ZnGeP_2$ and GaSe pumped at 3 µm," *J. Opt. Soc. Am. B*, vol. 10, no. 9, pp. 1723–1729, 1993.

[87] K. Vodopyanov, L. Kulevskii, V. Voevodin, A. Gribenyukov, K. Allakhverdiev, and T. Kerimov, "High efficiency middle IR parametric superradiance in $ZnGeP_2$ and GaSe crystals pumped by an erbium laser," *Optics Communications*, vol. 83, no. 5-6, pp. 322–326, 1991.

[88] V. V. Badikov, O. Pivovarov, Y. V. Skokov, O. Skrebneva, and N. Trotsenko, "Some optical properties of silver thiogallate single crystals," *Soviet Journal of Quantum Electronics*, vol. 5, no. 3, p. 350, 1975.

[89] N. P. Barnes, D. J. Gettemy, J. R. Hietanen, *et al.*, "Parametric amplification in $AgGaSe_2$," *Applied Optics*, vol. 28, no. 23, pp. 5162–5168, 1989.

[90] A. Novoselova and V. Lazarev, *Physical and chemical properties of semiconductors*. Nauka, Moscow, 1978.

[91] F. Adduci, I. Catalano, A. Cingolani, and A. Minafra, "Direct and indirect two-photon processes in layered semiconductors," *Physical Review B*, vol. 15, no. 2, p. 926, 1977.

[92] G. C. Catella and D. Burlage, "Crystal growth and optical properties of $AgGaS_2$ and $AgGaSe_2$," *MRS Bulletin*, vol. 23, no. 7, pp. 28–36, 1998.

[93] M. J. Weber, *CRC handbook of laser science and technology supplement 2: optical materials*. CRC Press, 2020.

[94] W. Shi and Y. J. Ding, "Continuously tunable and coherent terahertz radiation by means of phase-matched difference-frequency generation in zinc germanium phosphide," *Applied Physics Letters*, vol. 83, no. 5, pp. 848–850, 2003.

[95] R. Wu, K. Lai, E. Lau, H. Wong, W. Xie, Y. Lim, K. Lim, and L. Chia, "Multi-watt ZGP OPO based on diffusion bonded walkoff compensated KTP OPO and Nd:YALO laser," in *Advanced Solid State Lasers*, Optica Publishing Group, 2002, TuA4.

[96] T. H. Allik, S. Chandra, D. M. Rines, P. G. Schunemann, J. A. Hutchinson, and R. Utano, "Tunable 7–12-μm optical parametric oscillator using a Cr, Er:YSGG laser to pump CdSe and $ZnGeP_2$ crystals," *Optics Letters*, vol. 22, no. 9, pp. 597–599, 1997.

[97] G. Boyd, W. Gandrud, and E. Buehler, "Phase-matched up conversion of 10.6-μm radiation in $ZnGeP_2$," *Applied Physics Letters*, vol. 18, no. 10, pp. 446–448, 1971.

[98] A. Bianchi, A. Ferrario, and M. Musci, "4–12 µm tunable down-conversion in GaSe from a $LiNbO_3$ parametric oscillator," *Optics Communications*, vol. 25, no. 2, pp. 256–258, 1978.

[99] N. Barnes, R. Eckhardt, D. Gettemy, and L. Edgett, "Absorption coefficients and the temperature variation of the refractive index difference of nonlinear optical crystals," *IEEE Journal of Quantum Electronics*, vol. 15, no. 10, pp. 1074–1076, 1979.

[100] A. Okorogu, S. Mirov, W. Lee, D. Crouthamel, N. Jenkins, A. Y. Dergachev, K. Vodopyanov, and V. Badikov, "Tunable middle infrared downconversion in GaSe and $AgGaS_2$," *Optics Communications*, vol. 155, no. 4-6, pp. 307–312, 1998.

[101] S. Chandra, T. H. Allik, G. Catella, and J. A. Hutchinson, "Tunable output around 8 µm from a single step $AgGaS_2$ OPO pumped at 1.064 µm," in *Advanced Solid State Lasers*, Optica Publishing Group, 1998, FC15.

[102] G. Catella, L. Shiozawa, J. Hietanen, R. Eckardt, R. Route, R. Feigelson, D. Cooper, and C. Marquardt, "Mid-IR absorption in $AgGaSe_2$ optical parametric oscillator crystals," *Applied Optics*, vol. 32, no. 21, pp. 3948–3951, 1993.

[103] H. Komine, J. Fukumoto, W. Long, and E. Stappaerts, "Noncritically phase matched mid-infrared generation in $AgGaSe_2$," *IEEE Journal of Selected Topics in Quantum Electronics*, vol. 1, no. 1, pp. 44–49, 1995.

[104] C. L. Marquardt, D. G. Cooper, P. Budni, M. Knights, K. Schepler, R. DeDomenico, and G. Catella, "Thermal lensing in silver gallium selenide parametric oscillator crystals," *Applied Optics*, vol. 33, no. 15, pp. 3192–3197, 1994.

[105] V. Petrov, F. Rotermund, F. Noack, and P. Schunemann, "Femtosecond parametric generation in $ZnGeP_2$," *Optics Letters*, vol. 24, no. 6, pp. 414–416, 1999.

[106] I. B. Zotova and Y. J. Ding, "Spectral measurements of two-photon absorption coefficients for CdSe and GaSe crystals," *Applied Optics*, vol. 40, no. 36, pp. 6654–6658, 2001.

[107] J. Song, J. Xia, Z. Zhang, and D. Strickland, "Mid-infrared pulses generated from the mixing output of an amplified, dual-wavelength Ti:sapphire system," *Optics Letters*, vol. 27, no. 3, pp. 200–202, 2002.

[108] A. Bugaev, G. Averkieva, and V. Prochukhan, "Two-photon absorption and non-stationary energy transfer in the ternary semiconductor $AgGaSe_2$," *Physics of the Solid State*, vol. 37, no. 8, pp. 1367–1370, 1995.

[109] G. Boyd, E. Buehler, and F. Storz, "Linear and nonlinear optical properties of $ZnGeP_2$ and CdSe," *Applied Physics Letters*, vol. 18, no. 7, pp. 301–304, 1971.

[110] P. Budni, L. Pomeranz, M. Lemons, P. Schunemann, T. Pollak, and E. P. Chicklis, "10 W mid-IR holmium pumped $ZnGeP_2$ OPO," in *Advanced Solid State Lasers*, Optica Publishing Group, 1998, FC1.

[111] K. L. Vodop'yanov, Y. A. Andreev, and G. Bhar, "Parametric superluminescence in a $ZnGeP_2$ crystal with temperature tuning and pumping by an erbium laser," *Quantum Electronics*, vol. 23, no. 9, p. 763, 1993.

[112] G. Zhou, Q. Cao, F. X. Kärtner, and G. Chang, "Energy scalable, offset-free ultrafast mid-infrared source harnessing self-phase-modulation-enabled spectral selection," *Optics Letters*, vol. 43, no. 12, pp. 2953–2956, 2018.

[113] T. Dahinten, U. Plodereder, A. Seilmeier, K. Vodopyanov, K. Allakhverdiev, and Z. Ibragimov, "Infrared pulses of 1 picosecond duration tunable between 4 µm and 18 µm," *IEEE Journal of Quantum Electronics*, vol. 29, no. 7, pp. 2245–2250, 1993.

[114] G. Abdullaev, K. Allakhverdiev, L. Kulevskii, A. Prokhorov, E. Y. Salaev, A. Savel'Ev, and V. Smirnov, "Parametric conversion of infrared radiation in a GaSe crystal," *Soviet Journal of Quantum Electronics*, vol. 5, no. 6, p. 665, 1975.

[115] K. Vodopyanov and V. Voevodin, "2.8 µm laser pumped type I and type II travelling-wave optical parametric generator in GaSe," *Optics Communications*, vol. 114, no. 3-4, pp. 333–335, 1995.

[116] T. Elsaesser, A. Seilmeier, W. Kaiser, P. Koidl, and G. Brandt, "Parametric generation of tunable picosecond pulses in the medium infrared using $AgGaS_2$ crystals," *Applied Physics Letters*, vol. 44, no. 4, pp. 383–385, 1984.

[117] S. Haidar, K. Nakamura, E. Niwa, K. Masumoto, and H. Ito, "Mid-infrared (5–12-µm) and limited (5.5–8.5-µm) single-knob tuning generated by difference-frequency mixing in single-crystal $AgGaS_2$," *Applied Optics*, vol. 38, no. 9, pp. 1798–1801, 1999.

[118] R. Eckardt, Y. Fan, R. Byer, C. Marquardt, M. Storm, and L. Esterowitz, "Broadly tunable infrared parametric oscillator using $AgGaSe_2$," *Applied Physics Letters*, vol. 49, no. 11, pp. 608–610, 1986.

[119] S. Chandra, T. H. Allik, G. Catella, R. Utano, and J. A. Hutchinson, "Continuously tunable, 6–14 µm silver-gallium selenide optical parametric oscillator pumped at 1.57 µm," *Applied Physics Letters*, vol. 71, no. 5, pp. 584–586, 1997.

[120] P. Budni, M. Knights, E. Chicklis, and K. Schepler, "Kilohertz $AgGaSe_2$ optical parametric oscillator pumped at 2 µm," *Optics Letters*, vol. 18, no. 13, pp. 1068–1070, 1993.

[121] J. Kirton, "A 2.54 µm-pumped type II $AgGaSe_2$ mid-IR optical parametric oscillator," *Optics Communications*, vol. 115, no. 1-2, pp. 93–98, 1995.

[122] B. Stuart, M. Feit, A. Rubenchik, B. Shore, and M. Perry, "Laser-induced damage in dielectrics with nanosecond to subpicosecond pulses," *Physical Review Letters*, vol. 74, no. 12, p. 2248, 1995.

[123] B. Stuart, M. Feit, S. Herman, A. Rubenchik, B. Shore, and M. Perry, "Nanosecond-to-femtosecond laser-induced breakdown in dielectrics," *Physical Review B*, vol. 53, no. 4, p. 1749, 1996.

[124] I. Jovanovic, C. Brown, B. Wattellier, N. Nielsen, W. Molander, B. Stuart, D. Pennington, and C. Barty, "Precision short-pulse damage test station utilizing optical parametric chirped-pulse amplification," *Review of Scientific Instruments*, vol. 75, no. 12, pp. 5193–5202, 2004.

[125] R. Hardin and F. Tappert, "Applications of the split-step Fourier method to the numerical solution of nonlinear and variable coefficient wave equations," *SIAM Review (Chronicles)*, vol. 15, 1973.

[126] Y. Cui, H. Huang, Y. Bai, W. Du, M. Chen, B. Zhou, I. Jovanovic, and A. Galvanauskas, "Long-wave-infrared pulse production at 11 µm via difference-frequency generation driven by femtosecond mid-infrared all-fluoride fiber laser," *Optics Letters*, vol. 48, no. 7, pp. 1890–1893, 2023.

[127] I. T. Sorokina and K. L. Vodopyanov, *Solid-state mid-infrared laser sources*. Springer Science & Business Media, 2003, vol. 89.

[128] A. Schliesser, N. Picqué, and T. W. Hänsch, "Mid-infrared frequency combs," *Nature Photonics*, vol. 6, no. 7, pp. 440–449, 2012.

[129] T. Popmintchev, M.-C. Chen, D. Popmintchev, P. Arpin, S. Brown, S. Ališauskas, G. Andriukaitis, T. Balčiunas, O. D. Mücke, A. Pugzlys, *et al.*, "Bright coher-

ent ultrahigh harmonics in the keV x-ray regime from mid-infrared femtosecond lasers," *Science*, vol. 336, no. 6086, pp. 1287–1291, 2012.

[130] N. Nagl, K. F. Mak, Q. Wang, V. Pervak, F. Krausz, and O. Pronin, "Efficient femtosecond mid-infrared generation based on a Cr: ZnS oscillator and step-index fluoride fibers," *Optics Letters*, vol. 44, no. 10, pp. 2390–2393, 2019.

[131] E. Migal, A. Pushkin, B. Bravy, V. Gordienko, N. Minaev, A. Sirotkin, and F. Potemkin, "3.5-mJ 150-fs Fe:ZnSe hybrid mid-IR femtosecond laser at 4.4 µm for driving extreme nonlinear optics," *Optics Letters*, vol. 44, no. 10, pp. 2550–2553, 2019.

[132] A. Ruehl, A. Gambetta, I. Hartl, M. E. Fermann, K. S. Eikema, and M. Marangoni, "Widely-tunable mid-infrared frequency comb source based on difference frequency generation," *Optics Letters*, vol. 37, no. 12, pp. 2232–2234, 2012.

[133] Y. Yao and W. H. Knox, "Broadly tunable femtosecond mid-infrared source based on dual photonic crystal fibers," *Optics Express*, vol. 21, no. 22, pp. 26 612–26 619, 2013.

[134] A. Gambetta, N. Coluccelli, M. Cassinerio, D. Gatti, P. Laporta, G. Galzerano, and M. Marangoni, "Milliwatt-level frequency combs in the 8–14 µm range via difference frequency generation from an Er: fiber oscillator," *Optics Letters*, vol. 38, no. 7, pp. 1155–1157, 2013.

[135] K. Iwakuni, G. Porat, T. Q. Bui, B. J. Bjork, S. B. Schoun, O. H. Heckl, M. E. Fermann, and J. Ye, "Phase-stabilized 100 mW frequency comb near 10 µm," *Applied Physics B*, vol. 124, no. 7, pp. 1–7, 2018.

[136] S. D. Jackson, "Towards high-power mid-infrared emission from a fibre laser," *Nature Photonics*, vol. 6, no. 7, pp. 423–431, 2012.

[137] M. Pollnan and S. D. Jackson, "Erbium 3-µm fiber lasers," *IEEE Journal of Selected Topics in Quantum Electronics*, vol. 7, no. 1, pp. 30–40, 2001.

[138] A. Gambetta, R. Ramponi, and M. Marangoni, "Mid-infrared optical combs from a compact amplified Er-doped fiber oscillator," *Optics Letters*, vol. 33, no. 22, pp. 2671–2673, 2008.

[139] D. G. Winters, P. Schlup, and R. A. Bartels, "Subpicosecond fiber-based soliton-tuned mid-infrared source in the 9.7–14.9 µm wavelength region," *Optics Letters*, vol. 35, no. 13, pp. 2179–2181, 2010.

[140] D. Churin, K. Kieu, R. A. Norwood, and N. Peyghambarian, "Efficient frequency comb generation in the 9-µm region using compact fiber sources," *IEEE Photonics Technology Letters*, vol. 26, no. 22, pp. 2271–2274, 2014.

[141] K. F. Lee, C. J. Hensley, P. G. Schunemann, and M. Fermann, "Midinfrared frequency comb by difference frequency of erbium and thulium fiber lasers in orientation-patterned gallium phosphide," *Optics Express*, vol. 25, no. 15, pp. 17 411–17 416, 2017.

[142] J. Sotor, T. Martynkien, P. G. Schunemann, P. Mergo, L. Rutkowski, and G. Soboń, "All-fiber mid-infrared source tunable from 6 to 9 µm based on difference frequency generation in OP-GaP crystal," *Optics Express*, vol. 26, no. 9, pp. 11 756–11 763, 2018.

[143] J. P. Gordon, "Theory of the soliton self-frequency shift," *Optics Letters*, vol. 11, no. 10, pp. 662–664, 1986.

[144] Y. Cui, M. Chen, W. Du, Y. Bai, and A. Galvanauskas, "Generation of 85 fs mid-IR pulses with up to 2.4 W average power using an Er: ZBLAN fiber mode-locked

oscillator and a nonlinear amplifier," *Optics Express*, vol. 29, no. 26, pp. 42 924–42 931, 2021.

[145] L. Yu, J. Liang, S. Huang, J. Wang, J. Wang, X. Luo, P. Yan, F. Dong, X. Liu, Q. Lue, *et al.*, "Average-power (4.13 W) 59 fs mid-infrared pulses from a fluoride fiber laser system," *Optics Letters*, vol. 47, no. 10, pp. 2562–2565, 2022.

[146] S. Duval, J.-C. Gauthier, L.-R. Robichaud, P. Paradis, M. Olivier, V. Fortin, M. Bernier, M. Piché, and R. Vallée, "Watt-level fiber-based femtosecond laser source tunable from 2.8 to 3.6 µm," *Optics Letters*, vol. 41, no. 22, pp. 5294–5297, 2016.

[147] Y. Tang, L. G. Wright, K. Charan, T. Wang, C. Xu, and F. W. Wise, "Generation of intense 100 fs solitons tunable from 2 to 4.3 µm in fluoride fiber," *Optica*, vol. 3, no. 9, pp. 948–951, 2016.

[148] J.-C. Gauthier, M. Olivier, P. Paradis, M.-F. Dumas, M. Bernier, and R. Vallée, "Femtosecond tunable solitons up to 4.8 µm using soliton self-frequency shift in an InF_3 fiber," *Scientific Reports*, vol. 12, no. 1, pp. 1–14, 2022.

[149] Arlee Smith, *SNLO Software*, https://as-photonics.com/products/snlo/.

[150] F. M. Mitschke and L. F. Mollenauer, "Discovery of the soliton self-frequency shift," *Optics Letters*, vol. 11, no. 10, pp. 659–661, 1986.

[151] L. Yuan, Z. He, G. Lv, Y. Wang, C. Li, J. Wang, *et al.*, "Optical design, laboratory test, and calibration of airborne long wave infrared imaging spectrometer," *Optics Express*, vol. 25, no. 19, pp. 22 440–22 454, 2017.

[152] G. Zhou, M. Xin, F. X. Kaertner, and G. Chang, "Timing jitter of Raman solitons," *Optics Letters*, vol. 40, no. 21, pp. 5105–5108, 2015.

[153] H. Huang, X. Xiao, J. Nees, and I. Jovanovic, "Broadband long-wave infrared pulse generation using chirped-pulse difference-frequency mixing," in *CLEO: Science and Innovations*, Optica Publishing Group, 2022, STh4E–4.

[154] H. Huang, X. Xiao, J. Nees, and I. Jovanovic, "Genetic algorithm optimization for ultra-broadband long-wave infrared seed pulse generation," in *2021 Conference on Lasers and Electro-Optics (CLEO)*, IEEE, 2021, pp. 1–2.

[155] G. Andriukaitis, T. Balčiūnas, S. Ališauskas, A. Pugžlys, A. Baltuška, T. Popmintchev, M.-C. Chen, M. M. Murnane, and H. C. Kapteyn, "90 GW peak power few-cycle mid-infrared pulses from an optical parametric amplifier," *Optics Letters*, vol. 36, no. 15, pp. 2755–2757, 2011.

[156] P. Wang, Y. Li, W. Li, H. Su, B. Shao, S. Li, C. Wang, D. Wang, R. Zhao, Y. Peng, Y. Leng, R. Li, and Z. Xu, "2.6 mJ/100 Hz CEP-stable near-single-cycle 4 µm laser based on OPCPA and hollow-core fiber compression," *Optics Letters*, vol. 43, no. 9, pp. 2197–2200, 2018.

[157] L. von Grafenstein, M. Bock, D. Ueberschaer, K. Zawilski, P. Schunemann, U. Griebner, and T. Elsaesser, "5 µm few-cycle pulses with multi-gigawatt peak power at a 1 kHz repetition rate," *Optics Letters*, vol. 42, no. 19, pp. 3796–3799, 2017.

[158] S. Wandel, M.-W. Lin, Y. Yin, G. Xu, and I. Jovanovic, "Bandwidth control in 5 µm pulse generation by dual-chirped optical parametric amplification," *J. Opt. Soc. Am. B*, vol. 33, no. 8, pp. 1580–1587, 2016.

[159] T. Kanai, P. Malevich, S. S. Kangaparambil, K. Ishida, M. Mizui, K. Yamanouchi, H. Hoogland, R. Holzwarth, A. Pugzlys, and A. Baltuska, "Parametric amplifica-

tion of 100 fs mid-infrared pulses in $ZnGeP_2$ driven by a Ho: YAG chirped-pulse amplifier," *Optics Letters*, vol. 42, no. 4, pp. 683–686, 2017.

[160] D. Sanchez, M. Hemmer, M. Baudisch, S. Cousin, K. Zawilski, P. Schunemann, O. Chalus, C. Simon-Boisson, and J. Biegert, "7 µm, ultrafast, sub-millijoule-level mid-infrared optical parametric chirped pulse amplifier pumped at 2 µm," *Optica*, vol. 3, no. 2, pp. 147–150, 2016.

[161] U. Elu, T. Steinle, D. Sánchez, L. Maidment, K. Zawilski, P. Schunemann, U. Zeitner, C. Simon-Boisson, and J. Biegert, "Table-top high-energy 7 µm OPCPA and 260 mJ Ho: YLF pump laser," *Optics Letters*, vol. 44, no. 13, pp. 3194–3197, 2019.

[162] S. Qu, H. Liang, K. Liu, X. Zou, W. Li, Q. J. Wang, and Y. Zhang, "9 µm few-cycle optical parametric chirped-pulse amplifier based on $LiGaS_2$," *Optics Letters*, vol. 44, no. 10, pp. 2422–2425, 2019.

[163] M. De Barros and P. Becker, "Two-color synchronously mode-locked femtosecond Ti:sapphire laser," *Optics Letters*, vol. 18, no. 8, pp. 631–633, 1993.

[164] F. Seifert, V. Petrov, and M. Woerner, "Solid-state laser system for the generation of midinfrared femtosecond pulses tunable from 3.3 to 10 µm," *Optics Letters*, vol. 19, no. 23, pp. 2009–2011, 1994.

[165] K. Akagawa, S. Wada, A. Nakamura, and H. Tashiro, "Synchronization of pulsed Ti:sapphire lasers and its application to difference frequency mixing for tunable infrared generation," *Applied Optics*, vol. 35, no. 15, pp. 2570–2575, 1996.

[166] J. M. Fraser, D. Wang, A. Hache, G. R. Allan, and H. M. Van Driel, "Generation of high-repetition-rate femtosecond pulses from 8 to 18 µm," *Applied Optics*, vol. 36, no. 21, pp. 5044–5047, 1997.

[167] N. Saito, K. Akagawa, S. Wada, and H. Tashiro, "Difference-frequency generation by mixing dual-wavelength pulses emitting from an electronically tuned Ti:sapphire laser," *Applied Physics B*, vol. 69, no. 2, pp. 93–97, 1999.

[168] R. A. Kaindl, M. Wurm, K. Reimann, P. Hamm, A. M. Weiner, and M. Woerner, "Generation, shaping, and characterization of intense femtosecond pulses tunable from 3 to 20 µm," *J. Opt. Soc. Am. B*, vol. 17, no. 12, pp. 2086–2094, 2000.

[169] F. Rotermund, V. Petrov, and F. Noack, "Difference-frequency generation of intense femtosecond pulses in the mid-IR (4–12 µm) using $HgGa_2S_4$ and $AgGaS_2$," *Optics Communications*, vol. 185, no. 1-3, pp. 177–183, 2000.

[170] J. Xia, J. Song, and D. Strickland, "Development of a dual-wavelength Ti:sapphire multi-pass amplifier and its application to intense mid-infrared generation," *Optics Communications*, vol. 206, no. 1-3, pp. 149–157, 2002.

[171] K. Yamakawa and C. Barty, "Two-color chirped-pulse amplification in an ultrabroadband Ti:sapphire ring regenerative amplifier," *Optics Letters*, vol. 28, no. 23, pp. 2402–2404, 2003.

[172] A. Sugita, K. Yokoyama, H. Yamada, N. Inoue, M. Aoyama, and K. Yamakawa, "Generation of broadband mid-infrared pulses by noncollinear difference frequency mixing," *Japanese Journal of Applied Physics*, vol. 46, no. 1R, p. 226, 2007.

[173] J. Fraser, I. Cheung, F. Legare, D. Villeneuve, J. Likforman, M. Joffre, and P. Corkum, "High-energy sub-picosecond pulse generation from 3 to 20 µm," *Applied Physics B*, vol. 74, no. 1, s153–s156, 2002.

[174] C. Manzoni, G. Cirmi, D. Brida, S. De Silvestri, and G. Cerullo, "Optical-parametric-generation process driven by femtosecond pulses: Timing and carrier-envelope phase properties," *Physical Review A*, vol. 79, no. 3, p. 033 818, 2009.

[175] K. Okamura and T. Kobayashi, "Octave-spanning carrier-envelope phase stabilized visible pulse with sub-3-fs pulse duration," *Optics Letters*, vol. 36, no. 2, pp. 226–228, 2011.

[176] C. Erny and C. P. Hauri, "Design of efficient single-stage chirped pulse difference frequency generation at 7 µm, driven by a dual wavelength Ti:sapphire laser," *Applied Physics B*, vol. 117, no. 1, pp. 379–387, 2014.

[177] Y. Yin, A. Chew, X. Ren, J. Li, Y. Wang, Y. Wu, and Z. Chang, "Towards terawatt sub-cycle long-wave infrared pulses via chirped optical parametric amplification and indirect pulse shaping," *Scientific Reports*, vol. 7, p. 45 794, 2017.

[178] Y. Fu, K. Midorikawa, and E. J. Takahashi, "Towards a petawatt-class few-cycle infrared laser system via dual-chirped optical parametric amplification," *Scientific Reports*, vol. 8, no. 1, pp. 1–11, 2018.

[179] C. Barty, T. Guo, C. Le Blanc, F. Raksi, C. Rose-Petruck, J. Squier, K. Wilson, V. Yakovlev, and K. Yamakawa, "Generation of 18-fs, multiterawatt pulses by regenerative pulse shaping and chirped-pulse amplification," *Optics Letters*, vol. 21, no. 9, pp. 668–670, 1996.

[180] F. G. Omenetto, B. P. Luce, and A. J. Taylor, "Genetic algorithm pulse shaping for optimum femtosecond propagation in optical fibers," *J. Opt. Soc. Am. B*, vol. 16, no. 11, pp. 2005–2009, 1999.

[181] U. Andral, R. S. Fodil, F. Amrani, F. Billard, E. Hertz, and P. Grelu, "Fiber laser mode locked through an evolutionary algorithm," *Optica*, vol. 2, no. 4, pp. 275–278, 2015.

[182] I. Jovanovic, D. French, J. Walter, and R. Ratowsky, "Numerical studies of multimodal phase-sensitive parametric amplification," *J. Opt. Soc. Am. B*, vol. 26, no. 6, pp. 1169–1175, 2009.

[183] Eksma Optics, *Infrared nonlinear crystals*, https://eksmaoptics.com/out/media/EKSMA_Optics_Infrared_Nonlinear_Crystals.pdf.

[184] T. Fuji, A. Apolonski, and F. Krausz, "Self-stabilization of carrier-envelope offset phase by use of difference-frequency generation," *Optics Letters*, vol. 29, no. 6, pp. 632–634, 2004.

[185] W. P. Leemans, B. Nagler, A. J. Gonsalves, C. Tóth, K. Nakamura, C. G. Geddes, E. Esarey, C. Schroeder, and S. Hooker, "GeV electron beams from a centimetre-scale accelerator," *Nature Physics*, vol. 2, no. 10, pp. 696–699, 2006.

[186] C. G. Geddes, C. Toth, J. van Tilborg, E. Esarey, C. Schroeder, D. Bruhwiler, C. Nieter, J. Cary, and W. Leemans, "High quality electron beams from a plasma channel guided laser wakefield accelerator," *Nature*, vol. 431, no. 7008, 2004.

[187] S. P. Mangles, C. Murphy, Z. Najmudin, A. G. R. Thomas, J. Collier, A. E. Dangor, E. Divall, P. Foster, J. Gallacher, C. Hooker, *et al.*, "Monoenergetic beams of relativistic electrons from intense laser-plasma interactions," *Nature*, vol. 431, no. 7008, pp. 535–538, 2004.

[188] J. Faure, Y. Glinec, A. Pukhov, S. Kiselev, S. Gordienko, E. Lefebvre, J.-P. Rousseau, F. Burgy, and V. Malka, "A laser-plasma accelerator producing monoenergetic electron beams," *Nature*, vol. 431, no. 7008, pp. 541–544, 2004.

[189] A. Zylstra, O. Hurricane, D. Callahan, A. Kritcher, J. Ralph, H. Robey, J. Ross, C. Young, K. Baker, D. Casey, *et al.*, "Burning plasma achieved in inertial fusion," *Nature*, vol. 601, no. 7894, pp. 542–548, 2022.

[190] X.-L. Zhu, M. Chen, S.-M. Weng, T.-P. Yu, W.-M. Wang, F. He, Z.-M. Sheng, P. McKenna, D. A. Jaroszynski, and J. Zhang, "Extremely brilliant GeV γ-rays from a two-stage laser-plasma accelerator," *Science Advances*, vol. 6, no. 22, eaaz7240, 2020.

[191] S.-W. Bahk, P. Rousseau, T. Planchon, V. Chvykov, G. Kalintchenko, A. Maksimchuk, G. Mourou, and V. Yanovsky, "Generation and characterization of the highest laser intensities (10^{22} W/cm^2)," *Optics Letters*, vol. 29, no. 24, pp. 2837–2839, 2004.

[192] J. W. Yoon, C. Jeon, J. Shin, S. K. Lee, H. W. Lee, I. W. Choi, H. T. Kim, J. H. Sung, and C. H. Nam, "Achieving the laser intensity of 5.5×10^{22} W/cm^2 with a wavefront-corrected multi-PW laser," *Optics Express*, vol. 27, no. 15, pp. 20 412–20 420, 2019.

[193] J. W. Yoon, Y. G. Kim, I. W. Choi, J. H. Sung, H. W. Lee, S. K. Lee, and C. H. Nam, "Realization of laser intensity over 10^{23} W/cm^2," *Optica*, vol. 8, no. 5, pp. 630–635, 2021.

[194] P. Zhang, S. Bulanov, D. Seipt, A. Arefiev, and A. Thomas, "Relativistic plasma physics in supercritical fields," *Physics of Plasmas*, vol. 27, no. 5, p. 050 601, 2020.

[195] F. Isono, J. van Tilborg, S. K. Barber, J. Natal, C. Berger, H.-E. Tsai, T. Ostermayr, A. Gonsalves, C. Geddes, and E. Esarey, "High-power non-perturbative laser delivery diagnostics at the final focus of 100-TW-class laser pulses," *High Power Laser Science and Engineering*, vol. 9, e25, 2021.

[196] G. Genoud, F. Wojda, M. Burza, A. Persson, and C.-G. Wahlström, "Active control of the pointing of a multi-terawatt laser," *Review of Scientific Instruments*, vol. 82, no. 3, p. 033 102, 2011.

[197] T. Kanai, A. Suda, S. Bohman, M. Kaku, S. Yamaguchi, and K. Midorikawa, "Pointing stabilization of a high-repetition-rate high-power femtosecond laser for intense few-cycle pulse generation," *Applied Physics Letters*, vol. 92, no. 6, p. 061 106, 2008.

[198] S. Tang, Y. Guo, P. Yang, X. Jiang, N. Hua, and N. Zong, "Stability improvement of multi-beam picosecond-petawatt laser system for ultrahigh peak-power applications," *Frontiers in Physics*, vol. 11, p. 1 118 254, 2023.

[199] Y. Lu, D. Fan, and Z. Zhang, "Theoretical and experimental determination of bandwidth for a two-axis fast steering mirror," *Optik*, vol. 124, no. 16, pp. 2443–2449, 2013.

[200] K. Tyszka, M. Dobosz, and T. Bilaszewski, "Double wedge prism based beam deflector for precise laser beam steering," *Review of Scientific Instruments*, vol. 89, no. 2, p. 025 113, 2018.

[201] M. J. Kay, A. A. Rakhman, and S. M. Cousineau, "Active pointing control of pulsed, high-power laser beam after 65-meter transport," in *2022 IEEE 17th International Conference on Control & Automation (ICCA)*, IEEE, 2022, pp. 565–570.

[202] A. Barna, I. Földes, J. Bohus, and S. Szatmári, "Active stabilization of the beam pointing of a high-power KrF laser system," *Metrology and Measurement Systems*, vol. 22, no. 1, pp. 165–172, 2015.

[203] R. A. Hardin, Y. Liu, C. Long, A. Aleksandrov, and W. Blokland, "Active beam position stabilization of pulsed lasers for long-distance ion profile diagnostics at the Spallation Neutron Source (SNS)," *Optics Express*, vol. 19, no. 4, pp. 2874–2885, 2011.

[204] M. Mori, A. Pirozhkov, M. Nishiuchi, K. Ogura, A. Sagisaka, Y. Hayashi, S. Orimo, A. Fukumi, Z. Li, M. Kado, *et al.*, "Development of beam-pointing stabilizer on a 10-TW Ti:Al_2O_3 laser system JLITE-X for laser-excited ion accelerator research," *Laser Physics*, vol. 16, pp. 1092–1096, 2006.

[205] L. Kral, "Automatic beam alignment system for a pulsed infrared laser," *Review of Scientific Instruments*, vol. 80, no. 1, p. 013 102, 2009.

[206] F. Breitling, R. Weigel, M. Downer, and T. Tajima, "Laser pointing stabilization and control in the submicroradian regime with neural networks," *Review of Scientific Instruments*, vol. 72, no. 2, pp. 1339–1342, 2001.

[207] H. Chang, W.-Q. Ge, H.-C. Wang, H. Yuan, and Z.-W. Fan, "Laser beam pointing stabilization control through disturbance classification," *Sensors*, vol. 21, no. 6, p. 1946, 2021.

[208] F. Qin, D. Zhang, D. Xing, D. Xu, and J. Li, "Laser beam pointing control with piezoelectric actuator model learning," *IEEE Transactions on Systems, Man, and Cybernetics: Systems*, vol. 50, no. 3, pp. 1024–1034, 2017.

[209] S. Borneis, T. Laštovička, M. Sokol, T.-M. Jeong, F. Condamine, O. Renner, V. Tikhonchuk, H. Bohlin, A. Fajstavr, J.-C. Hernandez, *et al.*, "Design, installation and commissioning of the ELI-Beamlines high-power, high-repetition rate HAPLS laser beam transport system to P3," *High Power Laser Science and Engineering*, vol. 9, e30, 2021.

[210] D. J. Trummer, R. J. Foley, and G. S. Shaw, "Stability of optical elements in the NIF target area building," in *Third International Conference on Solid State Lasers for Application to Inertial Confinement Fusion*, SPIE, vol. 3492, 1999, pp. 363–371.

[211] R. Budriūnas, K. Jurkus, M. Vengris, and A. Varanavičius, "Long seed, short pump: converting Yb-doped laser radiation to multi-µJ few-cycle pulses tunable through 2.5–15 µm," *Optics Express*, vol. 30, no. 8, pp. 13 009–13 023, 2022.

[212] M. Duda, L. von Grafenstein, M. Bock, D. Ueberschaer, P. Fuertjes, L. Roškot, M. Smrž, O. Novák, and U. Griebner, "10-µJ few-cycle 12-µm source based on difference-frequency generation driven by a 1-kHz mid-wave infrared OPCPA," *Optics Letters*, vol. 47, no. 11, pp. 2891–2894, 2022.

[213] X. Xiao, J. Nees, H. Huang, and I. Jovanovic, "Nanosecond 2.73-µm parametric source for pumping LWIR OPCPA," in *CLEO: QELS_Fundamental Science*, Optical Society of America, 2021, JTu3A–109.

[214] I. Jovanovic, X. Xiao, and H. Huang, "Production of high-power ultrashort pulses in the long-wave infrared range," in *2020 IEEE Photonics Conference (IPC)*, IEEE, 2020, pp. 1–2.

[215] X. Xiao, J. Nees, H. Huang, A. Galvanauskas, and I. Jovanovic, "Optical parametric amplification at 10.6 µm in GaSe pumped by a 2.75-µm parametric source," in *CLEO: Applications and Technology*, Optical Society of America, 2020, JTu2F–19.

[216] H. Huang, C. Zhang, R. Crisci, T. Lu, H.-C. Hung, M. S. J. Sajib, P. Sarker, J. Ma, T. Wei, S. Jiang, *et al.*, "Strong surface hydration and salt resistant mechanism of a new nonfouling zwitterionic polymer based on protein stabilizer TMAO,"

Journal of the American Chemical Society, vol. 143, no. 40, pp. 16 786–16 795, 2021.

[217] H. Wang, J. Jasensky, N. W. Ulrich, J. Cheng, H. Huang, Z. Chen, and C. He, "Capsaicin-inspired thiol–ene terpolymer networks designed for antibiofouling coatings," *Langmuir*, vol. 33, no. 47, pp. 13 689–13 698, 2017.

[218] C. Leng, H. Huang, K. Zhang, H.-C. Hung, Y. Xu, Y. Li, S. Jiang, and Z. Chen, "Effect of surface hydration on antifouling properties of mixed charged polymers," *Langmuir*, vol. 34, no. 22, pp. 6538–6545, 2018.

[219] K. Zhang, H. Huang, H.-C. Hung, C. Leng, S. Wei, R. Crisci, S. Jiang, and Z. Chen, "Strong hydration at the poly (ethylene glycol) brush/albumin solution interface," *Langmuir*, vol. 36, no. 8, pp. 2030–2036, 2020.

[220] S. Wei, X. Zou, J. Tian, H. Huang, W. Guo, and Z. Chen, "Control of protein conformation and orientation on graphene," *Journal of the American Chemical Society*, vol. 141, no. 51, pp. 20 335–20 343, 2019.

[221] B. H. Stuart, *Infrared spectroscopy: fundamentals and applications*. John Wiley & Sons, 2004.

[222] X. Xiao, "Broadband long-wave infrared few-cycle pulse generation via optical parametric chirped-pulse amplification," Ph.D. dissertation, 2021.

[223] S. Qu, G. C. Nagar, W. Li, K. Liu, X. Zou, S. H. Luen, D. Dempsey, K.-H. Hong, Q. J. Wang, Y. Zhang, *et al.*, "Long-wavelength-infrared laser filamentation in solids in the near-single-cycle regime," *Optics Letters*, vol. 45, no. 8, pp. 2175–2178, 2020.

[224] A. Lanin, A. Fedotov, and A. Zheltikov, "Ultrabroadband XFROG of few-cycle mid-infrared pulses by four-wave mixing in a gas," *J. Opt. Soc. Am. B*, vol. 31, no. 8, pp. 1901–1905, 2014.

[225] D. J. Wilson, A. M. Summers, S. Zigo, B. Davis, S.-J. Robatjazi, J. A. Powell, D. Rolles, A. Rudenko, and C. A. Trallero-Herrero, "An intense, few-cycle source in the long-wave infrared," *Scientific Reports*, vol. 9, no. 1, p. 6002, 2019.

[226] P. D. Olszak, C. M. Cirloganu, S. Webster, L. A. Padilha, S. Guha, L. P. Gonzalez, S. Krishnamurthy, D. J. Hagan, and E. W. Van Stryland, "Spectral and temperature dependence of two-photon and free-carrier absorption in InSb," *Physical Review B*, vol. 82, no. 23, p. 235 207, 2010.

[227] R. Trebino, *Frequency-Resolved Optical Gating: The Measurement of Ultrashort Laser Pulses*. Springer Science & Business Media, 2000.

[228] K. W. DeLong, D. N. Fittinghoff, R. Trebino, B. Kohler, and K. Wilson, "Pulse retrieval in frequency-resolved optical gating based on the method of generalized projections," *Optics Letters*, vol. 19, no. 24, pp. 2152–2154, 1994.

[229] R. Jafari and R. Trebino, "High-speed "multi-grid" pulse-retrieval algorithm for frequency-resolved optical gating," *Optics Express*, vol. 26, no. 3, pp. 2643–2649, 2018.

[230] T. Zahavy, A. Dikopoltsev, D. Moss, G. I. Haham, O. Cohen, S. Mannor, and M. Segev, "Deep learning reconstruction of ultrashort pulses," *Optica*, vol. 5, no. 5, pp. 666–673, 2018.

[231] P. E. Ciddor, "Refractive index of air: New equations for the visible and near infrared," *Applied Optics*, vol. 35, no. 9, pp. 1566–1573, 1996.

[232] R. J. Mathar, "Refractive index of humid air in the infrared: Model fits," *Journal of Optics A: Pure and Applied Optics*, vol. 9, no. 5, p. 470, 2007.

[233] X. Xiao, J. Nees, and I. Jovanovic, "High-energy nanosecond parametric source at 2.7 µm," *Applied Optics*, vol. 60, no. 13, pp. 3585–3590, 2021.

[234] G. Abdullaev, L. Kulevskiĭ, P. Nikles, A. Prokhorov, A. Savel'ev, E. Y. Salaev, and V. Smirnov, "Difference frequency generation in a GaSe crystal with continuous tuning in the 560–1050 cm^{-1} range," *Soviet Journal of Quantum Electronics*, vol. 6, no. 1, p. 88, 1976.

[235] K. Vodopyanov, S. Mirov, V. Voevodin, and P. Schunemann, "Two-photon absorption in GaSe and $CdGeAs_2$," *Optics Communications*, vol. 155, no. 1-3, pp. 47–50, 1998.

[236] V. Petrov, V. L. Panyutin, A. Tyazhev, G. Marchev, A. I. Zagumennyi, F. Rotermund, F. Noack, K. Miyata, L. Iskhakova, and A. Zerrouk, "$GaS_{0.4}Se_{0.6}$: Relevant properties and potential for 1064 nm pumped mid-IR OPOs and OPGs operating above 5 µm," *Laser Physics*, vol. 21, pp. 774–781, 2011.

[237] J. Guo, J.-J. Xie, D.-J. Li, G.-L. Yang, F. Chen, C.-R. Wang, L.-M. Zhang, Y. M. Andreev, K. A. Kokh, G. V. Lanskii, *et al.*, "Doped GaSe crystals for laser frequency conversion," *Light: Science & Applications*, vol. 4, no. 12, e362–e362, 2015.